SF 298 MASTER COPY KEEP THIS COPY FOR REPRODUCTION PURPOSES

REPORT DOCUMENTATION PAGE

Form Approved
OMB NO. 0704-0188

1. AGENCY USE ONLY *(Leave blank)*

2. REPORT DATE
4/15/97

3. REPORT TYPE AND DATES COVERED
Final

4. TITLE AND SUBTITLE
Simulation of Massively Separated Flow Around a Missile Angle of Attack Using Solution-Adaptive Re-Meshing

5. FUNDING NUMBERS
DAAH04-95-1-0040

6. AUTHOR(S)
Bharat K. Soni

7. PERFORMING ORGANIZATION NAMES(S) AND ADDRESS(ES)
Bharat K. Soni
Engineering Research Center for Computational Field Simulation
P.O. Box 9627
Mississippi State, MS 39762

8. PERFORMING ORGANIZATION REPORT NUMBER

9. SPONSORING / MONITORING AGENCY NAME(S) AND ADDRESS(ES)
U.S. Army Research Office
P.O. Box 12211
Research Triangle Park, NC 27709-2211

10. SPONSORING / MONITORING AGENCY REPORT NUMBER
ARO 33958. 1-EG

11. SUPPLEMENTARY NOTES
The views, opinions and/or findings contained in this report are those of the author(s) and should not be construed as an official Department of the Army position, policy or decision, unless so designated by other documentation.

12a. DISTRIBUTION / AVAILABILITY STATEMENT
Approved for public release; distribution unlimited.

12 b. DISTRIBUTION CODE

19970515 185

TED 4

13. ABSTRACT *(Maximum 200 words)*

Simulation of massively separated flow around a missile at various angle of attack using solution adaptive re-meshing is performed. These simulations are exercised in support of the KTA2-12 program which is designed to evaluate computational technology for predicting highly separated flowfields for missile configurations. A new weight function using Boolean sum of pertinent solution gradient and curvature terms with appropriate scaling and normalization is developed. The new weight function is applicable to wide range of grid adaptive problems with no user input. The adaptive algorithms have been cast into a parallel multiblock adaptive grid system using MPI. The improvement in the convergence level and better agreement of flow solutions with experimental force and moment coefficients with flow solutions have been demonstrated by using the adaptive process. The computer codes NPARC and CFL3D are utilized for respective flow field simulations.

14. SUBJECT TERMS
Computational Fluid Dynamics (CFD), Grid Generation, Adaptive Gridding

15. NUMBER IF PAGES

16. PRICE CODE

17. SECURITY CLASSIFICATION OR REPORT	18. SECURITY CLASSIFICATION OF THIS PAGE	19. SECURITY CLASSIFICATION OF ABSTRACT	20. LIMITATION OF ABSTRACT
UNCLASSIFIED	UNCLASSIFIED	UNCLASSIFIED	UL

NSN 7540-01-280-5500

Enclosure 1

Standard Form 298 (Rev. 2-89)
Prescribed by ANSI Std. 239-18

GENERAL INSTRUCTIONS FOR COMPLETING SF 298

The Report Documentation Page (RDP) is used in announcing and cataloging reports. It is important that this information be consistent with the rest of the report, particularly the cover and title page. instructions for filling in each block of the form follow. It is important to ***stay within the lines*** to meet ***optical scanning requirements.***

Block 1. Agency Use Only *(Leave blank)*

Block 2. Report Date. Full publication date including day, month, and year, if available (e.g. 1 Jan 88). Must cite at least year.

Block 3. Type of Report and Dates Covered. State whether report is interim, final, etc. If applicable, enter inclusive report dates (e.g. 10 Jun 87 - 30 Jun 88).

Block 4. Title and Subtitle. A title is taken from the part of the report that provides the most meaningful and complete information. When a report is prepared in more than one volume, repeat the primary title, add volume number, and include subtitle for the specific volume. On classified documents enter the title classification in parentheses.

Block 5. Funding Numbers. To include contract and grant numbers; may include program element number(s), project number(s), task number(s), and work unit number(s). Use the following labels:

C - Contract
G - Grant
PE - Program Element
PR - Project
TA - Task
WU - Work Unit Accession No.

Block 6. Author(s). Name(s) of person(s) responsible for writing the report, performing the research, or credited with the content of the report. If editor or compiler, this should follow the name(s).

Block 7. Performing Organization Name(s) and Address(es). Self-explanatory.

Block 8. Performing Organization Report Number. Enter the unique alphanumeric report number(s) assigned by the organization performing the report.

Block 9. Sponsoring/Monitoring Agency Name(s) and Address(es). Self-explanatory.

Block 10. Sponsoring/Monitoring Agency Report Number. *(If known)*

Block 11. Supplementary Notes. Enter information not included elsewhere such as; prepared in cooperation with...; Trans. of...; To be published in.... When a report is revised, include a statement whether the new report supersedes or supplements the older report.

Block 12a. Distribution/Availability Statement. Denotes public availability or limitations. Cite any availability to the public. Enter additional limitations or special markings in all capitals (e.g. NORFORN, REL, ITAR).

DOD - See DoDD 4230.25, "Distribution Statements on Technical Documents."
DOE - See authorities.
NASA - See Handbook NHB 2200.2.
NTIS - Leave blank.

Block 12b. Distribution Code.

DOD - Leave blank
DOE - Enter DOE distribution categories from the Standard Distribution for Unclassified Scientific and Technical Reports
NASA - Leave blank.
NTIS - Leave blank.

Block 13. Abstract. Include a brief *(Maximum 200 words)* factual summary of the most significant information contained in the report.

Block 14. Subject Terms. Keywords or phrases identifying major subjects in the report.

Block 15. Number of Pages. Enter the total number of pages.

Block 16. Price Code. Enter appropriate price code *(NTIS only).*

Block 17. - 19. Security Classifications. Self-explanatory. Enter U.S. Security Classification in accordance with U.S. Security Regulations (i.e., UNCLASSIFIED). If form contains classified information, stamp classification on the top and bottom of the page.

Block 20. Limitation of Abstract. This block must be completed to assign a limitation to the abstract. Enter either UL (unlimited) or SAR (same as report). An entry in this block is necessary if the abstract is to be limited. If blank, the abstract is assumed to be unlimited.

FINAL REPORT

Simulation of Massively Separated Flow Around a Missile at Angle of Attack Using Solution–Adaptive Re–Meshing

by

Bharat K. Soni, Professor
Aerospace Engineering
NSF Engineering Research Center for
Computational Field Simulation
Mississippi State University
Mississippi State, MS 39762

601–325–2647
601–325–7692 Fax
Email: bsoni@erc.msstate.edu

Submitted to
U.S. Army Research Office
P.O. Box 1221
Research Triangle Park, NC 27709–2211

TABLE OF CONTENT

1. BACKGROUND

The proposed work addresses some research issues arising from Computational Fluid Dynamics (CFD) simulations performed in support of the KTA2–12 program. This program is designed to evaluate computational technology for predicting highly separated flowfields for missile configurations. Extensive experimental data at various axial locations is available for the test problem in the form of surface pressure coefficients, and flowfield pitot pressures for off surface structures. Two flow solvers, four turbulence models, and seven grids were used in various combinations to study the dependence of the predictions on a given component. One flow solver consistently yielded predictions closest to the data. For this flow solver the results were most sensitive to the grid used. It is desirable that the point distribution reflect some significant features of the flow, such as shocks and shear layers. It was very difficult and time consuming to construct an appropriate grid. In particular the feeding sheet was not properly resolved by any of the grids used. Also very small time steps, significant values of artificial viscosity, and large numbers of iterations were required. A solution–adaptive grid procedure is developed to address these issues.

The coordinates chosen for the mathematical formulation of fluid flow problems can have a significant effect on the accuracy and computational requirements of the analysis. In order to avoid problem–specific flow solvers, it is necessary that the coordinates be boundary conforming. Also, it is desirable that the coordinate point distribution reflect some significant features of the flow. Typically, grids are constructed based on the experience and intuition of the user. This process requires an experienced user and results in a time–consuming, iterative procedure. Several papers such as those by Thompson [1993], Anderson [1987], Soni and Yang [1992] and Soni, Weatherill and Thompson [1993] present applications where significant improvements in accuracy have been obtained through the use of solution adaptive grid procedures. Several approaches have employed for both structured and unstructured grid adaption. The most widely used approaches involve grid point redistribution, local grid point enrichment/derefinement or local modification of the actual flow solver. However, the success of any one of these methods ultimately depends on the feature detection algorithm used to flag regions of the solution domain which require a fine mesh for accurate representation. Typically, weight functions comprised of combinations of flow variable derivatives are constructed to mimic the local truncation error. The selection of which flow variables and in what combinations to include in such weight functions, may require substantial user input. These weight functions can then be used to construct blending functions for algebraic redistribution, interpolation functions for unstructured grid generation, forcing functions to attract/repel points in an elliptic system, or to trigger local refinement. Dwyer [1984] and Soni and Yang [1992] have developed scaling procedures to lessen the required user input for construction of these weight functions. It is believed that an adaptive grid system which requires no user input while ensuring an efficient grid point distribution would dramatically increase the routine use of CFD in the design and analysis environment. The development of such a system is the ultimate objective of this work.

Use of the adaptive process with the NPARC flow solver did improve the convergence level, agreement with flow visualization, and the agreement with the measured force and moment coefficients. The promising initial success indicates that the enhancements proposed significant further improvements can be obtained. Many problems of engineering interest involve multi–block grids. Hence, it is advantageous that the adaptive grid system be developed to recognize flow structures of different types as well as differing intensity, and adequately address scaling and normalization across blocks. The accurate prediction of unsteady flow phenomena is becoming increasingly important. It would be desirable to utilize the benefits of solution adaptive gridding for simulation of unsteady flow problems. These benefits are largest when the physical locations of the flowfield which require a fine grid for adequate resolution vary greatly with time.

2. DESCRIPTION OF PROBLEM

In order to study the accuracy and efficiency improvements due to the grid adaptation, it is necessary to quantify grid size and distribution requirements as well as computational times of non–adapted solutions. Hence, the first phase of this effort involves benchmarking the predictive capability through the use of solution adaptive gridding. This adaptive grid capability should automatically resolve complex flows with shock waves, expansion waves, shear layers and complex vortex–vortex and vortex–surface interactions. An adaptive grid approach seems well suited for such problems in which the spatial distribution of length scales is not known a priori.

There is interest in prediction capabilities for vortical flows about slender bodies of revolution. Maneuvering missiles often operate under flight conditions where forces induced by vortices often dominate. Also, delta wings proposed for High Speed Civil Transport (HSCT) aircraft often utilize vortex lift during landing and takeoff. Hence, the design of such vehicles would greatly benefit from a detailed and accurate knowledge of such flow fields. Due to the current interest in this type of flow, a generic missile body has been chosen as a test problem. As angle of attack and supersonic freestream conditions, this configuration exhibits large scale separated vortical flow, vortex–vortex and vortex–surface interactions, separated shear layers and multiple shocks of different intensity. Also, there is a substantial amount of experimental data available over a wide range of flow parameters. In fact, this problem is the focus of the KTA2–12 program. Pagan and Molton [1991], Hsieh, Wardlaw and Birch [1991], as well as the Army Research Laboratory (KTA2–12) have compiled experimental data. Data for the Mach number ranges from 0.7 to 3.5 and angles of attack from 0 to 20 degrees are available. Surface pressure coefficients as well as pitot pressure data for the off surface region are available. The availability of detailed experimental data for verification of the results coupled with the wide range of flow features provides a critical test for the capabilities of the flow solver used and any associated adaptive grid technique. Figure 1 illustrates the geometric configuration chosen for study along with an associated grid constructed using the GENIE++ [Soni, Thompson et. al., 1992] grid generation system.

3. RESEARCH OBJECTIVES & APPROACH

An overall objective of this work is to perform simulations in support of the KTA2–12 program and to address research issues associated with grid adaptation arising from these simulations.

The following tasks are performed to meet the aforestated objectives::

The first task involves simulations in order to better quantify the predictive capability of the NPARC [NASA LeRC 1993] and CFL3D [NASA LaRC 1993] flow solvers. The model configuration for the KTA2–12 project is a 3–caliber ogive with a 10–caliber cylindrical afterbody. The experimental data is available for six test cases involving different Mach numbers (in the range of 0.7 to 3.5) and angle of attack (8 and 14). The Navier–Stokes simulations are performed with different turbulence models. The six cases for which wind tunnel test conditions are available are presented in Table 1.

The second task is to develop an adaptive grid strategy and perform simulations using grid adaptation. The results of grid adaptation should be compared for improvements with the experimental data.

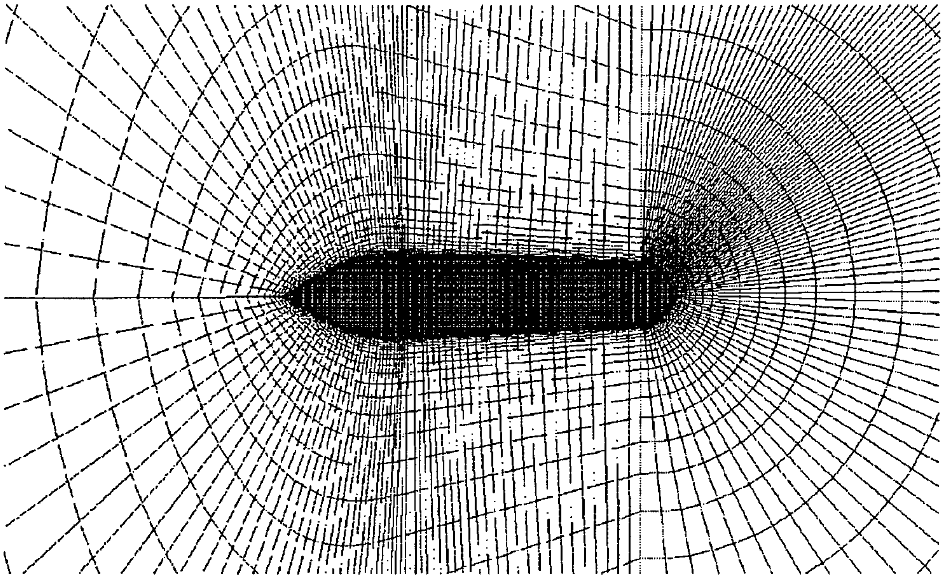

FIgure 1. Geometry and Initial Grid.

Case Number	Mach Number	Angle of Attack	Reynolds No, x 10^6 /Ft
1	1.45	14	2.0
2	1.8	14	2.0
3	2.5	14	4.0
4	3.5	8	4.0
5	3.5	14	2.0
6	0.7	14	2.0

Table 1. Wind Tunnel Test Conditions

4. SIMULATION RESULTS

The NPARC system simulates Reynolds averaged Navier–Stokes equations using finite difference Steger–Warming scheme utilizing multiblock structured grids. The scheme is second order accurate with ADI based time differencing allowing local time stepping. The program facilitates user oriented boundary condition specification. The CFL3D system also simulates Reynolds averaged Navier–Stokes equations using finite volume algorithm. The program allows a choice of Steger–Warming or Roe upwinding scheme. The third order accuracy can be achieved using MUSCL scheme. The limiters are based on the minmod technique. The program facilitates local time stepping, mesh sequencing and multigrid options to accelerate convergence. The Balwin–Lomax, Balwin–Barth and $k-\omega$ turbulence models are applicable for simulation.

The solutions were obtained using both NPARC [NASA LeRC 1994] and CFL3D [NASA LaRC 1993]. Four turbulence models were used to study the effect of the turbulence model on the solutions. The models used where the Baldwin–Lomax with the Dgani–Schiff correction, Baldwin–

Barth, k–ε, $k-\omega$ models for NPARC and Baldwin–Barth, Baldwin–Lomax, $k-\omega$ and Spalart–Allmaras models were used for CFL3D. Significant variations in the off surface structure were apparent with all flow solvers. The vortex grows in strength with the streamwise coordinate, and is located farther from the surface. The boundary layer separates to form the primary and secondary vortices. Hence, as the distance of the shear layer from the surface increases, the grid resolution decreases and accuracy deteriorates in the downstream direction. It was found that the solutions were very sensitive to the turbulence model. The general comments on both these codes is provided in Table 2.

The L_2 residual is considered for checking the order of the convergence. Most of the cases NPARC takes 6000–7000 iterations to achieve a residual of 10^{-6}–10^{-7}. For most of the turbulence model studies the NPARC code is restarted from the previously attained convergence solution for other models. This procedure reduces the overall run time for different turbulence model studies.

Typical convergence histories for different cases are shown in Figures 2–5.

The results obtained by applying various turbulence models for case 3 studies are presented. Four turbulence models were used for NPARC and CFL3D codes, as explained in the code performance section. k–ω implementation in CFL3D code may be corrupted due to errors (programming errors). The surface presents results associated with different turbulence models and comparison with experimental data for both the codes are displayed in Figures 6a–b and 7a–b.

For CFL3D, Spalart–Allmaras model gave good results. Comparison of resulting simulation using CFL3D and NPARC is also preformed. These results are presented in Figure 8a–b for Baldwin–Barth turbulence model, in Figure 8a–b for Baldwin–Lomax turbulence model and in Figure 10a–b for $k-\omega$ model.

The pitot–pressure with vortex structure comparison with experimental data is demonstrated in Figures 11–15 for different axial locations.

The forces and moments are calculated for case 3 and is given in Table 3. The computed axial forces are not matching well with that of experiment data. But simulated the normal force and moment matches well with the experimental data. The NPARC code with Baldwin–Barth turbulence model predicted the normal force and moments better than the other combinations.

NPARC	CFL3D
Central difference with artificial dissipation Sensitive to grid resolution esp near shock Vortex feeding sheet difficult to resolve properly Adaptive grid affects solution Very small CFL limit (0.5) Apparently due to shock resolution Slow convergence (5000 iter) esp in low speed viscous regions Cray C90, 1,556,280 grid points Case3 BL 47,332,701 words 5894 CPU seconds 1.2 x 10^{-5} sec/grid point 30 words/grid point 275 MFLOPS	Flux–Difference split, upwind Quick and easy Sharp resolution of shocks Sensitive to Flux limiter used Not as sensitive to grid as NPARC Cray C90, 1,556,280 grid points Case3 BL 91386581 words 5808 CPU seconds 9.33 x 10 sec/grid point 59 words/grid point 288 MFLOPS

Table 2. General Comments on Flow Solvers

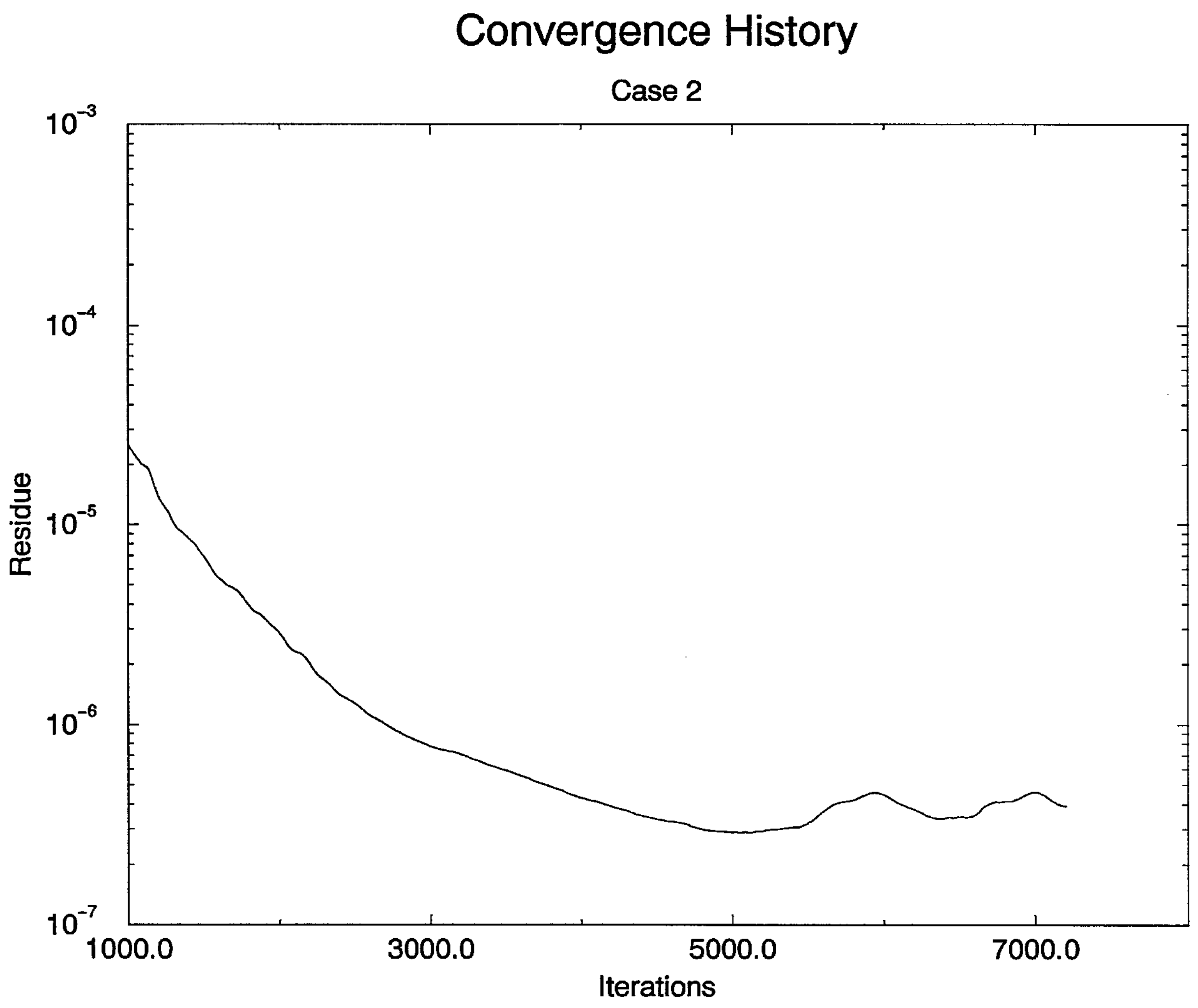

Figure 2 Convergence History gor Case 2 Using NPARC (Laminar)

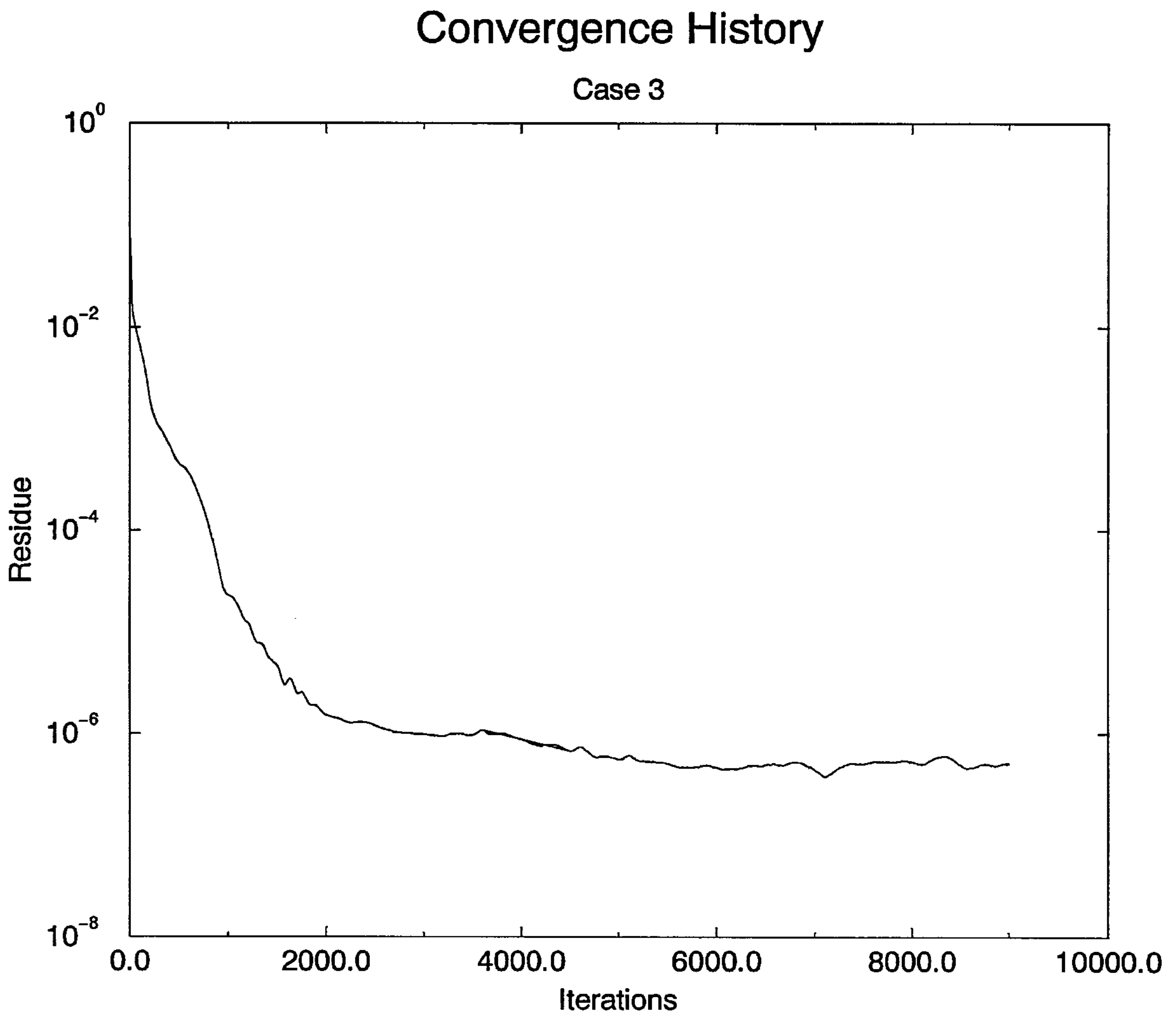

Figure 3 Convergence History for Case 3 Using NPARC (BL Model)

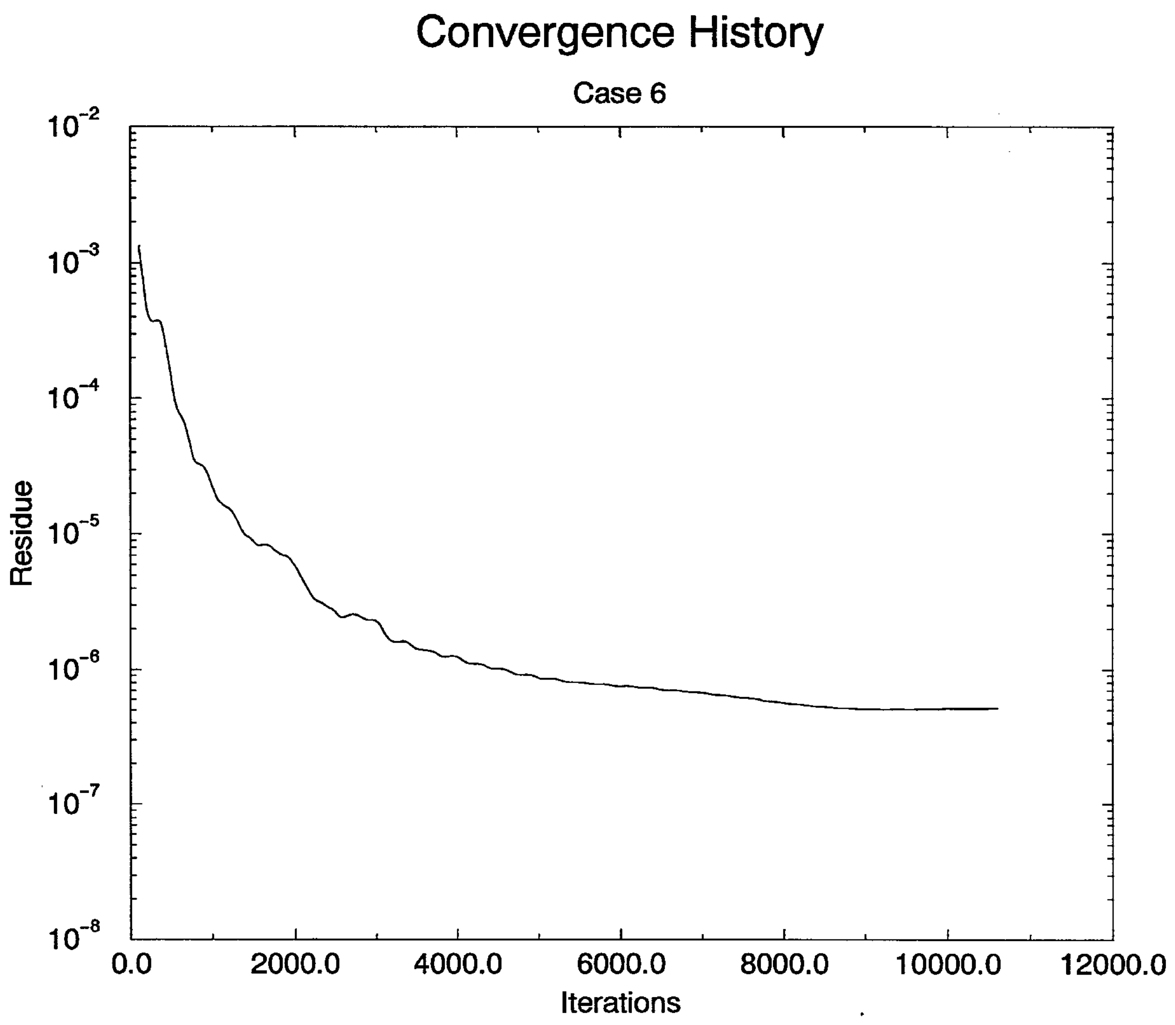

Figure 4 Convergence History for Case 6 Using NPARC (Euler)

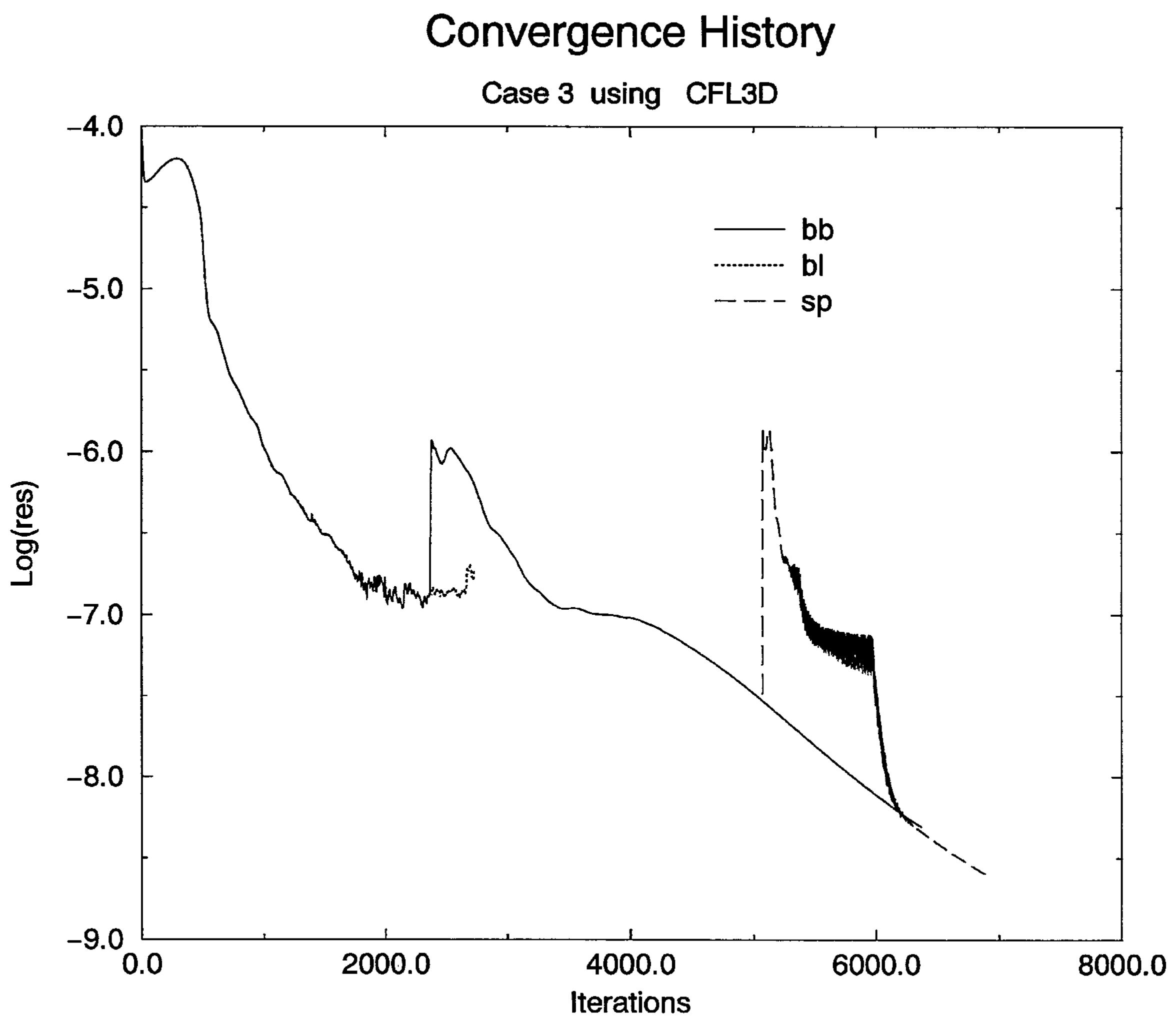

Figure 5 Convergnce History for Case 3 Using CFL3D

Force and Moment Comparisons					
Forces	Experimental Data	NPARC (BL)	NPARC (BB)	CFL3D BL	CFL3D BB
Axial	0.1957	0.3307	0.3297	0.3314	0.3311
Normal	1.9100	1.8855	1.9098	1.8729	1.9148
Moment	10.2417	10.0314	10.2666	9.9127	10.3315

Table 3. Forces/Moments (Case 3)

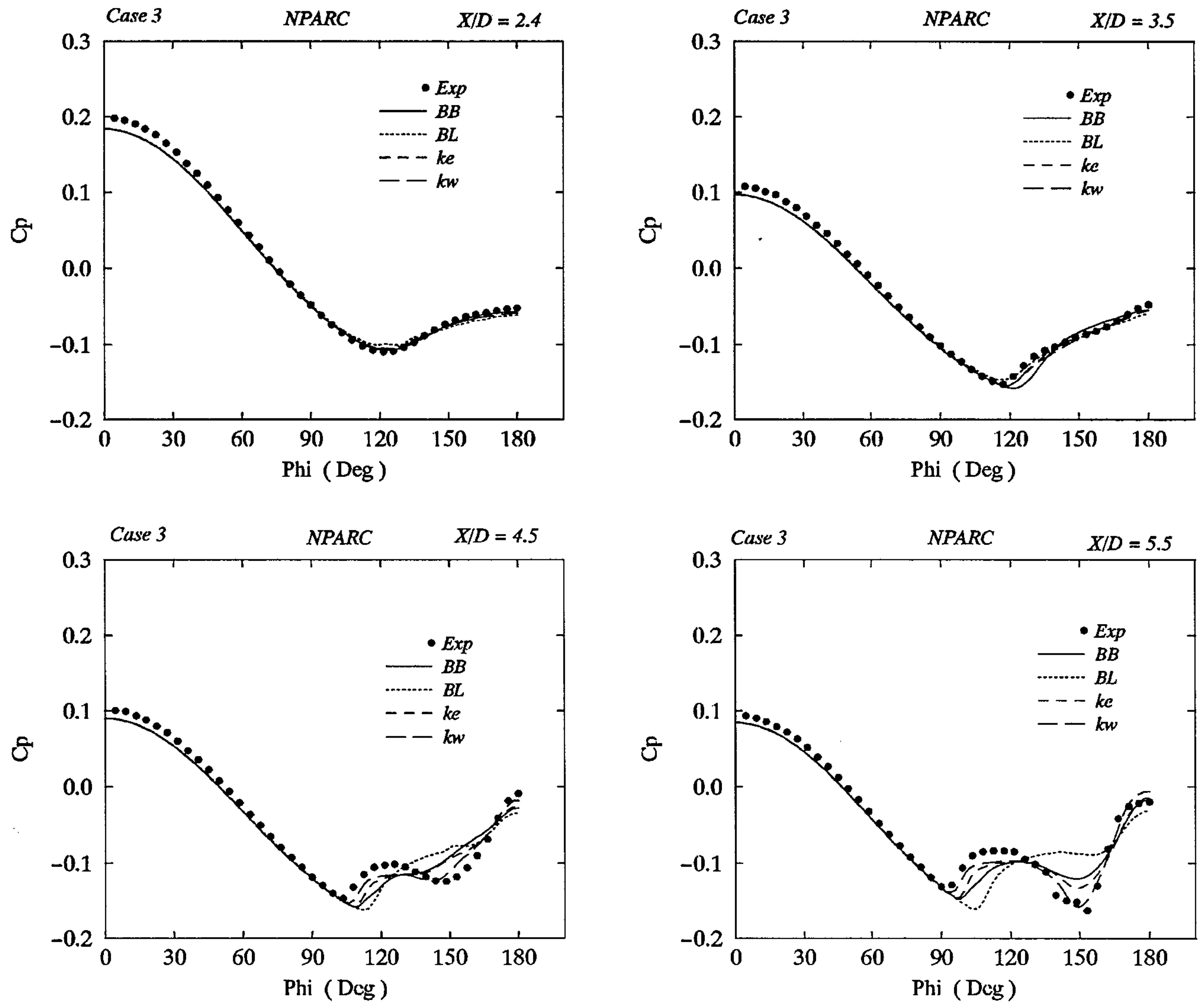

Figure 6(a) Turbulence Model Comparison for Case 3 Using NPARC

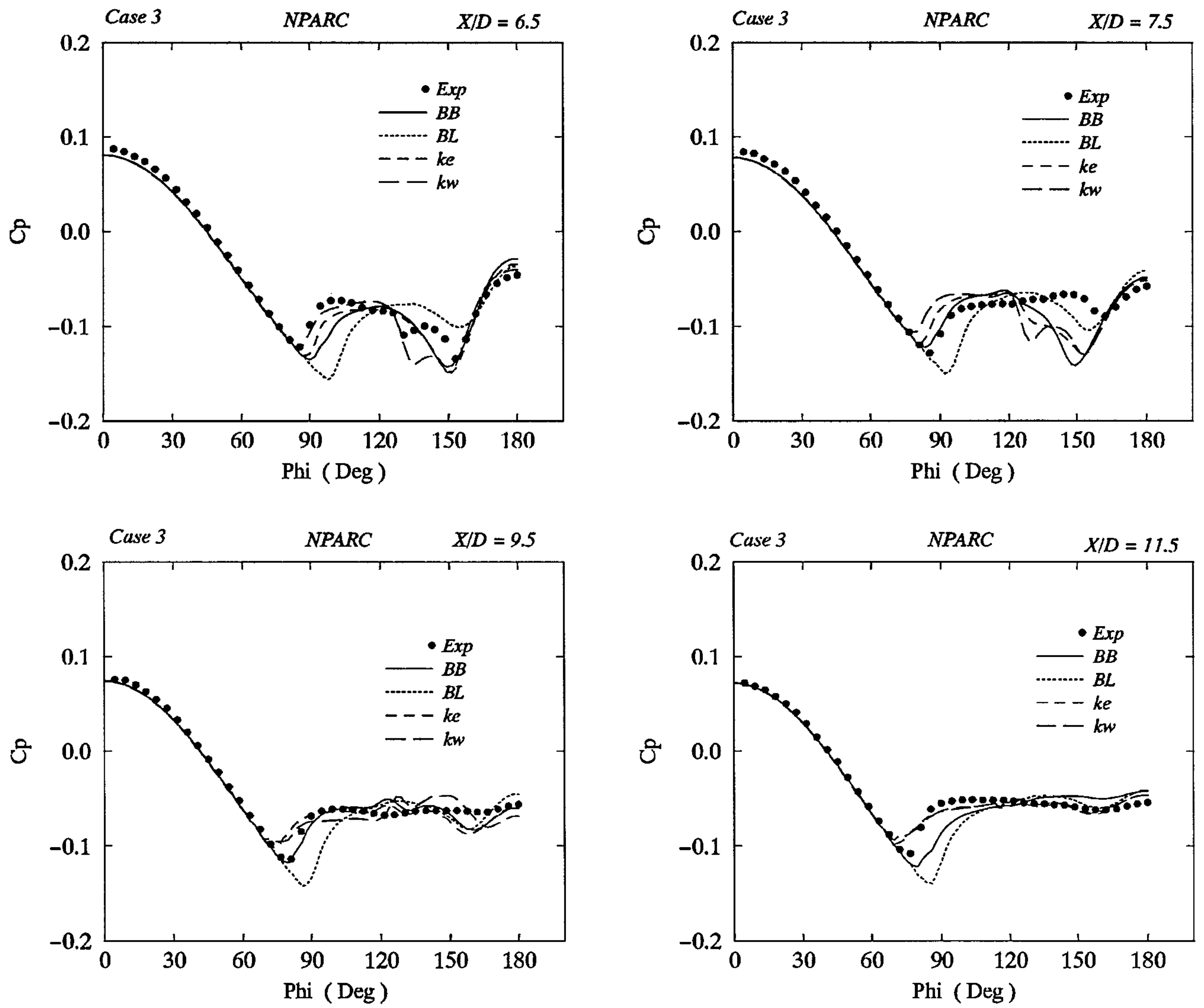

Figure 6(b) Turbulence Model Comparisons for Case 3 Using NPARC

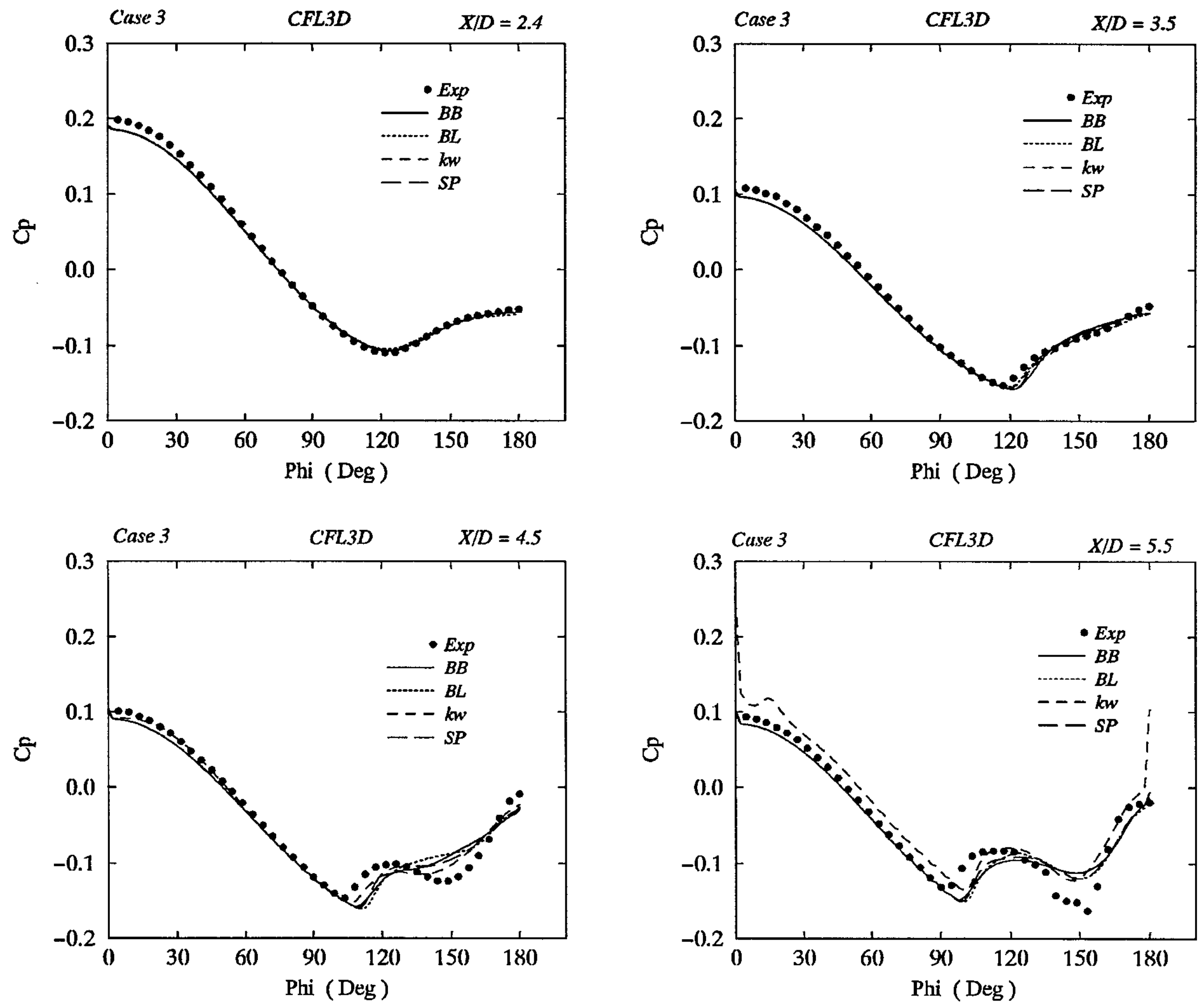

Figure 7(a) Turbulence Model Comparison for Case 3 Using CFL3d

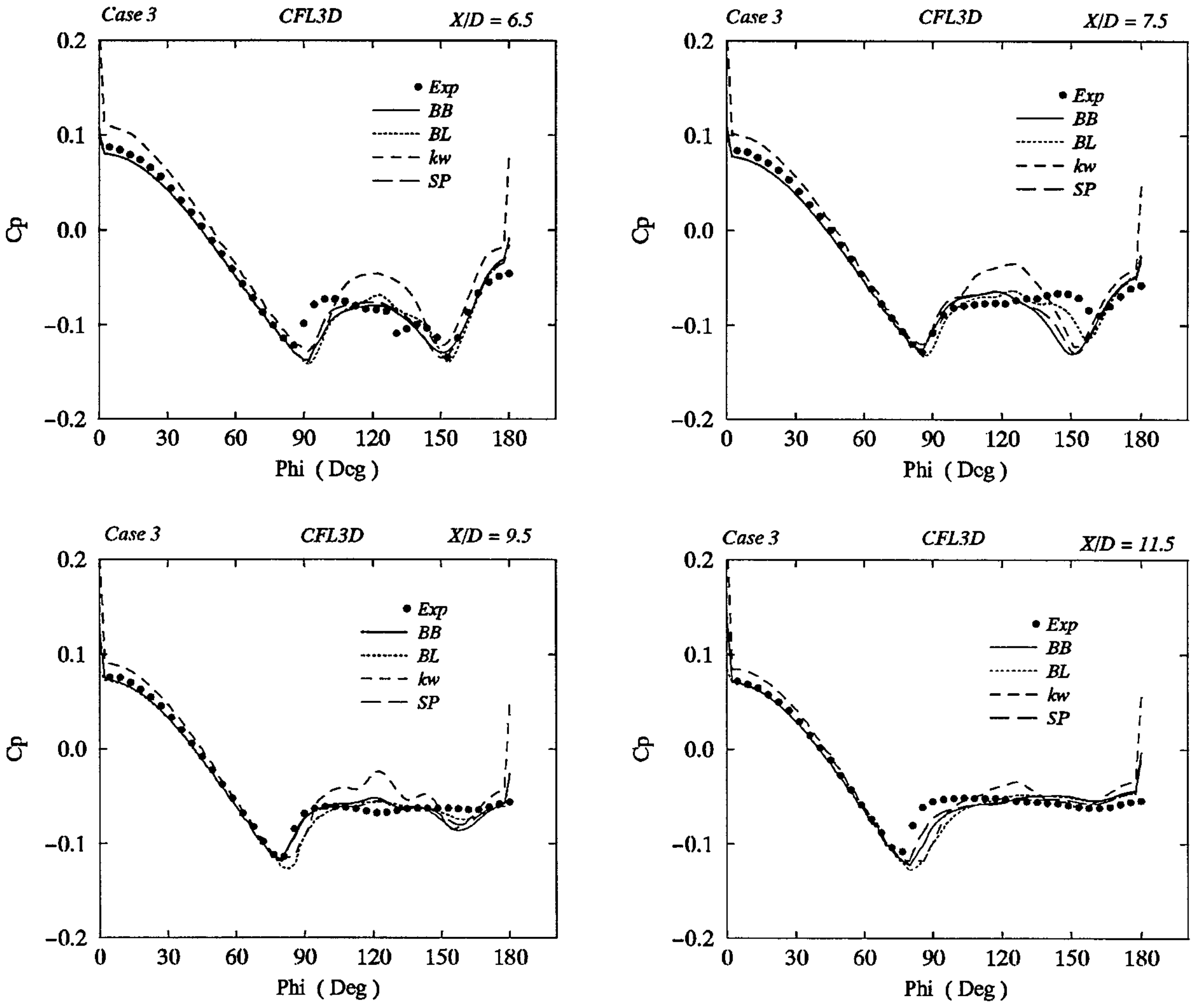

Figure 7(b) Turbulence Model Comparisons for Case 3 Using CFL3D

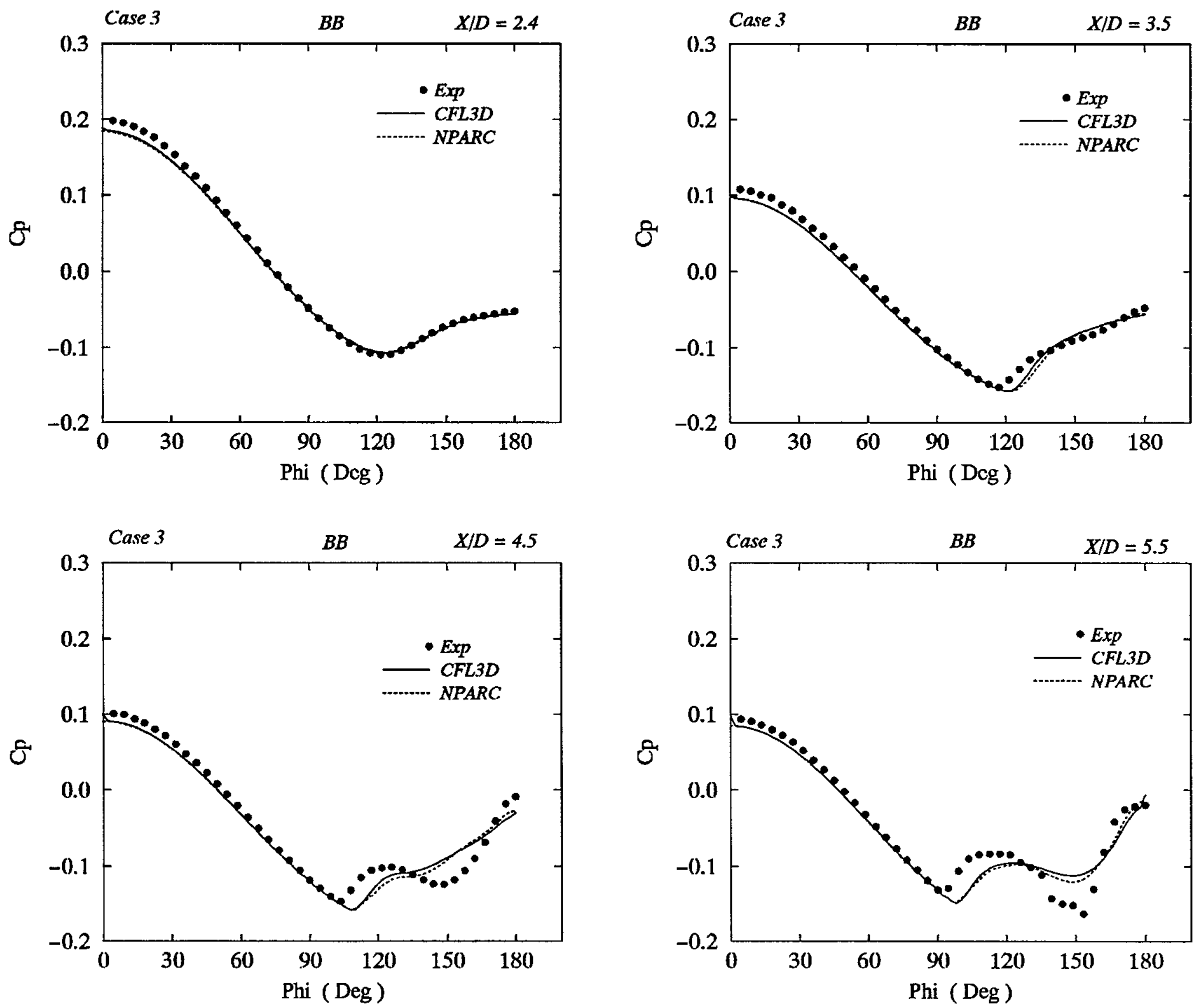

Figure 8(a) Baldwin–Barth TM for Both Codes

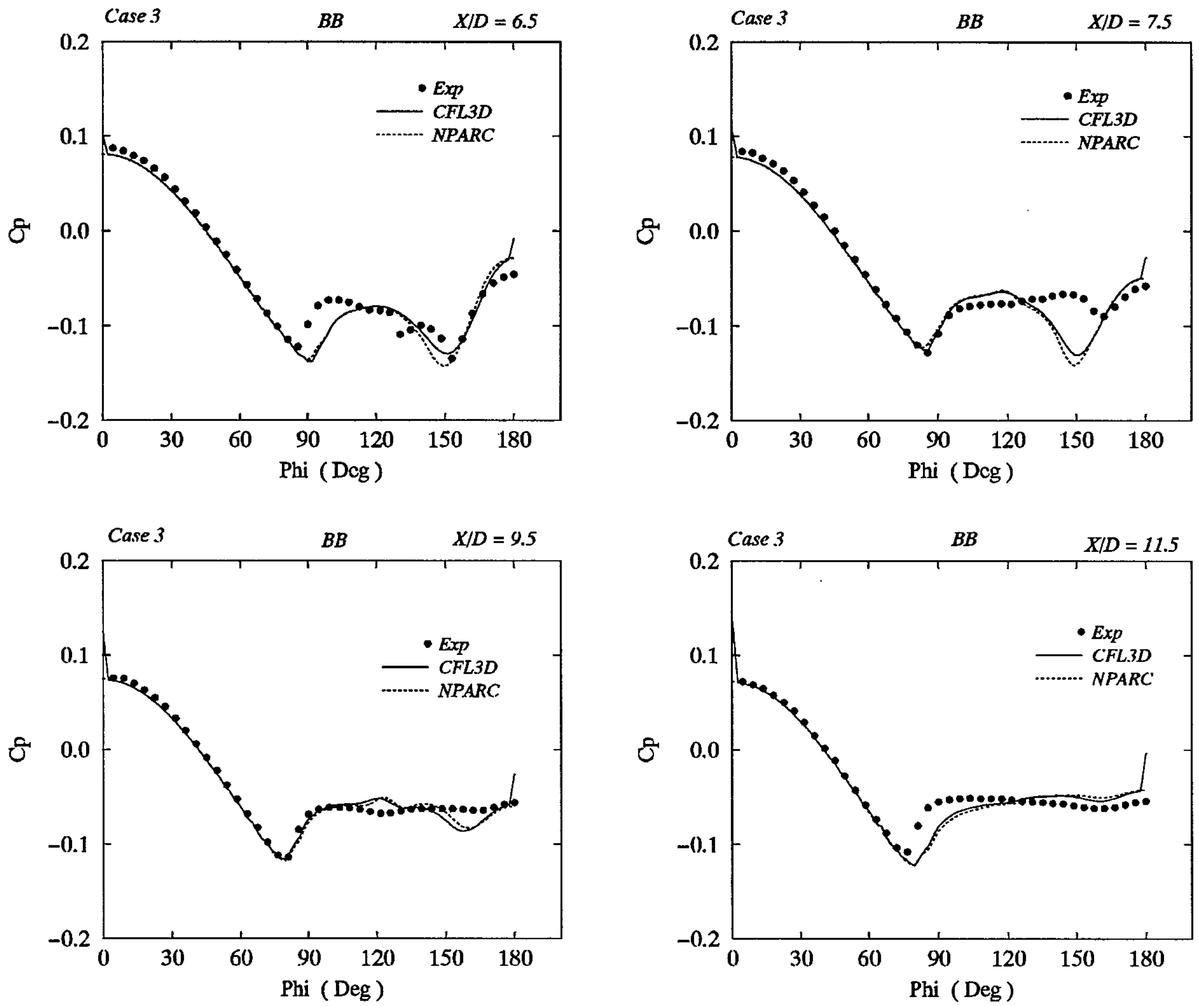

Figure 8(b) Baldwin–Barth TM Showing Comparison Between Both Codes

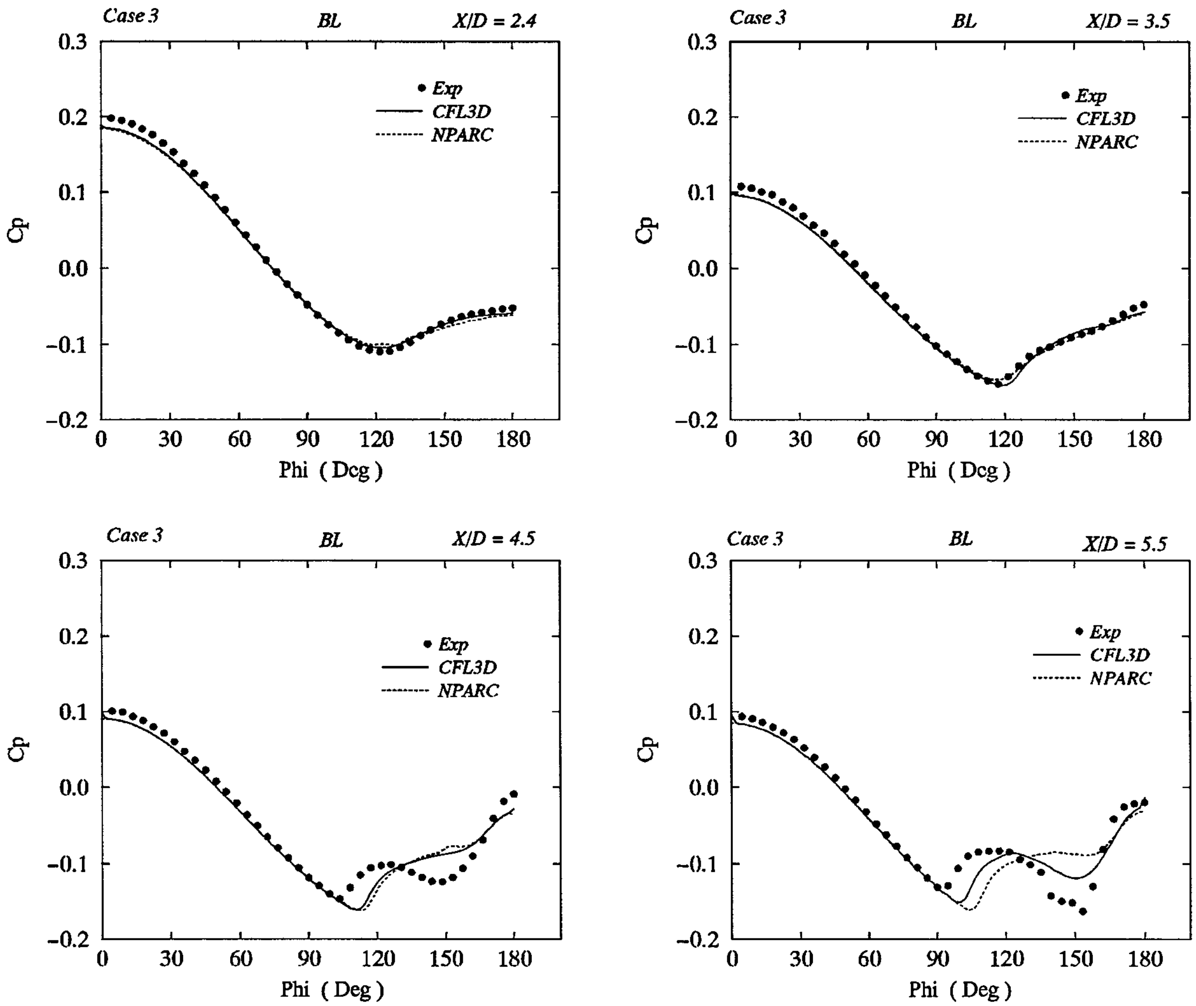

FGigure 9(a) Baldwin–Lomax TM Showing Comparison Between Both Codes

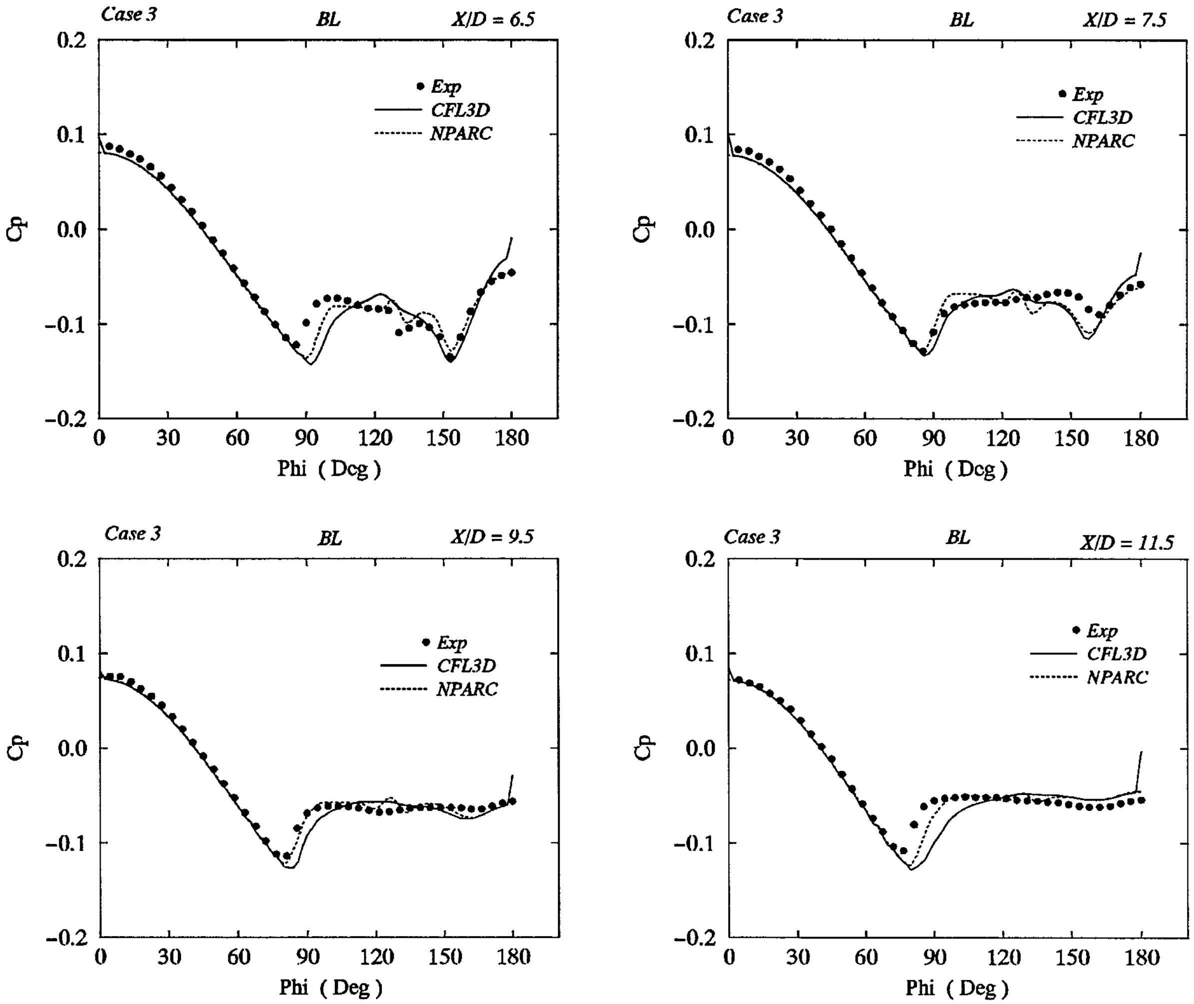

Figure 9(b) Baldwin–Lomax TM showing Comparison Between Both Codes

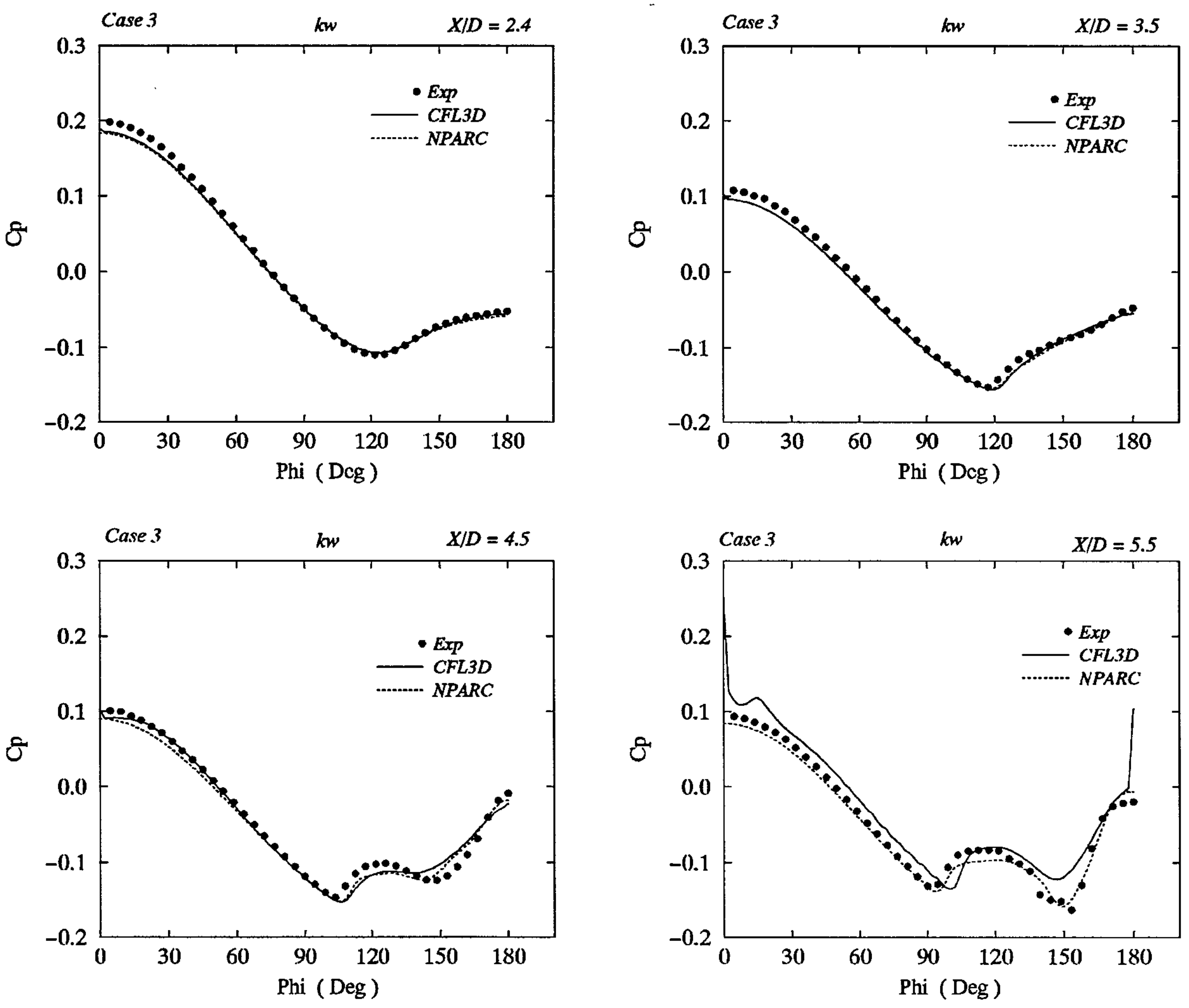

Figure 10(a) kw TM Showing Comparison Between Both Codes

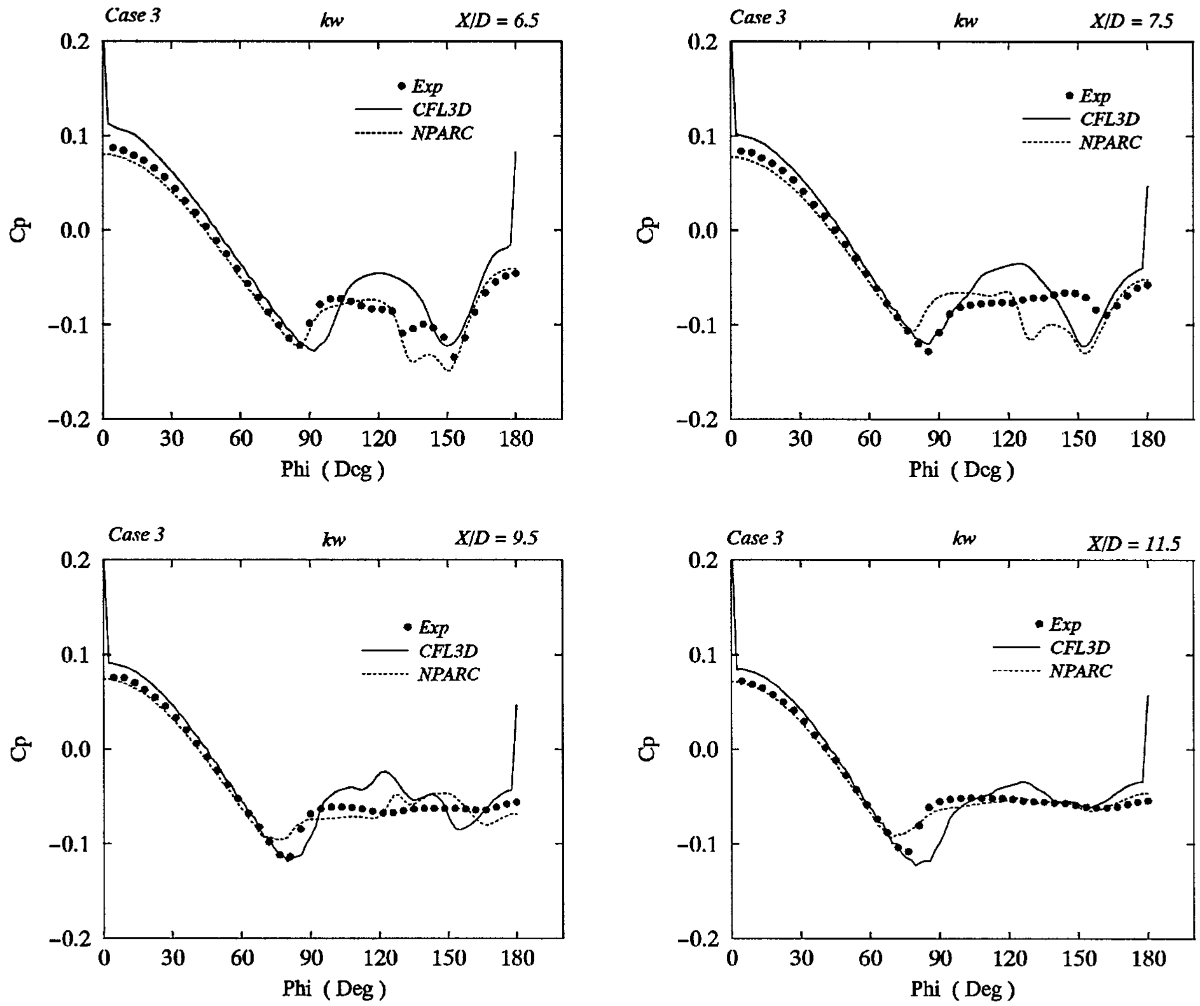

Figure 10(b) kw TM Showing Comparison Between Both Codes

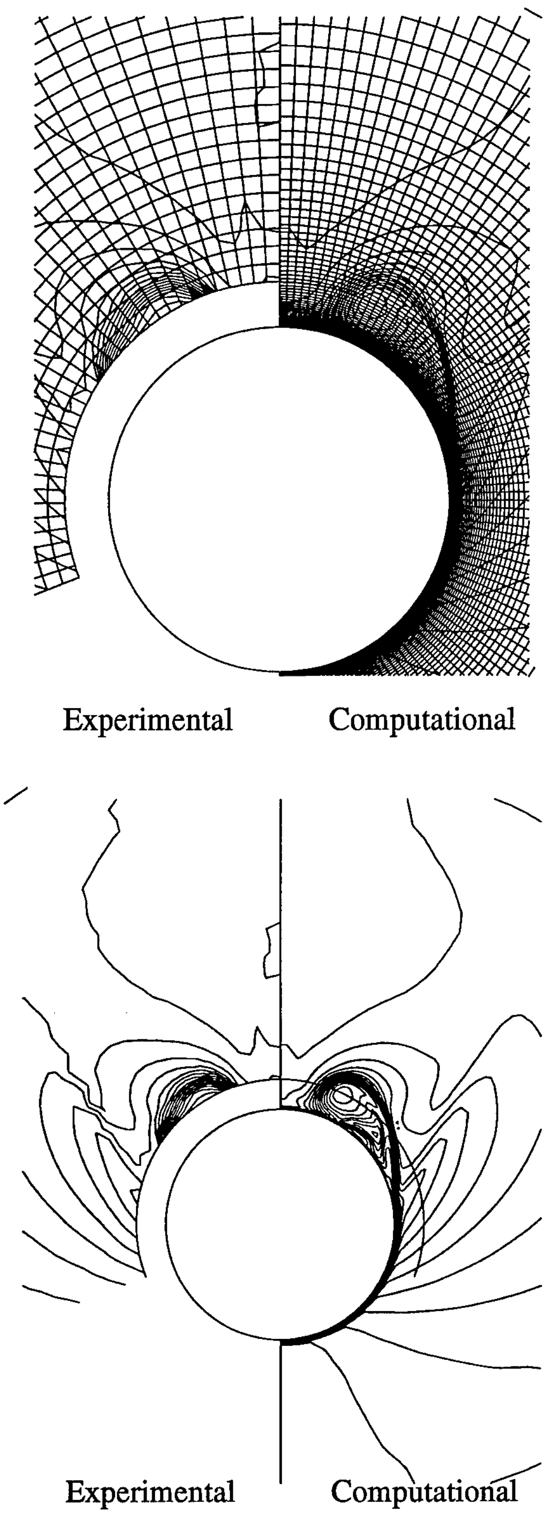

Figure 11 Comparison of Experimental and Computational Vortex Core for Case 3 at x/d = 5.5

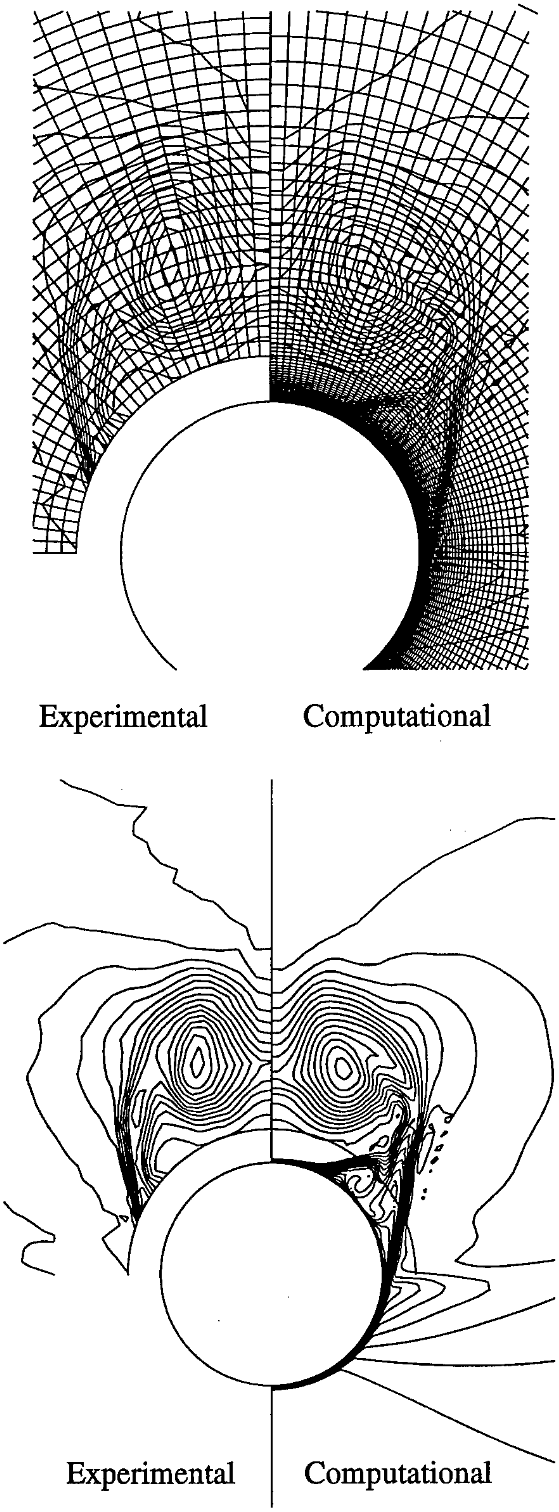

Figure 12 Comparison of Experimental and Computational Vortex Core for Case 3 at x/d = 11.5

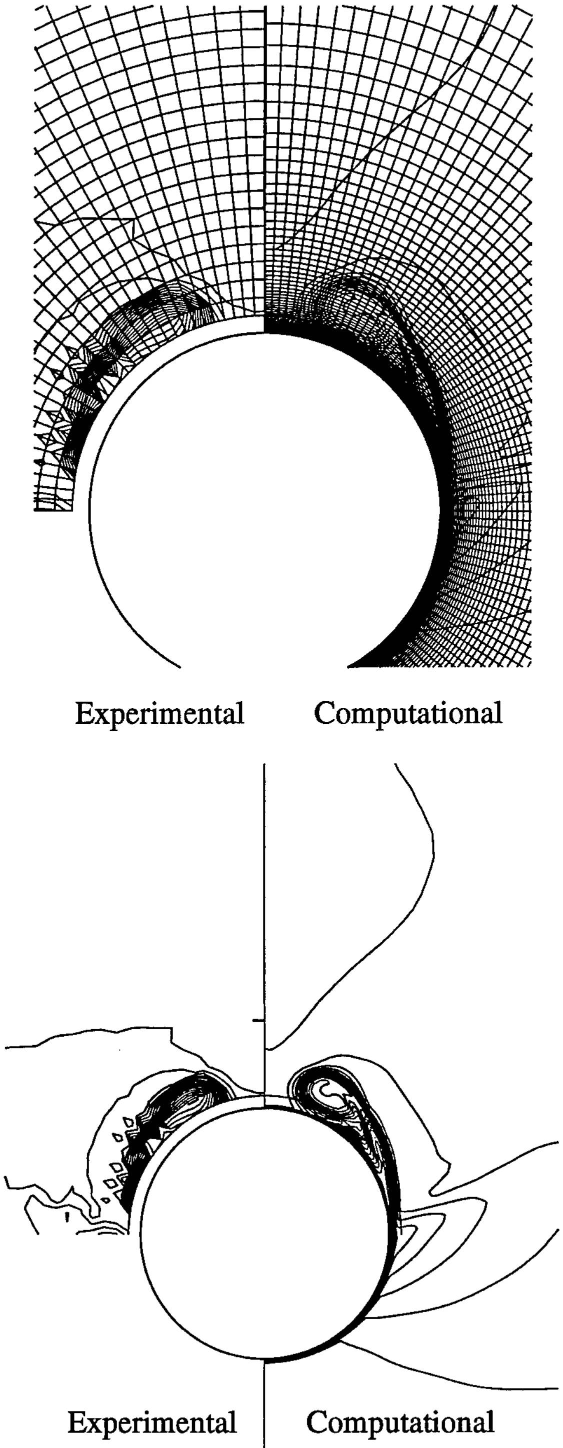

Figure 13 Comparison of Experimental and Computational Vortex Core for Case 2 at x/d = 5.5

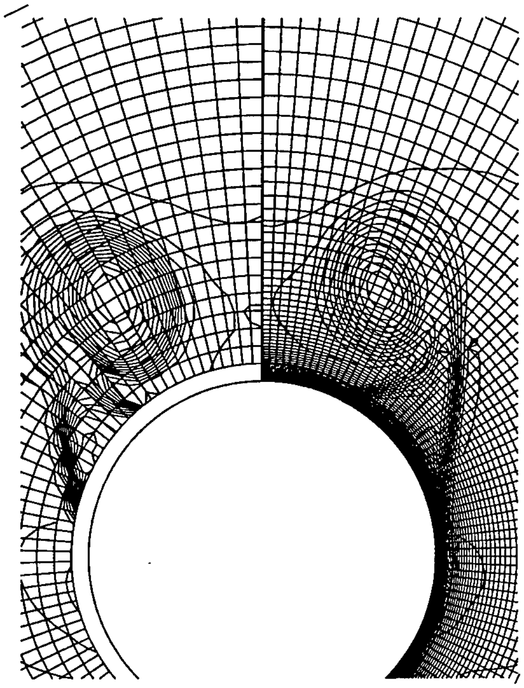

Experimental Computational

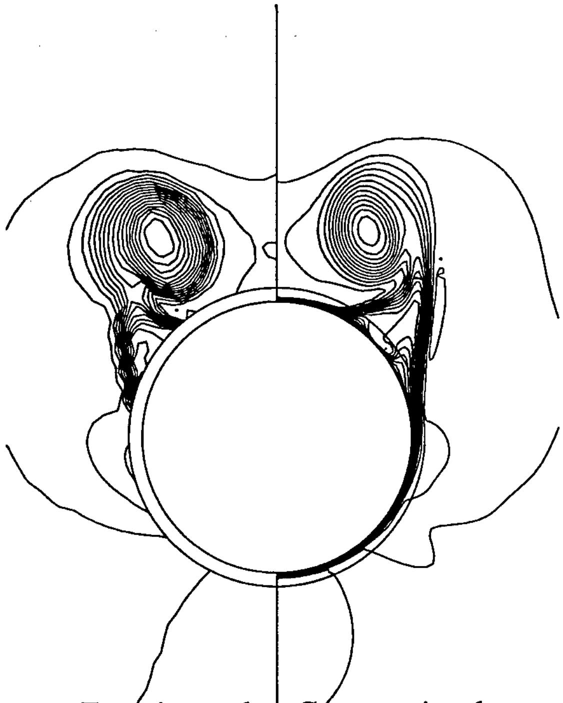

Experimental Computational

Figure 14 Comparison of Experimental and Computational Vortex Core for Case 2 at x/d = 8.5

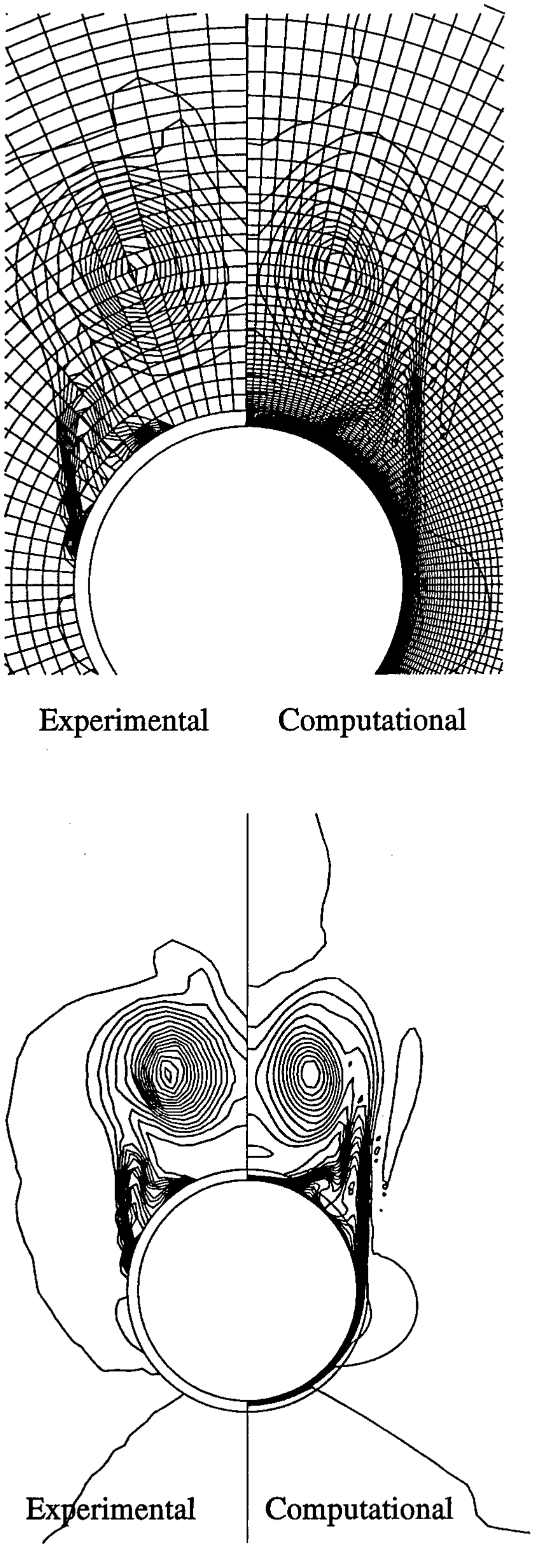

Figure 15 Comparison of Experimental and Computational Vortex Core for Case 2 at x/d = 11.5

5. GRID ADAPTATION

An adaptive grid system is developed to automatically redistribute grid lines based on an evolving flow solution. Solution adaptive schemes have demonstrated the ability to sharply capture shocks. Hence, in this work primary emphasis has been placed upon the ability of the procedure to capture in detail the feeding sheet and vortex definition. Using traditional grid generation methods it is difficult and very time consuming to align and cluster the grid with the feeding sheet, even if the location could be determined a priori. Appropriate clustering for crisp definition of the vortex core is also difficult. It is believed that if the available grid points were distributed in a near optimum manner then all seven grids would provide adequate spatial resolution. Use of the adaptive procedure has shown substantial improvement in flow solver convergence behavior and agreement with flow visualization pictures.

During this study, an adaptive grid system capable of automatically resolving complex flows with shock waves, expansion waves, shear layers and complex vortex–vortex and vortex–surface interactions has been developed. The weight functions developed utilize scaled derivatives and normalizing procedures to minimize or eliminate the need for user input. The grid redistribution scheme is based on the elliptic generation system with control functions governed by the assignment function.

The elliptic generation system:

$$\sum_{i=1}^{3}\sum_{j=1}^{3} g^{ij}\hat{r}_{\xi^i\xi^j} + \sum_{k=1}^{3} g^{kk}P_k\hat{r}_{\xi^k} = 0 \qquad (1)$$

where r : Position vector,
g^{ij} : Contravariant metric tensor
ξ^i : Curvilinear coordinate, and
P_k : Control function.

is widely used for grid generation [Thompson and Warsi 1985]. Control of the distribution and characteristics of a grid system can be achieved by varying the values of the control functions P_k in Equation 1. The application of the one dimensional form of Equation 1 combined with equidistribution of the weight function results in the definition of a set of control functions for three–dimensions.

$$P_i = \frac{(W_i)_{\xi^i}}{W_i} \quad (i = 1, 2, 3) \qquad (2)$$

These control functions were generalized by Eiseman [1983] as:

$$P_i = \sum_{j=1}^{3} \frac{g^{ij}}{g^{ii}}\frac{(W_i)_{\xi^i}}{W_i} \quad (i = 1, 2, 3) \qquad (3)$$

In order to conserve some of the geometrical characteristics of the original grid the definition of the control functions is extended as:

$$P_i = \left(P_{initialgeometry}\right) + c_i(P_{wt}) \quad (i = 1, 2, 3) \qquad (4)$$

where $P_{initial\ geometry}$: Control function based on initial geometry
P_{wt} : Control function based on

current solution
c_i : Constant weight factor.

These control functions are evaluated based on the current grid at a given time–step. This can be formulated as:

$$P_i^{(n)} = P_i^{(n-1)} + c_i(P_{wt})^{(n-1)} \quad (i = 1,2,3) \tag{5}$$

where

$$P_i^{(1)} = P_i^{(0)} + c_i(P_{wt})^{(0)} \quad (i = 1,2,3) \tag{6}$$

A flow solution is first obtained with an initial grid. Then the control function P_i is evaluated in accordance with Equations 2 and 5, which is a combination of the geometry of the current grid and the weight functions associated with the current flow solution.

The software in its current form inputs two PLOT3D format files [Buning 1985], one for the grid and one for the flow solution. Output consists of an NPARC restart file, as well as two PLOT3D files of the adapted grid and the flow solution interpolated onto the new grid. A multi–block treatment capability is included, but has not yet been validated. The adaptive grid is constructed in three steps. The first step is to generate the weight functions, which due to their critical importance will be discussed in detail in a separate section. The second step is to generate the actual adapted grid by equidistribution of the aforementioned weight function. In the current work this is accomplished by the numerical solution of Equation 1. A coupled three–dimensional strongly implicit procedure (CSIP) as described by Ghia et al. [1981] has been implemented for the solution of the discretized equations. Upwind differencing, with biasing based on the sign of the forcing functions, as well as central differencing has been implemented and studied for the first derivative terms. The first order upwind differencing increases the stability of the procedure, but at the expense of smearing the grid clustering. Hence, a hybrid upwind/central differencing scheme has been implemented to lessen this smearing while maintaining the smoothness and stability of the upwind procedure. Central differencing has been employed for all second and mixed derivative terms. All non–linear terms were treated by quasi–linearization. Boundary point movement was allowed through Neumann boundary conditions for plane surfaces, and by a NURBS fit and redistribution for curved surfaces. The NURBS redistribution is adapted from the GENIE++ code. For the curved surfaces the redistribution mesh was based on the nearest interior coordinate surface. Since Equation 1 is solved iteratively, the forcing functions must be evaluated for each new successive grid point location. The forcing functions are obtained by interpolation from the original grid. The interpolation procedure employed was that used for the non–matching block to block interface capability of the NPARC code. Upon convergence of this process the flow solution is interpolated onto the adapted grid using the same interpolation subroutine. Calculations can then be continued from the new restart file. This procedure can then be repeated until an acceptable solution is obtained. Experience indicates that coupling this procedure with a code capable of treating time accurate grid movement would ease this process and lessen the CPU requirements.

Application of the equidistribution law results in grid spacing inversely proportional to the weight function, and hence, the weight function determines the grid point distribution. Ideally, the weight would be the local truncation error ensuring a uniform distribution of error. For a given discretization the truncation error term contains derivatives of order greater than that of the solution order of accuracy. Evaluation of higher–order derivatives from discrete data is progressively less accurate and subject to noise. However lower–order derivatives must be non–zero in regions of wide variation of higher–order derivatives, and are proportional to the rate of variation. Therefore, it is possible to employ lower–order derivatives as a proxy for the truncation error. Determination of this function is one of the most challenging areas of adaptive grid generation.

Analysis of the weight functions explored to date indicates that density or velocity derivatives independently are not sufficient to represent the different types and strengths of flow features for viscous flows. Density or pressure for that manner varies insufficiently in the boundary layer to be used to construct weight functions for representation of these features. While velocity derivatives by themselves, for viscous flows, are dominated by the boundary layer, and additional variables must be included to represent other flow features. The present weight function consists of relative derivatives of density, and the three conservative velocities.

$$W^k_{i,j,k} = 1.0 + \frac{\left|\left(\hat{q}_{\xi k}\right)_{i,j,k} / \hat{q}_{i,j,k}\right|}{\left|\left(\hat{q}_{\xi k}\right)_{i,j,k} / \hat{q}_{i,j,k} + e\right|_{\max}} + \frac{\left|\left(\hat{q}_{\xi k \xi k}\right)_{i,j,k} / \hat{q}_{i,j,k}\right|}{\left|\left(\hat{q}_{\xi k \xi k}\right)_{i,j,k} / \hat{q}_{i,j,k} + e\right|_{\max}} \qquad (7)$$

$$\textit{where} \qquad \hat{q} = \{\varrho, \varrho u, \varrho v, \varrho w\}$$

The relative derivatives are necessary to detect features of varying intensity, so that weaker, but important structures such as vortices are accurately reflected in the weight function. One–sided differences are used at boundaries, and no–slip boundaries require special treatment since the velocity is zero. This case is handled in the same manner as zero velocity regions in the field. A small value, epsilon in the preceding equation, is added to all normalizing quantities. Also it appears that the Boolean sum construction method of Soni and Yang [1992] would more evenly balance the weight functions, as several features are reflected in multiple variables, while some are reflected in only one.

The weight function developed to represent the error associated with the discretization is presented in Figures 16, 17, and 18 for the NPARC, CFL3D and adapted NPARC calculations respectively. As can be seen from Figures 16, 17, and 18 the feeding sheet, and both primary and secondary vortices, as well as the strong shock at the nose are clearly visible. It can be seen in Figure. 18 that the solution has become much smoother and both the shock and feeding sheet are much sharper and clearer. Only structures that have been at least partially resolved by the flow solver can be detected by the weight function. Hence the quality of the weight function is dependent upon the quality of the solution.

Flow at Mach number 1.45 and 14 degree angle of attack has been simulated around the missile using the NPARC flow solver. The grid constructed for the second cycle of adaption using the hybrid differencing scheme for the grid equations is presented in Figure 19. Figure 20 presents a side by side comparison of the grid after two and three adaptation cycles. The alignment of the grid lines with the flow structures of interest is clearly visible. It can be seen that the grid, and, hence, the solution varies substantially from the second to the third cycle. The adaption procedure and the flow solver should be coupled so that the evolving grid can continuously reflect features that are detected as the solution develops and improves due to adaptation. This should increase the efficiency of the procedure.

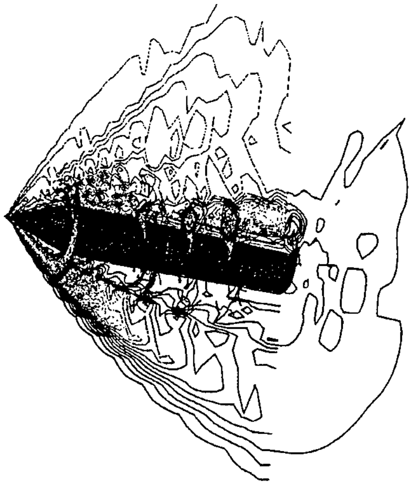

Figure 16 Weight Function Based Upon Original NPARC Solution.

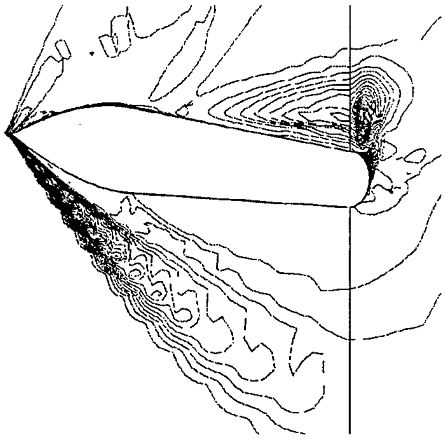

Figure 17 Weight Function Based Upon Original CFL3D Solution.

The results shown demonstrate the capability of the procedure to detect and resolve shocks of differing strengths, primary and secondary vortices, and shear layers adequately. The use of adaptive re–meshing allows the use of larger time steps resulting in increased convergence. However, the single greatest benefit resulting from the adaptive procedure is a dramatic lowering of the artificial viscosity parameters required for stability. This results in off surface structures which are much sharper and more closely resemble the flow visualization. No special treatment is needed for boundary layers and no user input is required. In fact, the normal spacing for the first point off the wall on the windward side was reduced to on the order of 10^{-6} from on the order of 10^{-4} by the adaptation procedure. It should be noted that this is due primarily to the decrease in boundary layer thickness as the artificial dissipation values were lowered.

As discussed previously, it is imperative that the adaptation process be coupled with the flow solver as experience indicates that complex flowfields may require dozens of adaptive cycles. This is par-

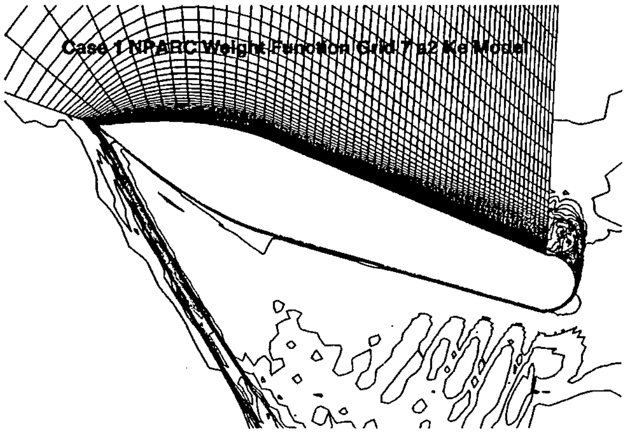

Figure 18 Weight Function Upon Adapted NPARC.

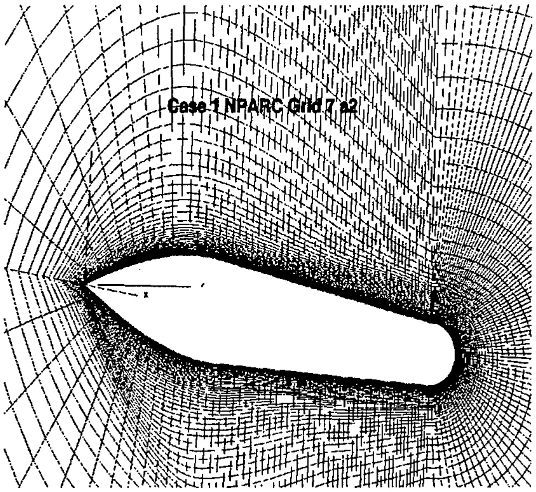

Figure 19 Adapted grid after two cycles.

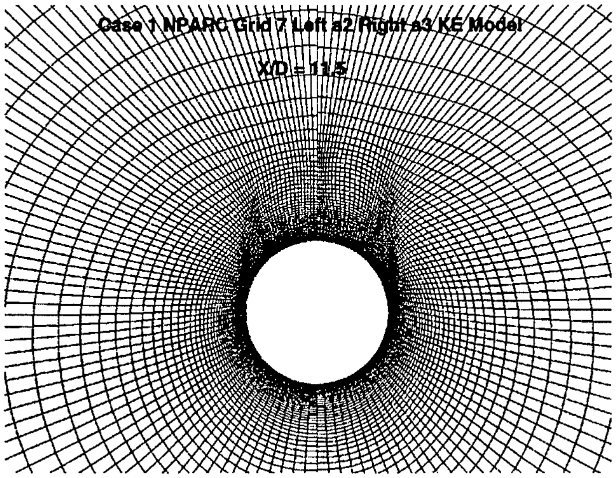

Figure 20 Comparison of adapted grid after two and three cycles.

ticularly critical for flow fields that are initially poorly resolved. Also, the interpolation procedure for updating the forcing functions, which is very time consuming and often a source of trouble, would be eliminated.

Currently, simple multi–block problems are being simulated to evaluate this capability. Attention is being placed upon across block scaling for the weight functions. A global maximum across all blocks seems to work well for the normalization of weight function components. However, this issue is being monitored as more complex problems are attempted. A further problem arises due to equidistribution via forcing functions. This does not appear to be a problem where a block face is connected to one and only one face of another block. Problems have been encountered for a multi–block launch vehicle computation where a block face consisted of a block to block connection and a solid surface for the base region. A smooth, continuous set of forcing functions across this block boundary does not yield a smooth grid. It is believed that this is due to the elliptic character of the grid equations. The simple fix is to introduce artificial block boundaries to force one to one correspondence.

Use of the adaptive process with the NPARC flow solver did improve the convergence level, agreement with flow visualization, and the agreement of the force and moment coefficients with the experimental data. The promising initial success indicates that with the enhancements proposed significant further improvements can be obtained. It is proposed to work on block interface issues as well as coupling with flow solvers, unsteady flows, and more complex multi–block problems.

The simulation results for grid adaptation are presented in Figures 21–31.

From the grid adaption study it was concluded that the results are different than the unadapted one. However, not clear improvement in matching experimental pressure data. The vortex sheet and the shock structure is better pronounced in adaptive solution is in good agreement with the experimental data. Further work is needed in grid adaptation and grid optimization. However, there is a remarkable improvement in the simulated values of normal force and moment coefficients using adapted grid as compared to the unadapted grid. The calculated values of these coefficients are compared with the experimental data in Table 4.

Forces	Experimental Data	Unadapted (NPARC, BL)	Adapted (NPARC, BL)
Axial	0.1957	0.3307	0.3309
Normal	1.9100	1.8855	1.9052
Moment	10.2417	10.0314	10.2666

Table 4. Forces/Moments Comparison

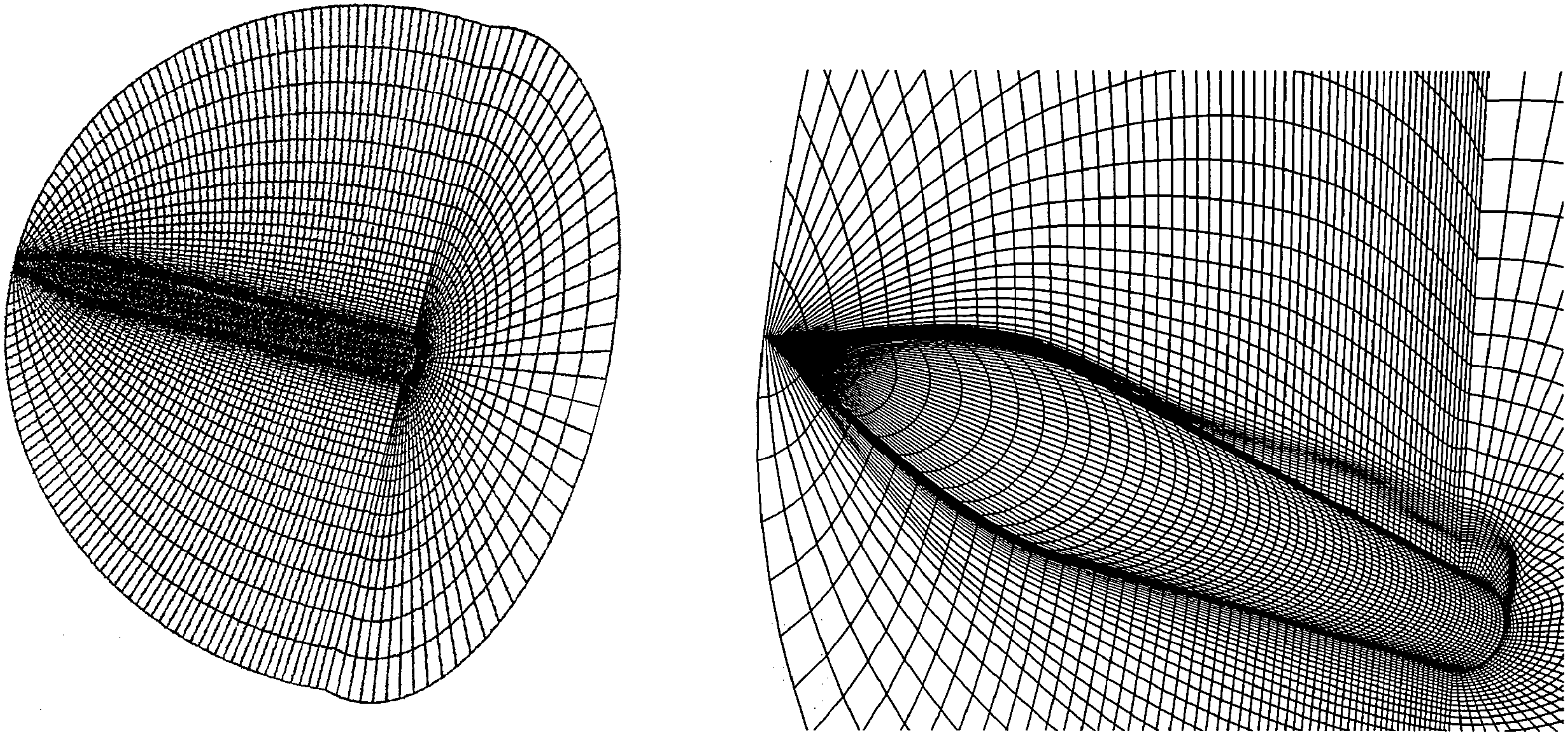

Undapted

Adapted

Figure 21 Comparison of Unadapted and Adapted Grid

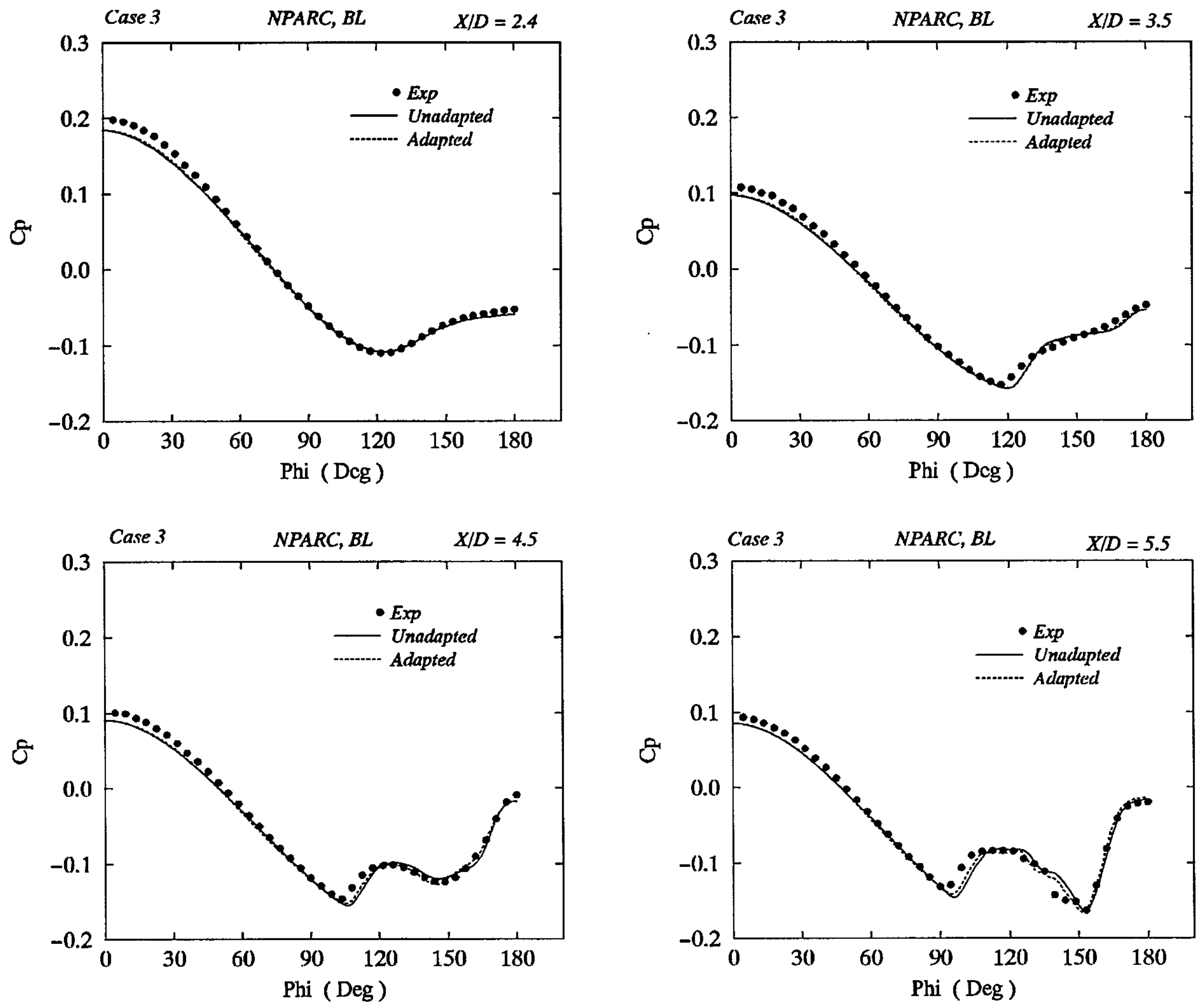

Figure 22(a) Comparison of Unadapted and Adapted Solution for Case 3

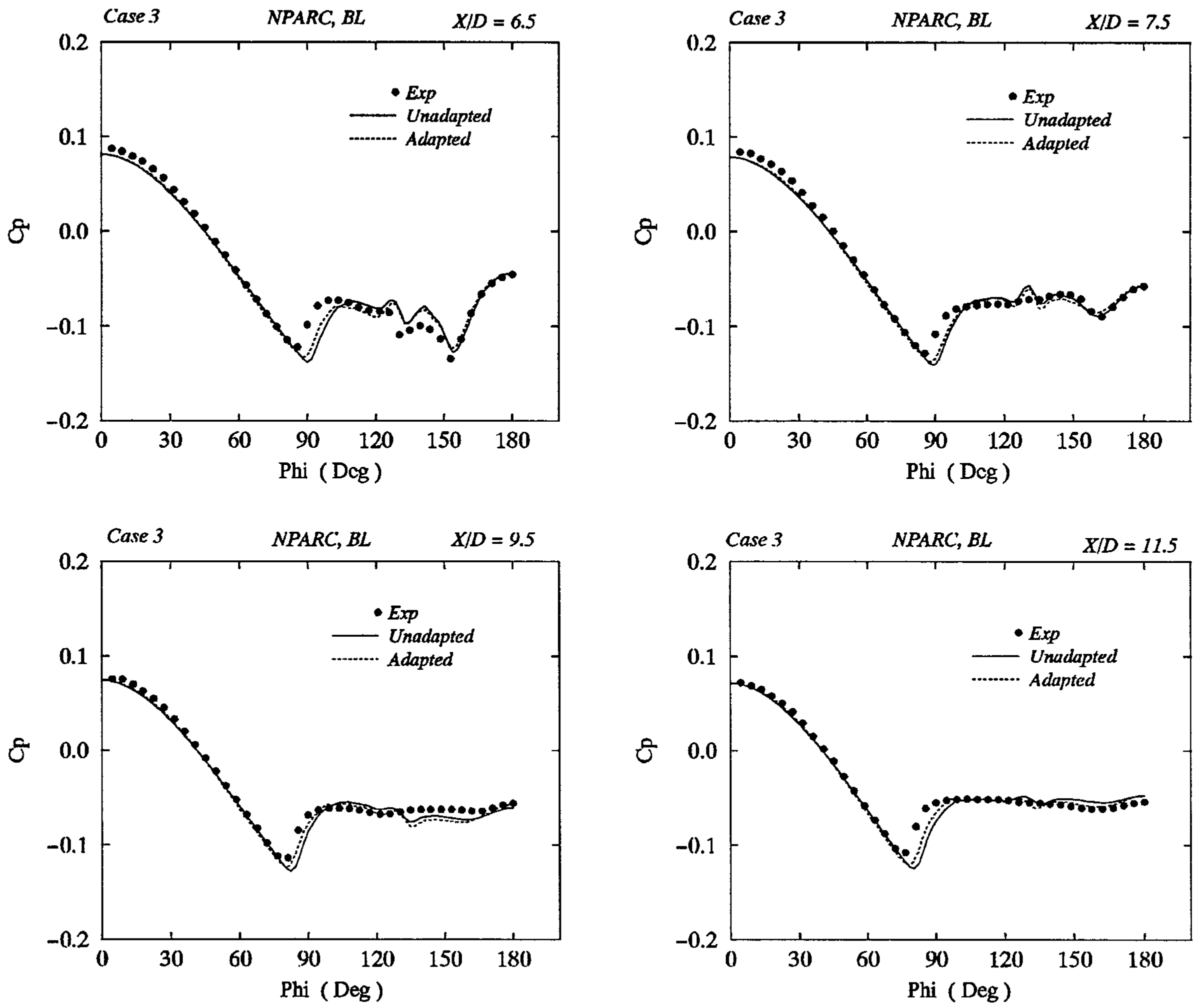

Figure 22(b) Comparison of Unadapted and Adapted Solutions for Case 3

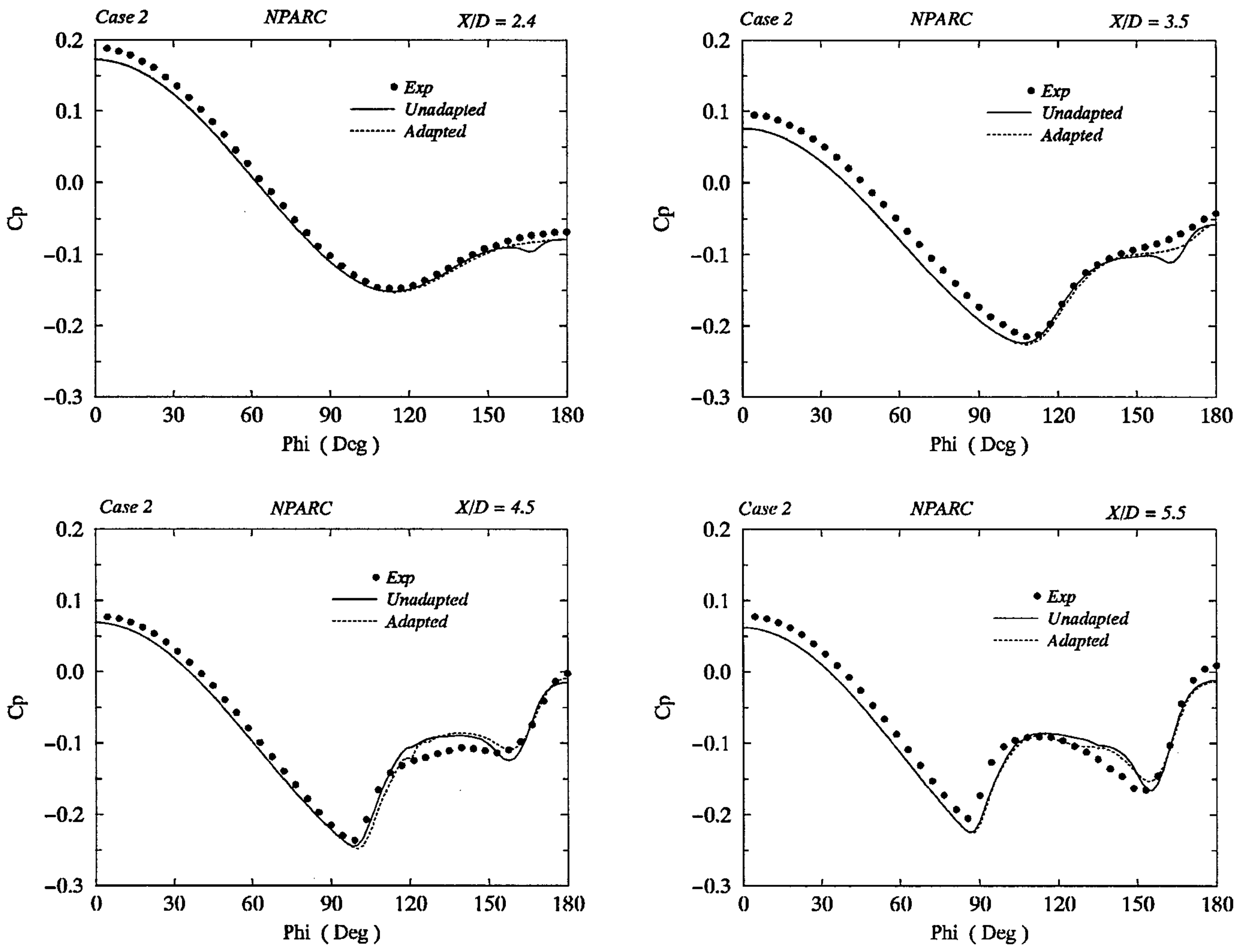

Figure 23(a) Comparison of Unadapted and Adapted Solutions for Case 2

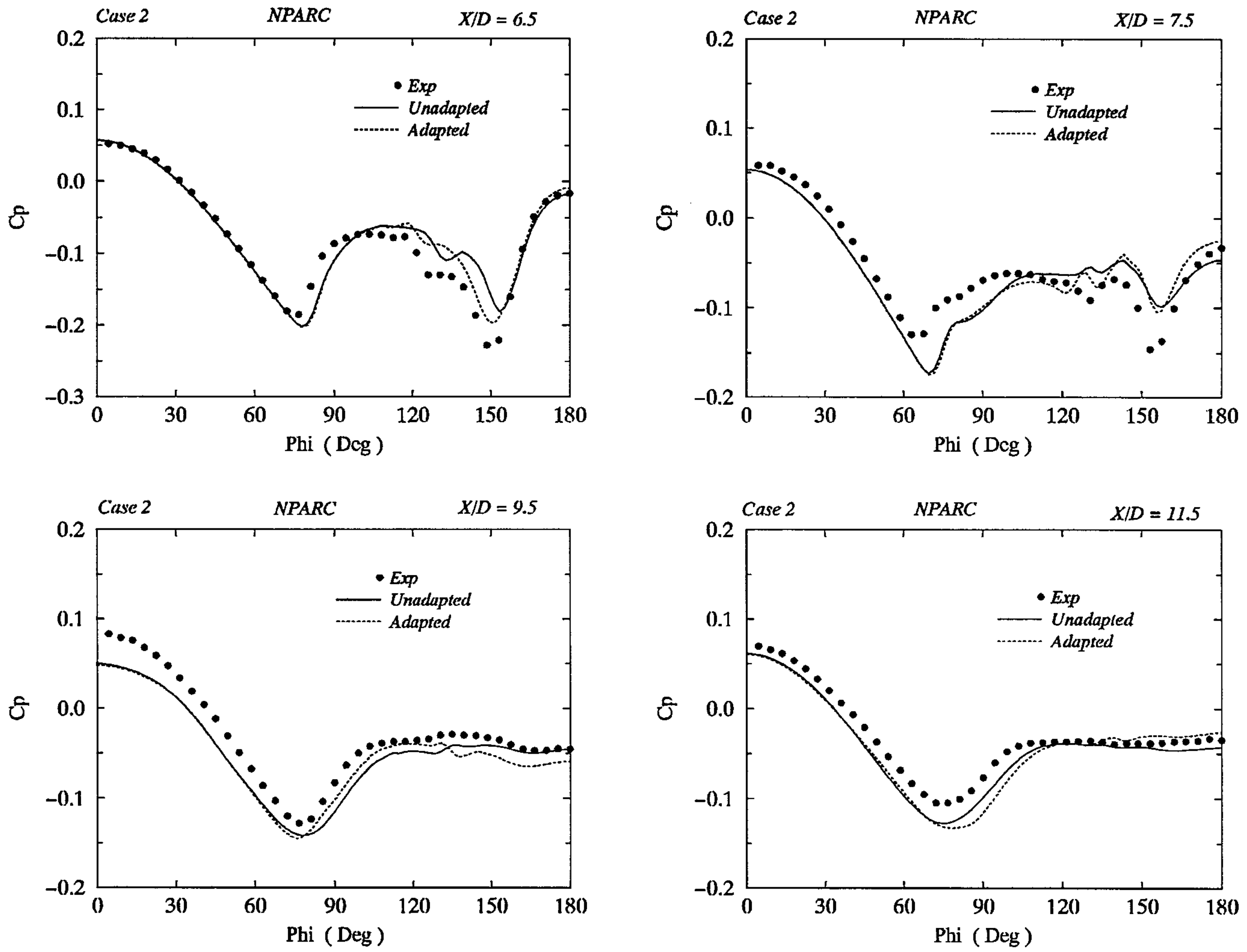

Figure 23(b) Comparison of Unadpted and Adapted Solutions for Case 2

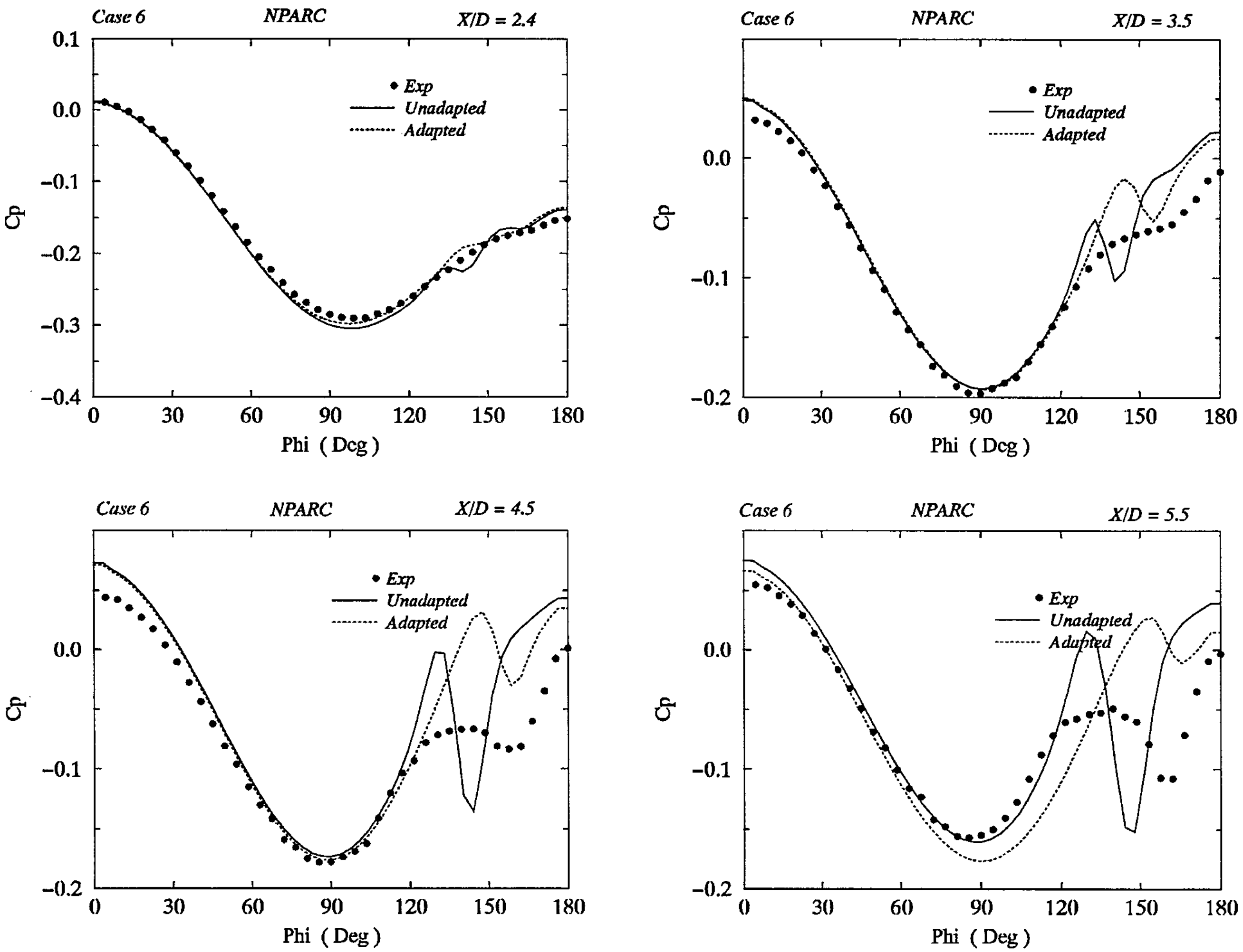

Figure 24(a) Comparison of Unadapted and Adapted Solution for Case 6 (Euler)

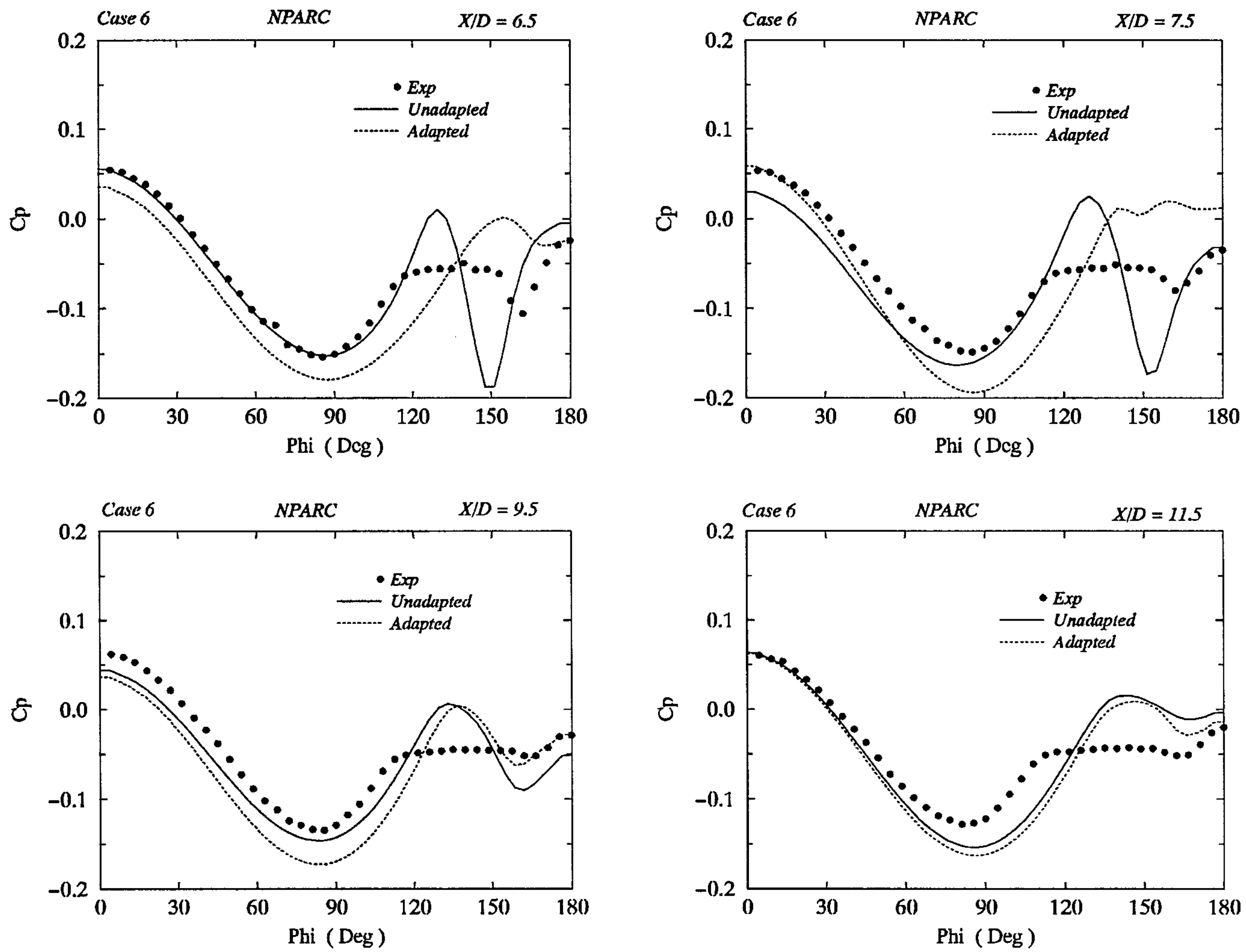

Figure 24(b) Comparison of Unadapted and Adapted Solutions for Case 6 (Euler)

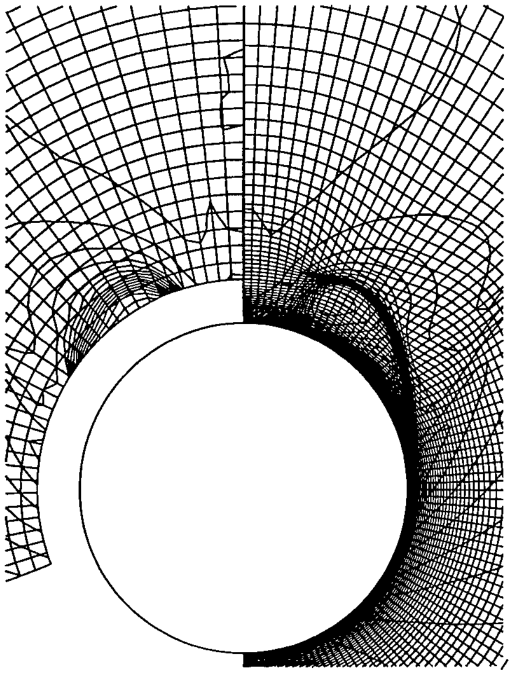

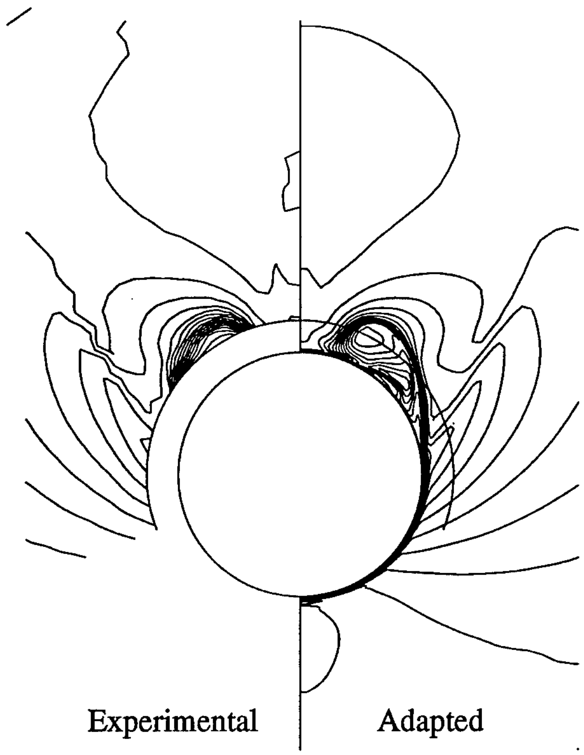

Figure 25 Comparison of Experimental and Computational (Adapted) Vortex Core for Case 3 at x/d = 5.5

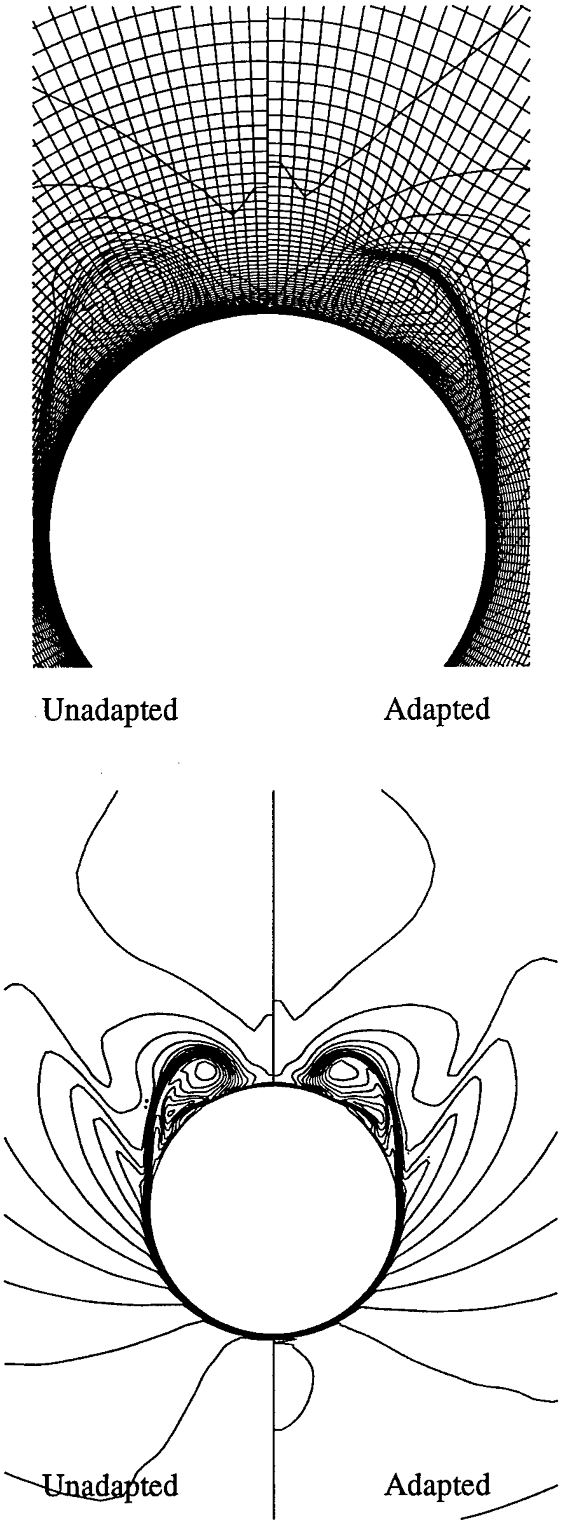

Figure 26 Comparison of Unadapted and Adapted Vortex Core for Case 3 at x/d = 5.5

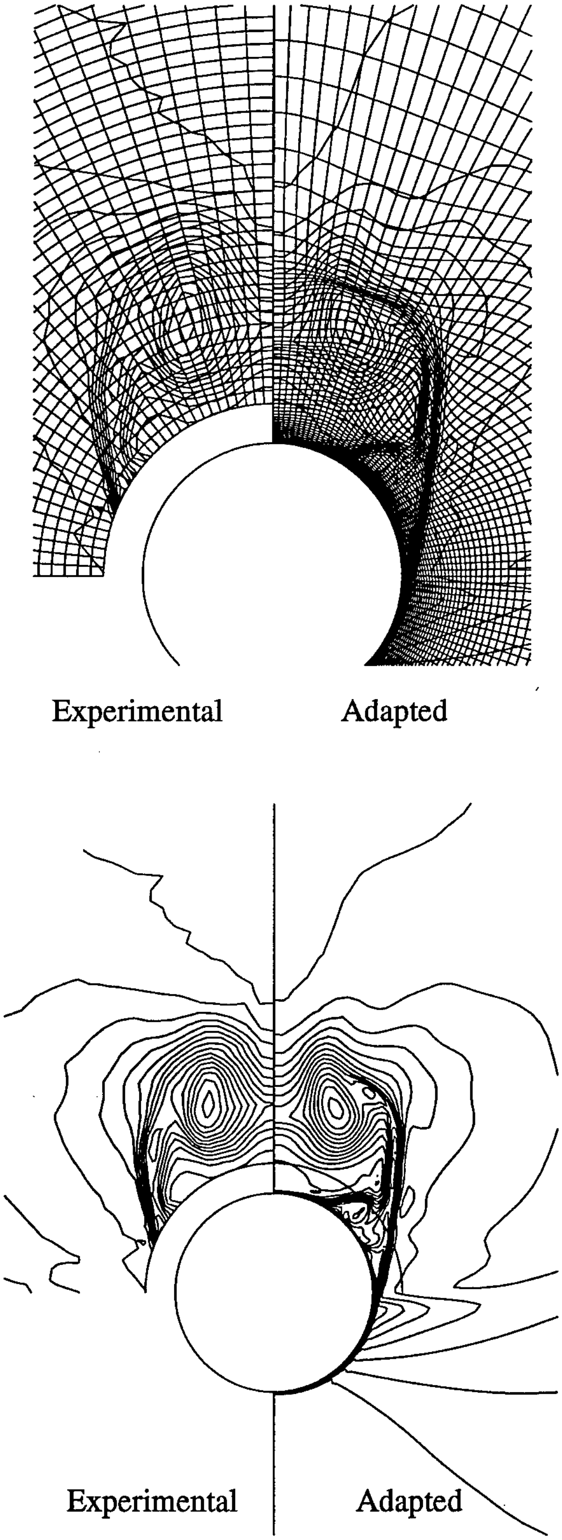

Figure 27 Comparison of Experimental and Computational (Adapted) Vortex Core for Case 3 at x/d = 11.5

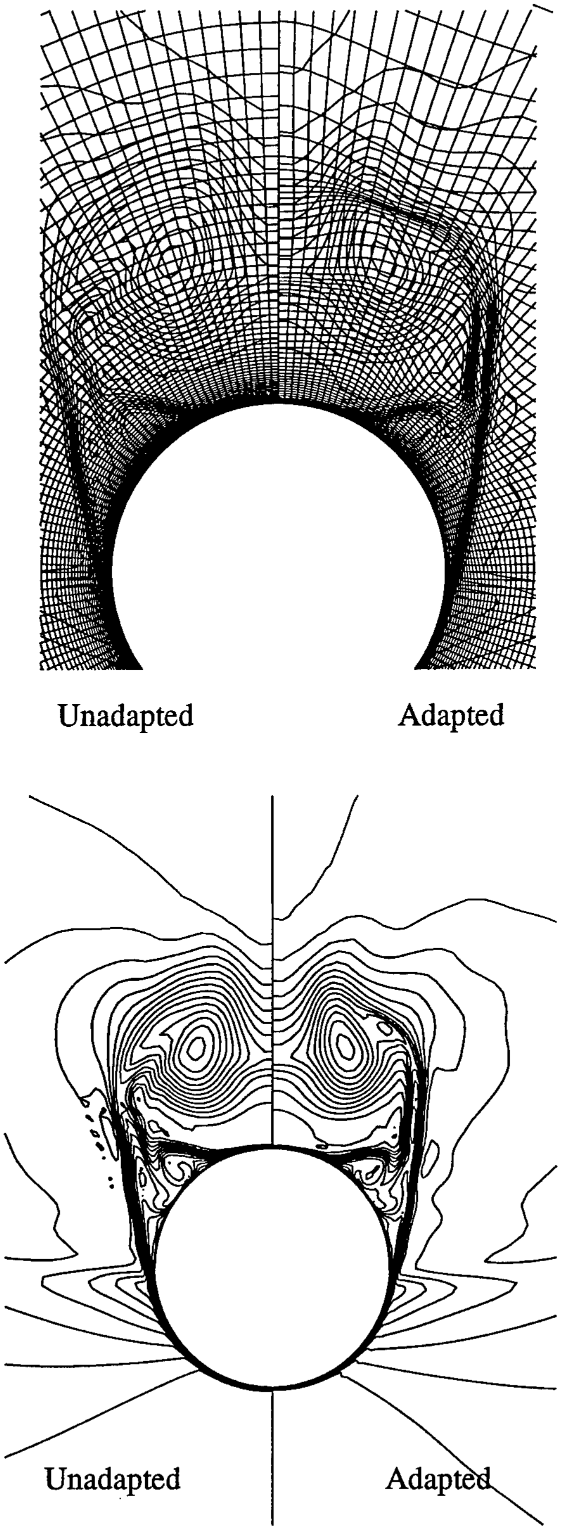

Figure 28 Comparison of Unadapted and Adapted Vortex Core for Case 3 at x/d = 11.5

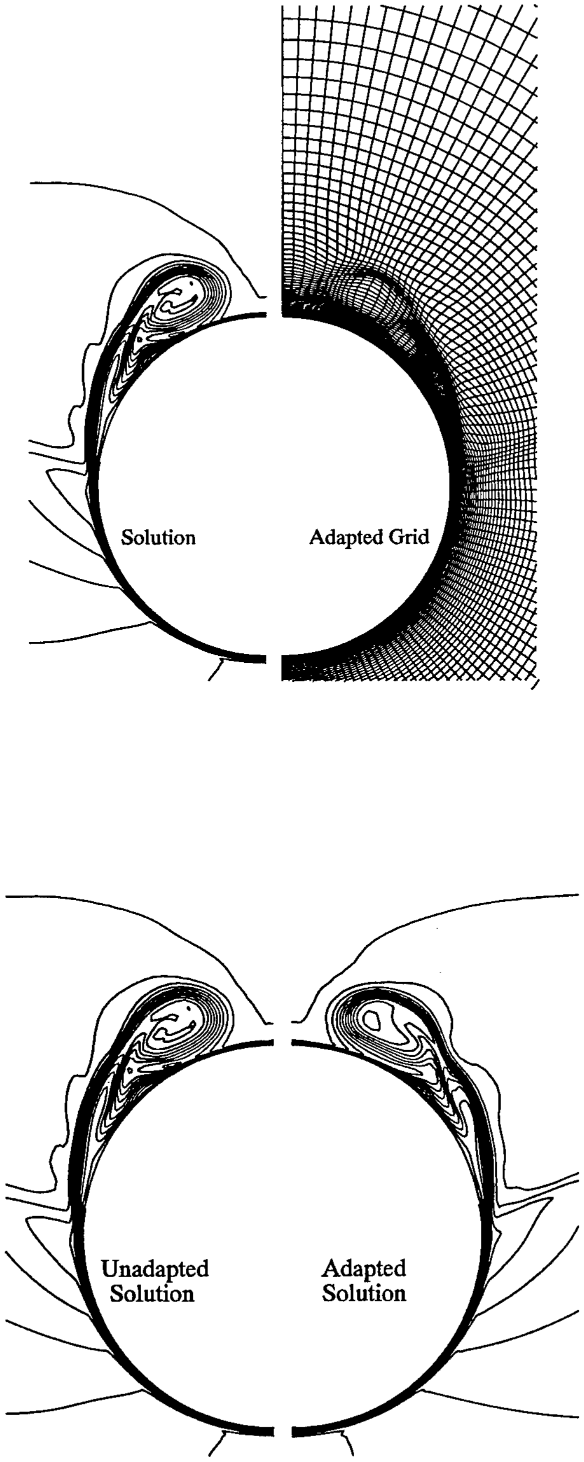

Figure 29 Comparison of Unadapted and Adapted Vortex Core for Case 3 at x/d = 5.5

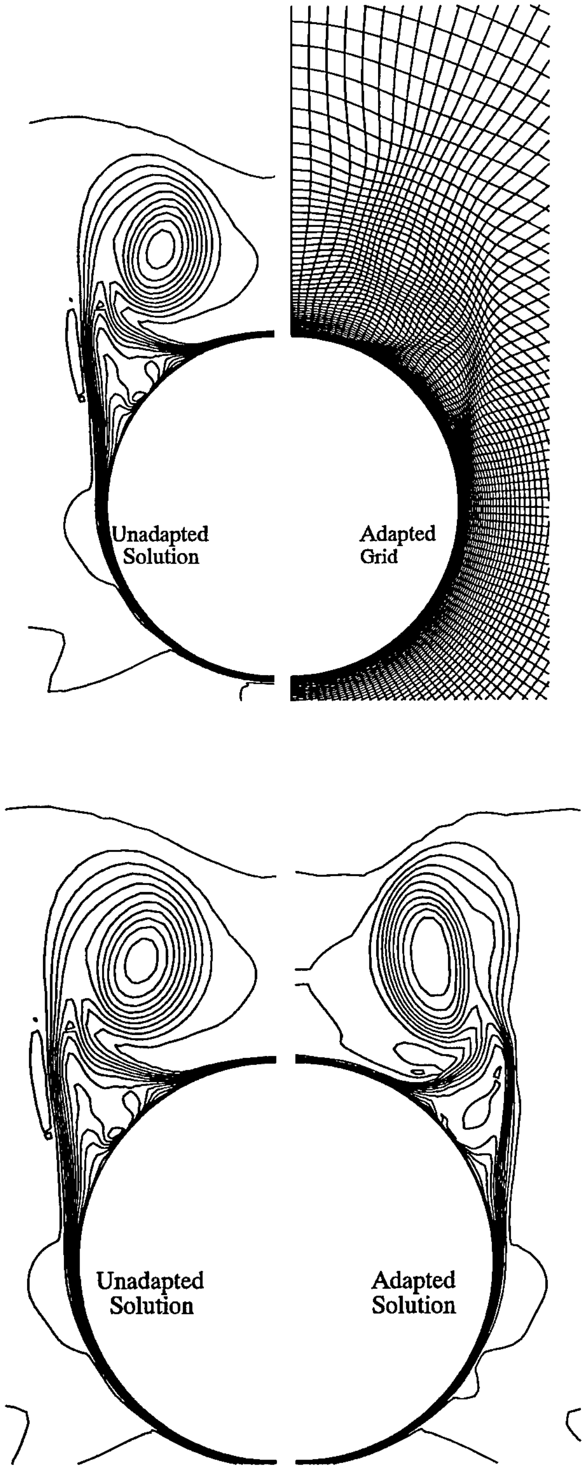

Figure 30 Comparison of Unadapted and Adapted Vortex Core for Case 3 at x/d = 5.5

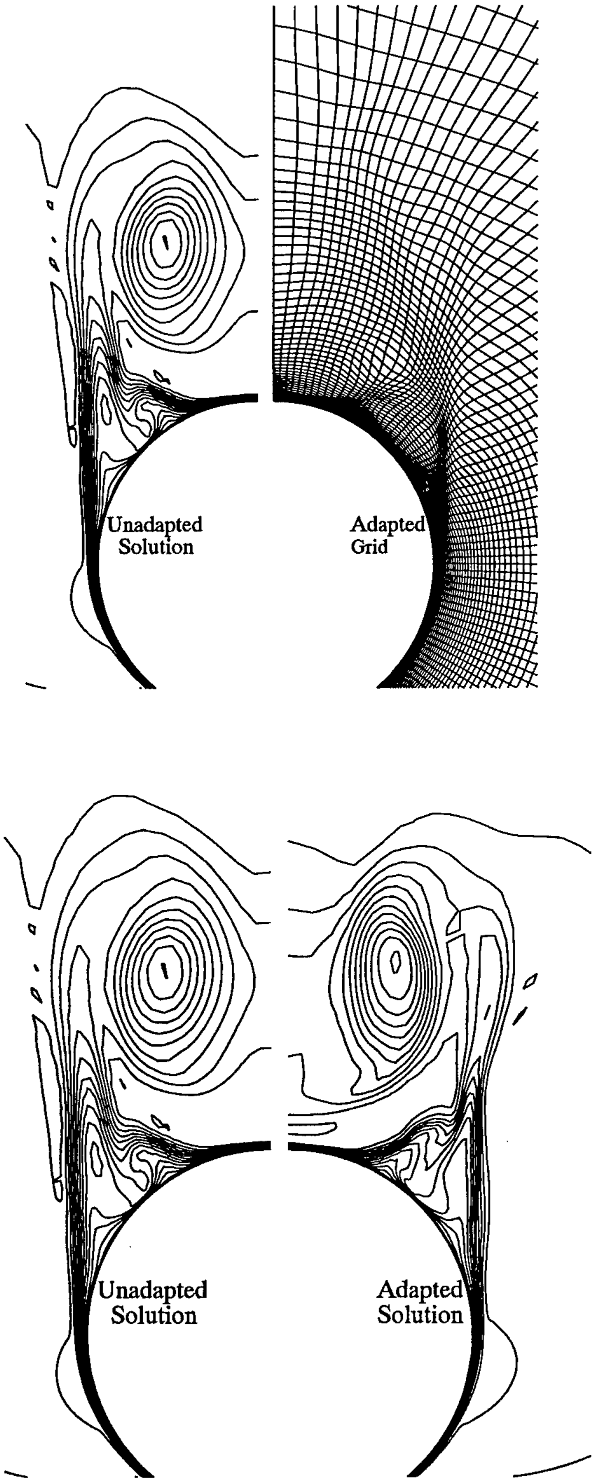

Figure 31 Comparison of Unadapted and Adapted Vortex Core for Case 3 at x/d = 5.5

6. CONCLUSION

The CFD simulations performed utilizing the flow solvers: NPARC and CFL3D were submitted to the KTA2–12 team. Nine different CFD codes were exercised by the KTA team in all six cases. However, the concentration was placed on case 3 (Mach=2.5, AOA=14) for the reporting and comparison purpose. Qualitatively, consistent results were obtained by all these codes. Also, no best turbulence model could be identified as of result of these simulations in view of comparison with experimental data. A technical paper summarizing this program has been written and was presented at the AIAA conference. The paper entitled, "The Application of CFD to the Prediction of Missile Body Vortices" is included in the Appendix A.1 of this report.

An adaptive grid strategy has been developed and grid adaptation was performed to evaluate the influence on simulation. Little variation was observed in the surface pressure coefficients due to adaptation. However, the vortex core resolution was crisp and the forces and moments indicated better agreement because of adaptation. Further work in grid adaptation is needed to evaluate effect of the grid adaptation on simulations. The development of weight function and detailed study of grid adaptation has been reported in a technical paper entitled, "A Structured Grid Based Solution–Adaptive Technique for Complex Separated Flow". This paper has been accepted for the publication in the *Journal of Applied Mathematics and Computation* and is included in the Appendix A.2 of this report.

REFERENCES

1. Anderson, D.A., (1987), Equidistribution schemes, Poisson generators, and adaptive grids, *Appl. Math. Comput. 24,* 211–227.

2. Anderson, D.A., “Adaptive Grid Methods for Partial Differential Equations,” *Advances in Grid Generation,* ASME Fluids Engineering Conference, Houston, 1983.

3. Benson, Rusty A., and McRae, D. Scott, “Time–Accurate Simulations of Unsteady Flows With A Dynamic Solution–Adaptive Grid Algorithm,” *Numerical Grid Generation in Computational Fluid Dynamics and Related Fields, (1994)* (Pineridge Press Limited, Swansea, U.K.) Ed. N.P. Weatherill, P.R. Eiseman, J. Hauser, J.F. Thompson.

4. Bockelie, M.J. (1988) Adaptive grid movement schemes and the numerical simulation of shock vortex interaction, *Ph.D. Thesis,* Columbia University, New York.

5. Brackbill, J.S., “Application and Generalization of Variational Methods for Generating Adaptive MEshes,” *Numerical Grid Generation*, Edited by J.G. Thompson, Elsevier Science Publishing Company, 1985.

6. Brackbill, J.U. and J. Saltzman (1982) Adaptive zoning for singular problems in two dimensions, *J. Comput. Phys. 46,* 342–368.

7. Buning, P.G. and Steger, J.L., ”Graphics and Flow Visualization in Computational Fluid Dynamics,” AIAA Paper 85–1507–CP, Proceedings of the AIAA 7th Computational Fluid Dynamics Conference, 1985.

8. Catherall, D., “An Assessment of the Advantages of Adaptivity on Structured Grids,” *Numerical Grid Generation in Computational Fluid Dynamics and Related Fields, (1994)* (Pineridge Press Limited, Swansea, U.K.) Ed. N.P. Weatherill, P.R. Eiseman, J. Hauser, J.F. Thompson.

9. Dwyer, H.A., ”Grid Adaption for Problems in Fluid Dynamics,” AIAA Journal, vol. 22. No. 12, pp. 1705–1712, December 1984.

10. Eiseman, P.R., ”Alternating Direction Adaptive Grid Generation,” AIAA Paper 83–1937, 1983.

11. Ghia, K.N., Ghia, U., Shin, C.T. and Reddy, D.R., ”Multigrid Simulation of Asymptotic Curved–Duct Flows Using a Semi–Implicit Numerical Technique,” Computers in Flow Prediction and Fluid Dynamics Experiments, ASME Publication, New York 1981.

12. Hagmeijer, R., (1993) “Anisotropic Grid Adaption Based on Diffusion Equations,” *Numerical Grid Generation in Computational Fluid Dynamics and Related Fields, (1994)* (Pineridge Press Limited, Swansea, U.K.) Ed. N.P. Weatherill, P.R. Eiseman, J. Hauser, J.F. Thompson.

13. Hsieh, T., Wardlaw, A.B. and Birch, T.J., ”Vortical Flows about a Long Ogive–Cylinder at $M=3.5$ and $\alpha=18^{0}$”, AIAA–91–1808, AIAA 22nd Fluid Dynamics, Plasma Dynamics and Lasers Conference, Honolulu, Hawaii, June 24–26, 1991.

14. Jones, W.P., Menzies, K.R., “An Adaptive Grid Redistribution Scheme and its Application to Incompressible Recirculating Fluid Flow Calculations,” *Numerical Grid Generation in Computational Fluid Dynamics and Related Fields, (1994)* (Pineridge Press Limited, Swansea, U.K.) Ed. N.P. Weatherill, P.R. Eiseman, J. Hauser, J.F. Thompson.

15. Kim, H.J. and J.F. Thompson (1990), Three–dimensional adaptive grid generation on a composite–block grid, *AIAA J.* 28 470–477.

16. NASA LeRC and USAF AEDC, ”NPARC 1.0 User Notes,” June 1993.

17. NASA LaRC, ”User Document for CFL3D/CFL3DE (Version 1.0)”, 1993.

18. Niederdrenk, Peter, “Grid Adaptation to Multiple Auto–scaled Solution Features,” *Numerical Grid Generation in Computational Fluid Dynamics and Related Fields, (1994)* (Pineridge Press Limited, Swansea, U.K.) Ed. N.P. Weatherill, P.R. Eiseman, J. Hauser, J.F. Thompson.

19. Pagan, D. and Molton, P., ”Basic Experiment on a Supersonic Vortex Flow Around a Missile Body,” AIAA–91–0287, 29th Aerospace Sciences Meeting, Reno, NV, Jan. 7–10, 1991.

20. Shih, M.H., “Towards A Comprehensive Computational Simulation System for Turbomachinery”. Dissertation, Mississippi State University, May, 1994.

21. Soni, B.K., “Algebraic Methods and CAGD techniques in Structured Grid Generation,” *Proceedings of the Fourth International Conference of Numerical Grid in CFD,* Swansea, Wales, April 1994.

22. Soni, B.K., Weatherill, N.P. and Thompson, J.F., ”Grid Adaptive Strategies in CFD,” International Conference on Hydo Science and Engineering, Washington, D.C., June 7–11, 1993.

23. Soni, B.K. and Yang, J.C., ”General Purpose Adaptive Grid Generation System,” AIAA–92–0664, 30th Aerospace Sciences Meeting, Reno, NV, Jan. 6–9, 1992.

24. Soni, B.K., Thompson, J.F., Stokes, M.L. and Shih, M.H., ”GENIE++, EAGLEView and TIGER: General and Special Purpose Interactive Grid Systems,” AIAA–92–0071, 30th Aerospace Sciences Meeting, Reno, NV, Jan. 6–9, 1992.

25. Sweby, P.K, and Yee, H.C., “On The Dynamics of Some Grid Adaption Schemes,” *Numerical Grid Generation in Computational Fluid Dynamics and Related Fields, (1994)* (Pineridge Press Limited, Swansea, U.K.) Ed. N.P. Weatherill, P.R. Eiseman, J. Hauser, J.F. Thompson.

26. Takahashi, Satoshi, Eiseman, Peter R., “Adaptive Grid Movement with Respect to Boundary Curvature,” *Numerical Grid Generation in Computational Fluid Dynamics and Related Fields, (1994)* (Pineridge Press Limited, Swansea, U.K.) Ed. N.P. Weatherill, P.R. Eiseman, J. Hauser, J.F. Thompson.

27. Thompson, J.F., and Weatherill, N.P., “Aspects of Numerical Grid Generation: Current Science and Art,” AIAA–93_3539–CP, *Applied Aerodynamics Conference,* Monterey, CA, August 1993.

28. Thompson, J.F., Z.U.A. Warsi and C.W. Mastin (1985) *Numerous Grid Generation: Foundations and Applications* (North–Holland, Amsterdam).

29. Thompson, J.F., (1985), A survey of dynamically–adaptive grids in the numerical solution of partial differential equations, *Appl. Num. Math. 1,* 3–27.

30. Thompson, J.F., F.C. Thames and C.W. Mastin (1974) Automatic numerical generation of body–fitted curvilinear coordinate system for fields containing any number of arbitrary two–dimensional bodies. *J. Comp. Phys. 15*, pp. 299–319.

31. Thornburg, H.J. and Soni, B.K., "Weight Functions inGrid Adaption," Proceedings of the 4th International Conference in Numerical Grid Generation in Computational Fluid Dynamics and Related Fields held at Swansea, Wales 6–8th April 1994.

32. Thornburg, H.J. (1991) An adaptive–grid technique for simulation of complex unsteady flows, *Ph.D. Thesis*, Dept. of Mechanical, Industrial and Nuclear Engineering, University of Cincinnati, Cincinnati, Ohio.

33. Trompert, R.A. and J.G. Verwer (1990), A static–regridding method for two–dimensional parabolic partial differential equations, *Report NM–R8923*, Centre for Mathematics and Computer Science, Amsterdam, The Netherlands.

34. Tu, Y. and Thompson, J.F., "Three–Dimensional Adaptive Grid Generation on Composite Configurations," AIAA *Journal*, Vol. 29, p. 2025, 1991.

35. Vatsa, V.N., Sanetrik, M.D., and Parlette, E.B., "Development of a Flexible and Efficient Multigrid Based Flow Solver," AIAA–93–0677, Reno, NV Jan. 1993.

36. Yang, J.C., and Soni, B.K., "Structured Adaptive Grid Generation," Proceedings of the Mississippi State University Annual Conference on Differential Equations and Computational Simulation, MSU, March 19–20, 1993.

37. Yu, Tzu–Yi and Soni, Bharat K., "Geometry Transformer and NURBS in grid generation", The Fourth International Conference in Numerical Grid Generation and related fields, Swansea, England, April 6–8, 1994.

38. Yu, T.Y., "IGES Transformer and NURBS In Grid Generation," Master's Thesis, Mississippi State University, August.

APPENDIX A.1
Technical Paper AIAA–97–0637

AIAA 97-0637

The Application of CFD to the Prediction of Missile Body Vortices

Walter B. Sturek , U. S. Army Research Laboratory, Aberdeen Proving Ground, MD
Trevor Birch, Defense Research Agency, Bedford, UK
Marc Lauzon, Defense Research Establishment-Valcartier, Valcartier, CA
Clinton Housh, U. S. Naval Air Warfare Center, China Lake, CA
Joseph Manter, U. S. Air Force Wright Laboratory, Wright-Patterson AFB, OH
Eswar Josyula, U. S. Air Force Wright Laboratory, Wright-Patterson AFB, OH
Bharat Soni, Mississippi State University, Starkville, MS

35th Aerospace Sciences Meeting & Exhibit

January 6-10, 1997 / Reno, NV

THE APPLICATION OF CFD TO THE PREDICTION OF MISSILE BODY VORTICES

Walter B. Sturek*, U. S. Army Research Laboratory, Aberdeen Proving Ground, MD
Trevor Birch, Defense Research Agency, Bedford, UK
Marc Lauzon, Defense Research Establishment-Valcartier, Valcartier, CA
Clinton Housh, U. S. Naval Air Warfare Center, China Lake, CA
Joseph Manter**, U. S. Air Force Wright Laboratory, Wright-Patterson AFB, OH
Eswar Josyula**, U. S. Air Force Wright Laboratory, Wright-Patterson AFB, OH
Bharat Soni*, Mississippi State University, Starkville, MS

Abstract

This paper reports the results of a collaborative study carried out under the auspices of The Technical Cooperation Program (TTCP) with participants from Canada, UK, and the US. The purpose of this study was to apply Navier-Stokes computational techniques to a complex flow field with highly separated flow for a missile shape to evaluate the predictive technology. Nine Navier-Stokes computational codes were applied to predict the flow about an ogive-cylinder configuration for transonic and supersonic velocities at 8° and 14° angle of attack. The computational results were compared to experimental measurements for surface pressure, pitot surveys of the outer flow field, and strain gage force measurements. Computational results were obtained for nine turbulence models, laminar flow, and inviscid flow. For the conditions of this study, no 'best' turbulence model could be identified in the comparisons to experiment. Predictions of surface pressure and outer vortical flow in regions of highly separated flow indicate further development of the predictive technology is required; however, the prediction of aerodynamic lift and pitching moment are within acceptable design requirements.

Introduction

Computational Fluid Dynamics (CFD) has emerged as a critical technology for the design and assessment of weapon systems in the future. Such influencing factors as: advancing computer technology; funding shortfalls that limit the availability of experimental testing in the design phase of weapon systems development; and advances in computational modeling technology have served to focus emphasis on the development and validation of computational predictive technology. A previous TTCP study, which was completed in 1990, addressed a wide selection of test cases including base flows, bodies of revolution, and finned missiles. Transonic and supersonic velocities for angles of attack from small to large were included in the test matrix. The computational results were dominated by Euler solutions. One result of this effort was the identification of the inability of Euler solutions to provide adequate accuracy for flows with significant boundary layer separation, which results in vortex dominated flow. Another result was the realization of the magnitude of effort and computer resources required to perform Navier-Stokes modeling.

Since the completion of this previous study, significant advances in computational modeling techniques and increased availability of supercomputer resources have taken place. Accordingly, this study was chartered to focus effort to apply 3-D Navier-Stokes computational techniques to predict the flow fields about long l/d bodies at moderate angles of attack for transonic and supersonic velocities. The Defense Research Agency, UK provided a high-quality experimental data base (1)for a missile shape that included surface pressure, flow field pitot pressure surveys, and force measurements. The computational results have been compared to these experimental data along with cross comparisons among the various computational techniques.

---

* Associate Fellow, AIAA
** Senior Member, AIAA

Computational Techniques

The participants utilized Navier-Stokes computational codes that are used in the performance of missile aerodynamic analysis duties. The codes used cover a wide spectrum of predictive technology, including finite-difference, finite-volume, finite-element, explicit, implicit, upwind, and central-difference formulations. These codes have been reported elsewhere in the literature (2-8) in detail so no extensive code descriptions will be included in this report. Table 1 gives a listing of the codes used in this study.

Experimental Data

The experimental data were provided by the DRA, Bedford, UK. The data were obtained as part of a comprehensive experimental study that extended over a period of several years, Birch (1). The model configuration of interest for this study is a 3-caliber ogive with a 10-caliber cylindrical afterbody. A Schlieren photograph showing the model mounted in the wind tunnel for test conditions of Mach = 3.5 and alpha = 8° is shown in Figure 1. The test conditions for the six test cases used in this study are listed in Table 2. The experimental data obtained include surface pressures, pitot surveys of the flow field, and force balance measurements. The surface pressure measurements include 32 axial stations for 41 circumferential locations from the wind- to the lee-side at a 4.5° increment. The pitot pressure surveys provide a dense array of measurements at axial stations as indicated in Table 3. Strain gage force balance measurements are available as indicated.

Results

Test Case Overview

Each test case presents significant physical modeling challenges. The following discussion attempts to provide an overview of the flow fields along with a "typical" comparison between computation and experiment. Due to the large number of computational results, space limitations prevent showing a comprehensive comparison between the computational techniques. The calculations shown were performed using the overflow code. The turbulent viscous results were obtained using the BLDS turbulence model.

Case 1. Mach = 1.45, $\alpha = 14°$, $Re/d = 0.667 \times 10^6$, Figure 2.
The laminar results indicate strong separation on the wind-side prior to x/d = 3.5, whereas the turbulent results and experiment indicate separation on the lee-side for $3.5<x/d<4.5$. The lee-side is strongly separated for $x/d>4.5$. The results at x/d=6.5,7.5 and 9.5 show the experimental pressure greater than the prediction on the wind-side where close agreement between computation and experiment is expected. This behavior is, perhaps, evidence that a wind-side shock is triggered from a position upstream of x/d=6.5 and results in a pressure jump that the computed results do not show. An explanation for the computation not predicting this behavior is unknown. It is noted that the laminar predictions also do not predict the increase in surface pressure on the wind-side for $x/d>5.5$ even though the laminar predictions indicate early boundary-layer separation that could trigger a wind-side shock.

Case 2. Mach = 1.8, $\alpha = 14°$, $Re/d = 0.667 \times 10^6$, Figure 3.
The laminar results indicate strong separation for x/d=3.5, which is not supported by the experimental data or the turbulent calculations. The laminar viscous results consistently predict early flow field separation compared to the experiment and turbulent viscous results. The experiment indicates the flow is strongly separated for $x/d > 4.5$. A pressure jump is noted at x/d = 9.5 similar to that noted for Case 1.

Case 3. Mach = 2.5, $\alpha = 14°$, $Re/d = 1.123 \times 10^6$, Figure 4.
The laminar viscous results indicate early separation of the viscous layer compared to the experiment and the turbulent viscous results. Good agreement is achieved on the wind-side for all results shown. This test case was selected as the top priority because the Mach number and Reynolds number of the flow provided the expectation for high-quality experimental measurements and fully turbulent viscous flow, which would yield the best conditions for agreement between computation and experiment.

Case 4. Mach = 3.5, $\alpha = 8°$, $Re/d = 1.123 \times 10^6$, Figure 5.
The laminar viscous results indicate separation for x/d = 4.5 and greater. Good agreement is shown on the wind-side for all stations except at x/d = 2.4, where the calculations predict a higher pressure than

the experiment. No indication of a pressure jump resulting from an upstream shock is apparent as was seen in the lower Mach number flows. The turbulent viscous predictions for x/d >7.5 predict a lower first suction peak than indicated by the experimental data.

Case 5. Mach = 3.5, $\alpha = 14\,°$, Re/d = 1.123×10^6, Figure 6.
The laminar and turbulent viscous results are close agreement over the full missile body. The separated flow region on the lee-side is characterized by a relatively flat pressure distribution compared to the other test cases. For x/d > 5.5, the turbulent results indicate earlier separation than the laminar results with the experiment located in between.

Case 6. Mach = 0.7, $\alpha = 14\,°$, Re/d = 0.667×10^6, Figure 7.
This subsonic test case was added during the second year of the study as a special challenge. Computational modeling required moving the outer boundary further away from the body in order to lessen effects of the outer boundary interacting with the flow on the body. This reduced the density of the grid resolution and was cause for some concern. The turbulent viscous predictions are obviously in better agreement with the experiment than laminar. The lee-side suction peak is not predicted well until x/d > 7.5 is reached. Also, the turbulent results indicate some jitter in the surface pressure profiles, particularly on the wind-side for x/d > 3.5.

In summary, the test case results indicate that turbulent viscous modeling is required and that the flow fields are highly separated on the lee-side. There is some indication that a wind-side shock occurs resulting in a pressure jump on the wind-side at downstream stations for test cases with free stream Mach Number < 2.0 that is not predicted by the computations.

Grid Resolution

The question of grid resolution was addressed in this study by making comparisons for several grid resolutions. Since the time-marching codes require substantial computer resources for modest grid resolution, this effect has been addressed by comparing results for time-marching codes using a variety of grid resolutions and also by comparing the results from time-marching codes with much higher resolution results obtained with an iterative PNS code. An example comparing results for different grid resolutions using the time-marching code CFL3D is shown in Figure 8. Only slight differences are seen for the grid resolutions shown (61 x 81 x 141 and 81 x 111 x 141)(axial, normal, circumferential). Grid resolutions for the time-marching codes compared in the study ranged from 61 to 150 (axial), 81 to 111(normal), and 81 to 141(circumferential).

The iterative PNS technique provides the capability to achieve highly dense grid resolution for the conditions of this study with moderate computer resources. An example of the results achieved using this technique for a grid resolution of 1000 x 72 x 72 is shown in Figure 9. The turbulent viscous result is comparable to that shown in Figure 8. These results lend confidence that a nominal grid resolution of 80 x 80 x 80 is adequate for the test cases considered here. Figure 9 also shows results for laminar and inviscid modeling. The inviscid result predicts a lee-side shock that is not confirmed by the experimental measurements.

Turbulence Models

A variety of turbulence models have been utilized for the comparisons with experimental data. The listing includes: Baldwin-Lomax(BL); Baldwin-Lomax-Degani-Schiff(BLDS); k-epsilon(ke), k-omega(kw), Spalart-Allmaras(SA); Smagorinsky(SM); and Baldwin-Barth(BB). An example of comparisons for Case 3 using the NPARC code for four turbulence models is shown in Figure 10. The BB model appears to provide the best results for the first suction peak. The BL model, where the turbulent length scale is determined by a search to the flow field outer boundary, consistently overpredicts the location of the first suction peak. None of the models predict well the separated flow region for x/d = 6.5 and 7.5, where there is a distinct second suction peak. For x/d = 9.5 and 11.5, the models provide equivalent results in the lee-side separated flow. These results are consistent with those for all the computational codes utilized. The message indicated here is that the more computer-intensive two-equation turbulence models do not provide a clear advantage over the less sophisticated algebraic or one-equation turbulence models.

Statistical Analysis

The scope of the computational study includes eight computer codes, nine turbulent viscous models, laminar viscous results, several grid resolutions, and six test cases. This has resulted in more than 90 test case results for evaluation with respect to each other and with respect to effects of grid resolution, turbulence model, and computational technique.

The traditional method for evaluating the previously mentioned effects on flow field computations has been for the engineer to visually inspect the results, make qualitative comparisons, and draw conclusions. This process can be very satisfactory for limited data sets to evaluate. However, for this study, the number of data sets has grown to a large number, thus making the evaluation and comparison of the results a formidable task.

Thus, it was decided to explore the possibility that statistical analysis techniques could assist in the evaluation process. The technique used here is to consider the difference between the computation and experiment. This difference has been used to obtain a mean value, standard deviation, and variance between the experiment and computation. An example of the results of this analysis technique for Case 3 in which the statistical quantities have been summed for 41 circumferential positions at 9 axial stations for each computational result is shown in Figure 11. A visualization of the analysis is shown in Figures 11 and 12 in the form of a box and whisker plot. The summary shown consists of the median of the errors, the inner-quartiles (the 25th and 75th percentiles) that determine the vertical dimension of the box, and the maximum and minimum error to determine the whisker lengths. These results indicate that, although individual comparisons for different codes, grid resolutions, and viscosity models show varying amounts of disagreement, the overall quality of the comparisons with experiment is comparable.

The above analysis technique has been applied to all data sets from the study. The results shown in Figures 11 and 12 provide an overview of the comparisons obtained for the various codes and permit some general conclusions to be made.

All turbulent viscous results for test case 3 are shown in Figure 11. This provides a good summary comparison for the different computational techniques and turbulence models. Table 4 provides a listing of the CFD code associated with the ID number shown in Figure 11. The results indicate relative consistency. Results number 1, 4, and 13 appear to have the best agreement, whereas results number 2, 8, 10, 12, and 16 appear to have the larger errors. Of these results, case 4 and 13 were obtained using the BLDS turbulence model and case 2, 12, 16 were obtained using the BL turbulence model without modification. These results suggest that the BL turbulence model has potential for good performance; however, it requires a skilled computational specialist to use effectively. Another observation is that the benefit of using more complex two-equation turbulence models does not justify the increased computational effort as opposed to algebraic or single equation turbulence models.

A sample statistical analysis result is shown in Figure 12, which shows results achieved using the FDL3DI code for test cases 1, 2, 3, 4 and 5. This plot provides insight into the relative accuracy for the predictions for the various flow field conditions. One obvious observation is that the results for test cases 1, 2, and 3 (Mach < 3) indicate significantly greater errors than those for test cases 4 and 5 (Mach $=3.5$).

This technique shows promise for providing a useful tool for use by the engineer when comparing numerous computational and experimental results; however, it does not diminish the value of examination of individual profile comparisons.

Vortical Flow

The experimental data included measurements of pitot pressures in the outer flow fields using total head probes. These data provide the opportunity to evaluate the ability to predict the size, strength, and location of these vortices. These comparisons are made by direct comparisons of pitot pressures calculated from the flow field computational data to the experimental measurements. Additionally, in an effort to obtain a more quantitative measurement of the ability of the computational technique to predict the strength and location of the vortex, the location of the center of the vortex and the pitot pressure along a line extending from the vortex center to the pitch-plane axis were obtained from the experiment.

Examples of comparisons between the computations and experiment for the pitot pressure surveys are shown in Figures 13, 14, 15, and 16 for M= 1.8, 2.5, 3.5, and 0.7, respectively for $x/d = 11.5$. These figures show examples of pitot contours and the pitot pressure extrapolation along a line perpendicular to the pitch plane passing through the vortex core as defined by the experimental measurement. Comparisons are shown for laminar and turbulent viscous modeling obtained using the NPARC code and the BLDS turbulence model. The results indicate that the laminar viscous predictions consistently underpredict the strength and size of the vortex core. Also, the turbulent modeling provides encouraging accuracy for the axial position shown.

The NPARC implementation of the BLDS turbulence model provides an option to limit the search range in the radial direction for determining the turbulent length scale. An example of the effect of this limiter on the prediction of the outer vortical flow is shown in Figure 17. The case shown is for M=2.5, $\alpha=14°$. Results for a search limit of 15 and 25 points are shown (ke = 15 and ke=25). The extent of the region of this search in the flowfield is indicated by the circles drawn about the model cross section. A detailed comparison, not shown, in the study was carried out to examine this effect on the predictions. It was determined that for the test cases considered here, a value of 15 provided optimal results.

Aerodynamic Forces and Moments

The experimental data available included strain gage balance measurements for normal force, pitching moment, and axial force. A partial tabulation of results obtained for normal force and pitching moment are provided in Table 5. These results indicate that most codes provided comparable predictions that are within ± 3% agreement with experiment for normal force and ± 5% for pitching moment. This degree of accuracy is within acceptable requirements for initial design and optimization analysis for most projectile and missile systems.

Closing Remarks

1) Consistent results were achieved for the various computational codes for like conditions of grid density and turbulence model.

2) For the conditions of this study, no best turbulence model could be identified in the comparisons to experiment. There was no consistent benefit obtained from utilization of a (k-epsilon or k-omega) turbulence model over the algebraic models even though substantial flow separation was present in the flow fields studied.

3) Although flow field details such as the definition of the separated vortex and the surface pressure in regions of separated flow are not predicted as well as desired, the aerodynamic force and moment predictions are accurate within ± 5% for these test cases. This level of accuracy is usually adequate for weapon design requirements. Thus, CFD is a viable predictive tool for the class of body configurations considered in this study and should be of increasing importance as computer technology continues to advance thus permitting the predicted results to be obtained in a timely fashion.

Acknowledgments

The authors would like to express their appreciation of TTCP Technical Panel WTP-2 for chartering this study. Also, significant contributions to the body of computational results of this study have been made by Hugh Thornburg (formerly at Mississippi State University NSF Engineering Research Center); Duane Frist (formerly at the U. S. Army Research Laboratory); Don Kinsey (U. S. Air Force Wright Laboratory); J. Sahu, Karen Heavey, and Malcolm Taylor (U. S. Army Research Laboratory); Stephen Ray (Army High Performance Computing Research Center); and Roy Koomullil (Mississippi State University, NSF Engineering Research Center).

Nomenclature

d	model cylinder diameter, 3.7-inches
C_m	pitching moment coefficient
C_n	Normal force coefficient
M	Mach Number
x	axial distance from nose of missile
y	vertical distance from axis
z	horizontal distance from axis
α	angle of attack, degrees
phi	circumferential angle about axis

Turbulence Model Identification

BB	Baldwin-Barth
BBGR	Baldwin-Barth-Goldstein-Ramakrishnan
BL	Baldwin-Lomax
BLDS	Baldwin-Lomax with Degani-Schiff

ke	k-epsilon
kw	k-omega, Wilcox
SA	Spalart-Allmaras
SM	Smagorinski
kwm	k-omega, Menter

References

1. Birch, T., pivate communication.

2. Cooper, G. K. and Sirbaugh, J. R., "PARC Code: Theory and Usage", AEDC-TR-89-15, December 1989.

3. NPARC Alliance Technical Team, "A User's Guide to NPARC Version 2.0", November 1994.

4. Chakravarthy, S. R., *et. al.*, "Computing Aerodynamics Methodology for the Aerospace Plane," *Computing Systems in Engineering*, Vol. 1, Nos 2-4, pp. 415-435, 1990.

5. Visbal, M.R., "Onset of Vortex Breakdown Above a Pitching Delta Wing," *AIAA Journal*, 32(8), pp. 1568-1575, August 1995.

6. Sahu, J. and Steger, J.L., "Numerical Simulation of Transonic Flows," *International Journal for Numerical Methods in Fluids*, Vol. 10, No. 8, pp. 855-873, 1990.

7. Tezduyar, T., Behr, M., Aliabadi, S., Mittal, S., and Ray, S.E., "A new mixed preconditioning method for finite element computations," *Computer Methods in Applied Mechanics and Engineering*, Vol. 99, pp. 27-42, 1992.

8. Buning, P., et. al., "OVERFLOW User's Manuel," NASA-Ames Research Center, June 1995.

Table 1. List of Navier-Stokes Codes Utilized

Code Name	**Brief Description**
NPARC	**FD, Implicit, Central**
CFL3D	**FV, Implicit, ROE**
UNPNS	**FD, Implicit, Iterative PNS**
USA Series	**FV, Implicit, EOS**
FDL3DI	**FD, Implicit, Upwind-Central**
F3D	**FV, Implicit, Upwind-Central**
AHPCRC FE	**FE, Implicit, GMRES**
OVERFLOW	**FV, Implicit, Upwind-Central**
COBALT	**FV, Explicit, Godonov**

Table 2. Wind Tunnel Test Conditions

Case Number	**Mach Number**	**Angle of Attack**	**Reynolds No, x10^6/ft**
1	**1.45**	**14**	**2.0**
2	**1.8**	**14**	**2.0**
3	**2.5**	**14**	**4.0**
4	**3.5**	**8**	**4.0**
5	**3.5**	**14**	**2.0**
6	**0.7**	**14**	**2.0**

Table 3. Experimental Data Available

Case Number	Surface Pressure	Pitot Survey, X/D	Force Measurements
1	32 x 41	8.5, 11.5	no
2	32 x 41	5.5, 8.5, 11.5	no
3	32 x 41	5.5, 11.5	yes
4	32 x 41	5.5	yes
5	32 x 41	5.5, 11.5	yes
6	32 x 41	11.5	no

Table 4. Code ID for Figure 11 and Table 5.

ID Number	Code, Turbulence Model
1	AHPCRC FE, SM
2	UNPNS, BL
3	UNIS/USA, BBGR
4	OVERFLOW, BLDS
5	FDL3DI, ke
6	COBALT, SA
7	NPARC, BLDS
8	CFL3D, BB
9	CFL3D, BL
10	CFL3D, kw
11	CFL3D, SA
12	NPARC, BB
13	NPARC, BL
14	NPARC, ke
15	NPARC, kw
16	F3D, BL
17	USA, BB

Table 5. Normal Force and Pitching Moment - Prediction and Experiment

Test Case	Code ID	Normal Force	Exp. - C_n	%-C_n	Pitching Moment	Exp. - C_m	% - C_m
3	3	1.87	1.91	2.09	-10.05	-10.24	1.85
3	4	1.88	1.91	1.57	-10.16	-10.24	0.78
3	5	1.84	1.91	3.66	-10.31	-10.24	-0.68
3	6	1.91	1.91	0.0	-10.5	-10.24	-2.54
3	7	1.85	1.91	3.14	-9.92	-10.24	3.12
4	4	0.75	0.76	1.32	-3.59	-3.47	-3.48
4	7	0.76	0.76	0.0	-3.72	-3.47	-7.20
5	3	1.92	1.92	0.0	-11.17	-11.11	-0.54
5	4	1.92	1.92	0.0	-11.21	-11.11	-0.90
5	7	1.90	1.92	1.04	-11.00	-11.11	0.99

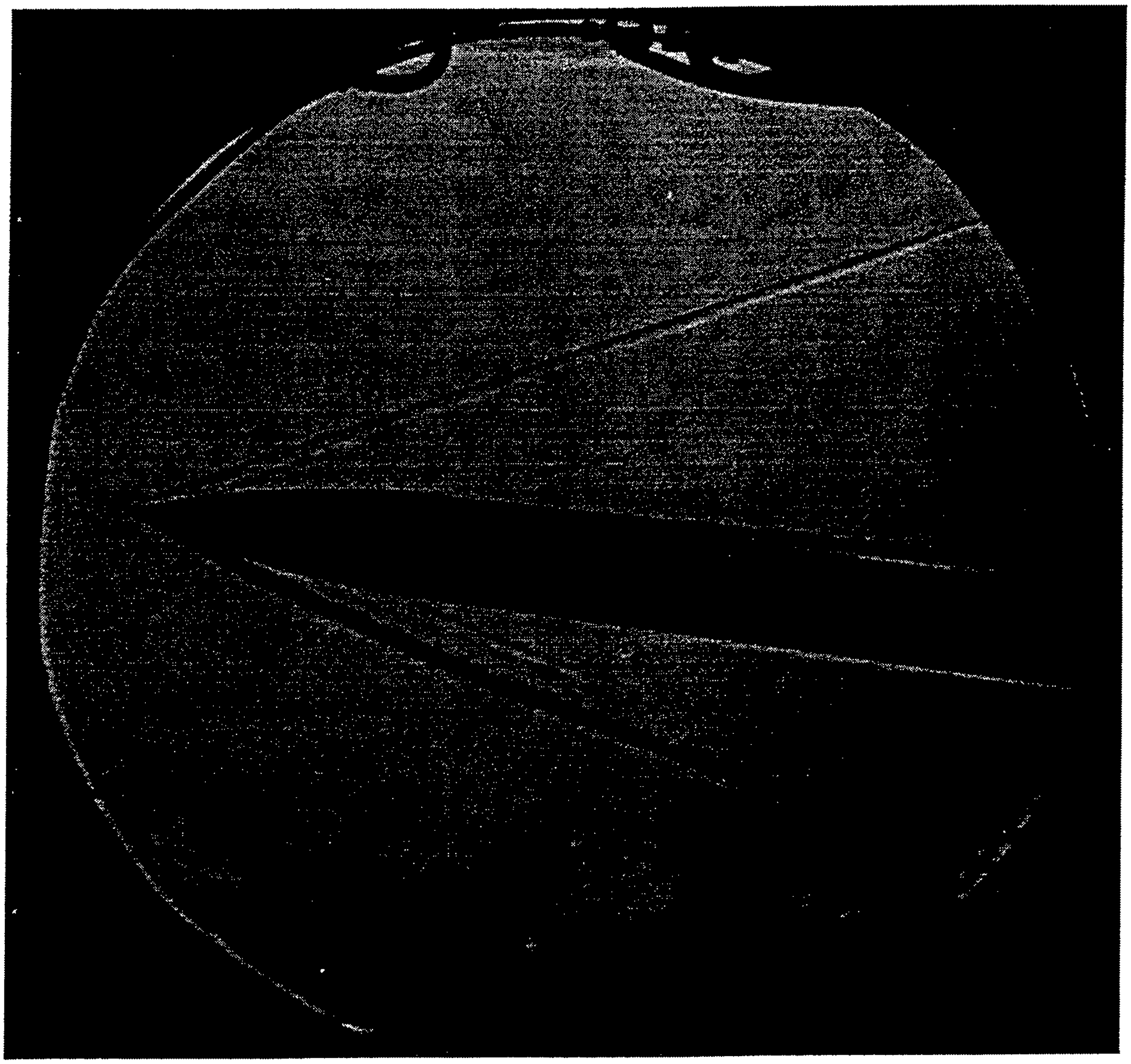

Figure1. Schlieren photograph of model mounted in wind tunnel, Mach =3.5, $\alpha = 8°$.

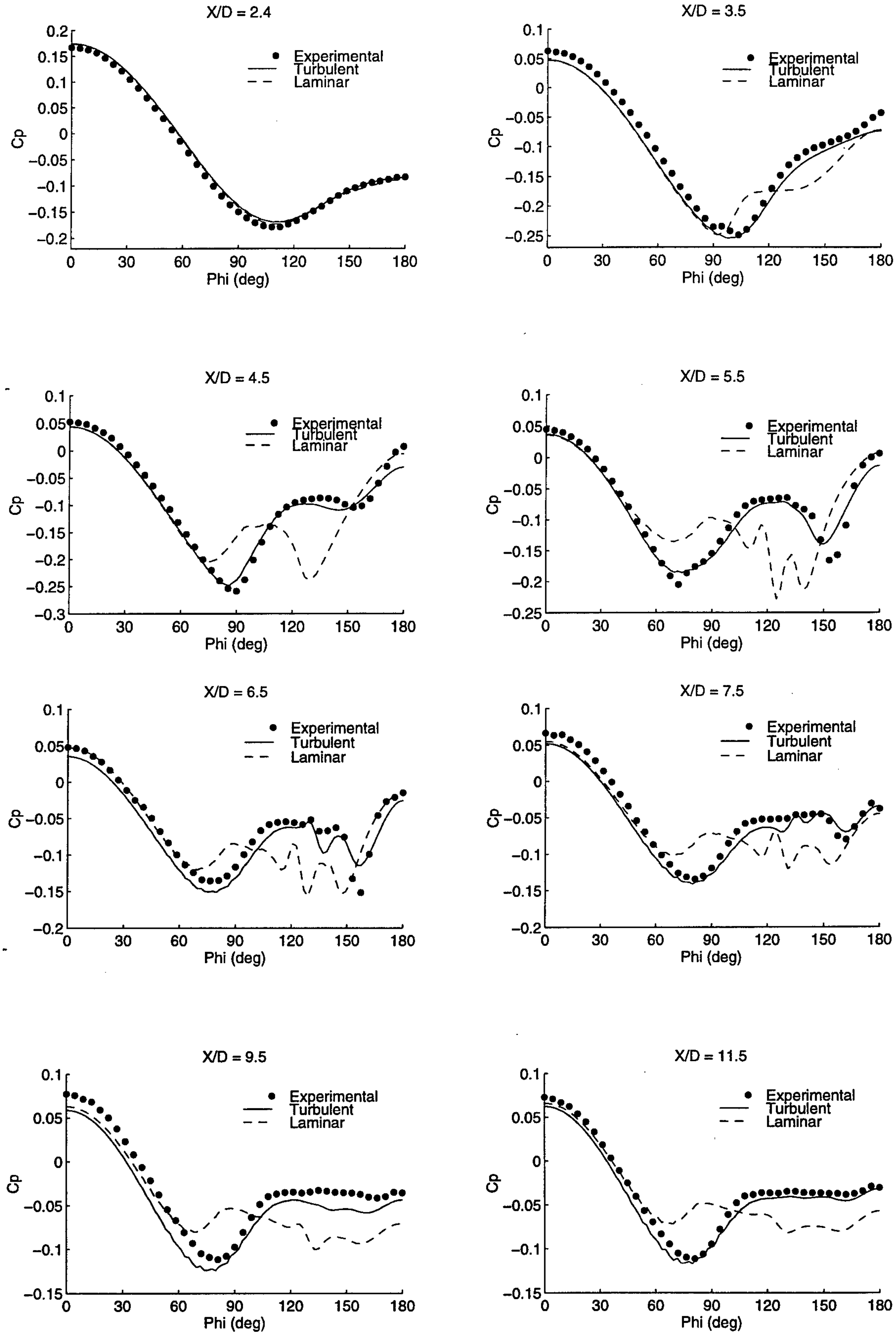

Figure 2. Test Case Overview, Case 1, Mach = 1.45, $\alpha = 14°$, Re/D = 0.667×10^6

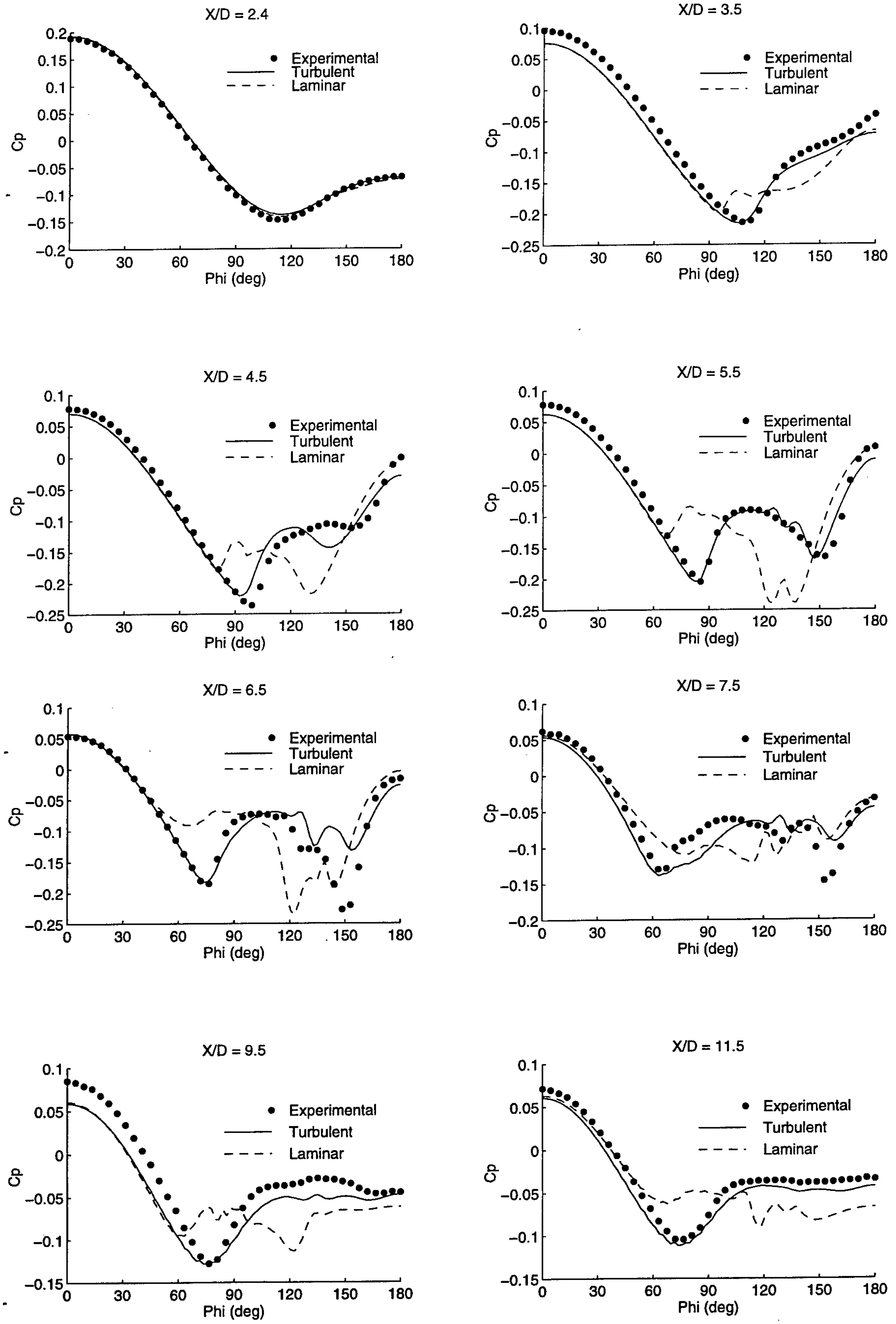

Figure 3. Test Case Overview, Case 2, Mach = 1.8, α = 14°, Re/D = 0.667x10^6

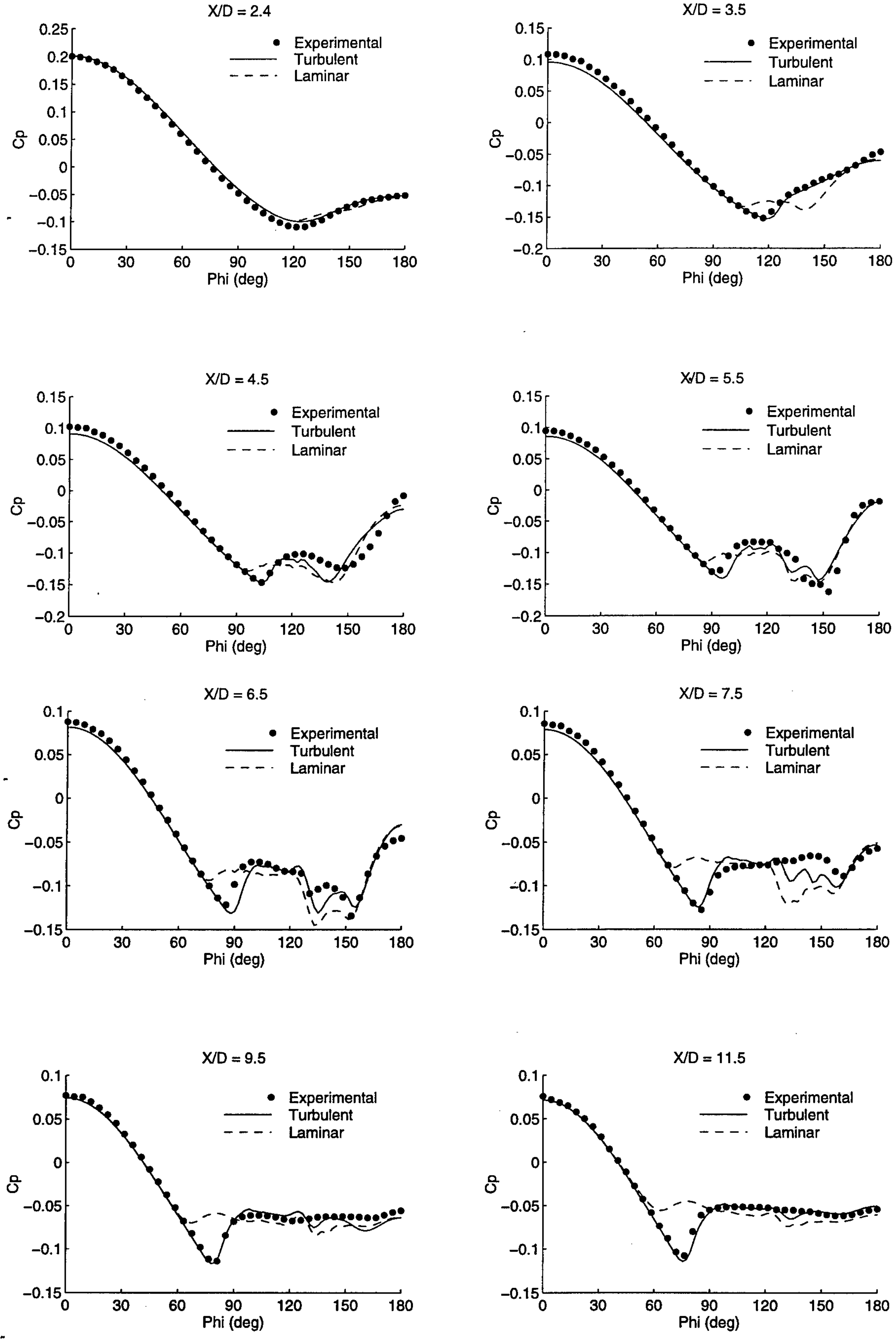

Figure 4. Test Case Overview, Case 3, Mach = 2.5, α = 14°., Re/D = 1.123x10^6

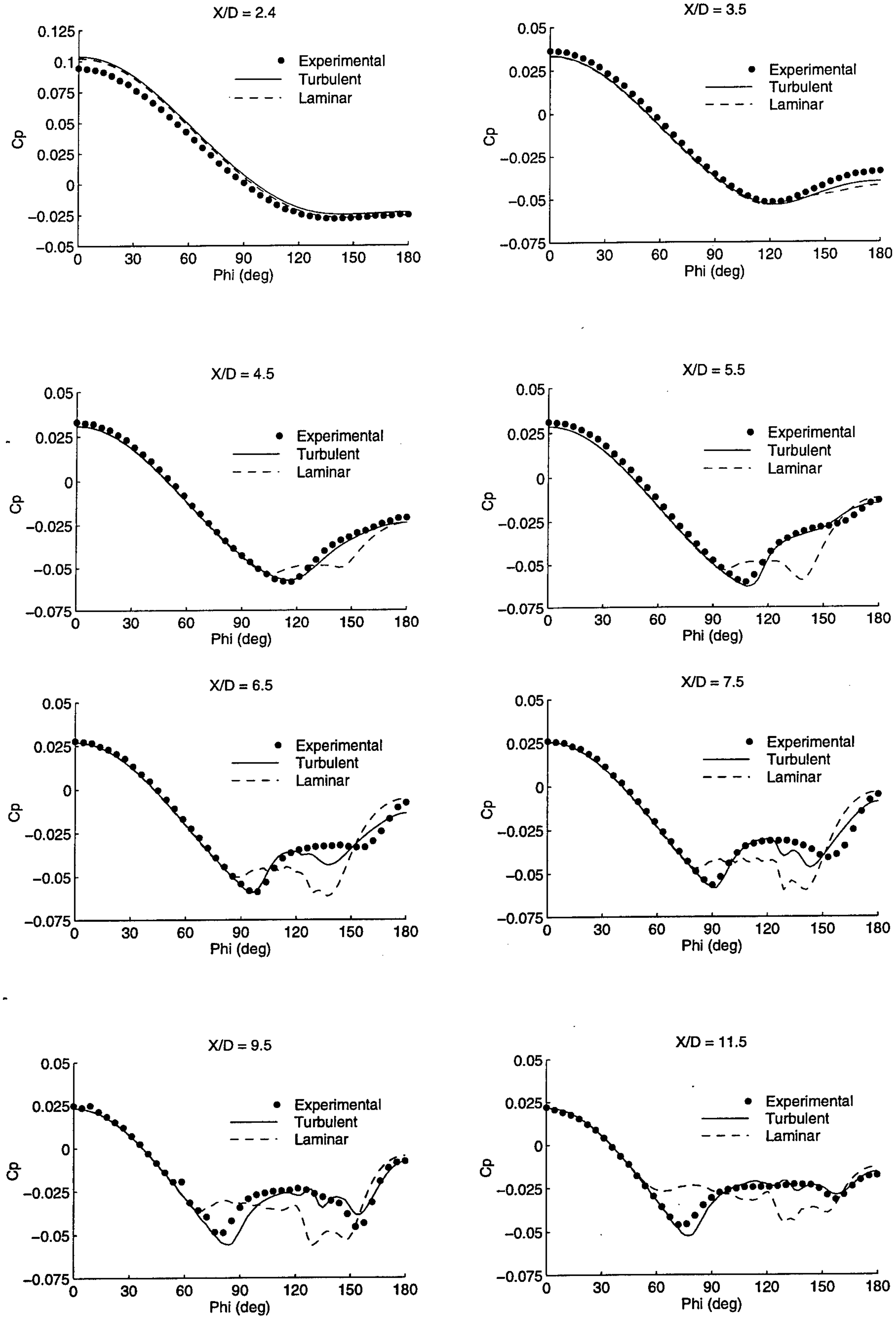

Figure 5. Test Case Overview, Case 4, Mach = 3.5, $\alpha = 8°$, Re/D = 1.123×10^6

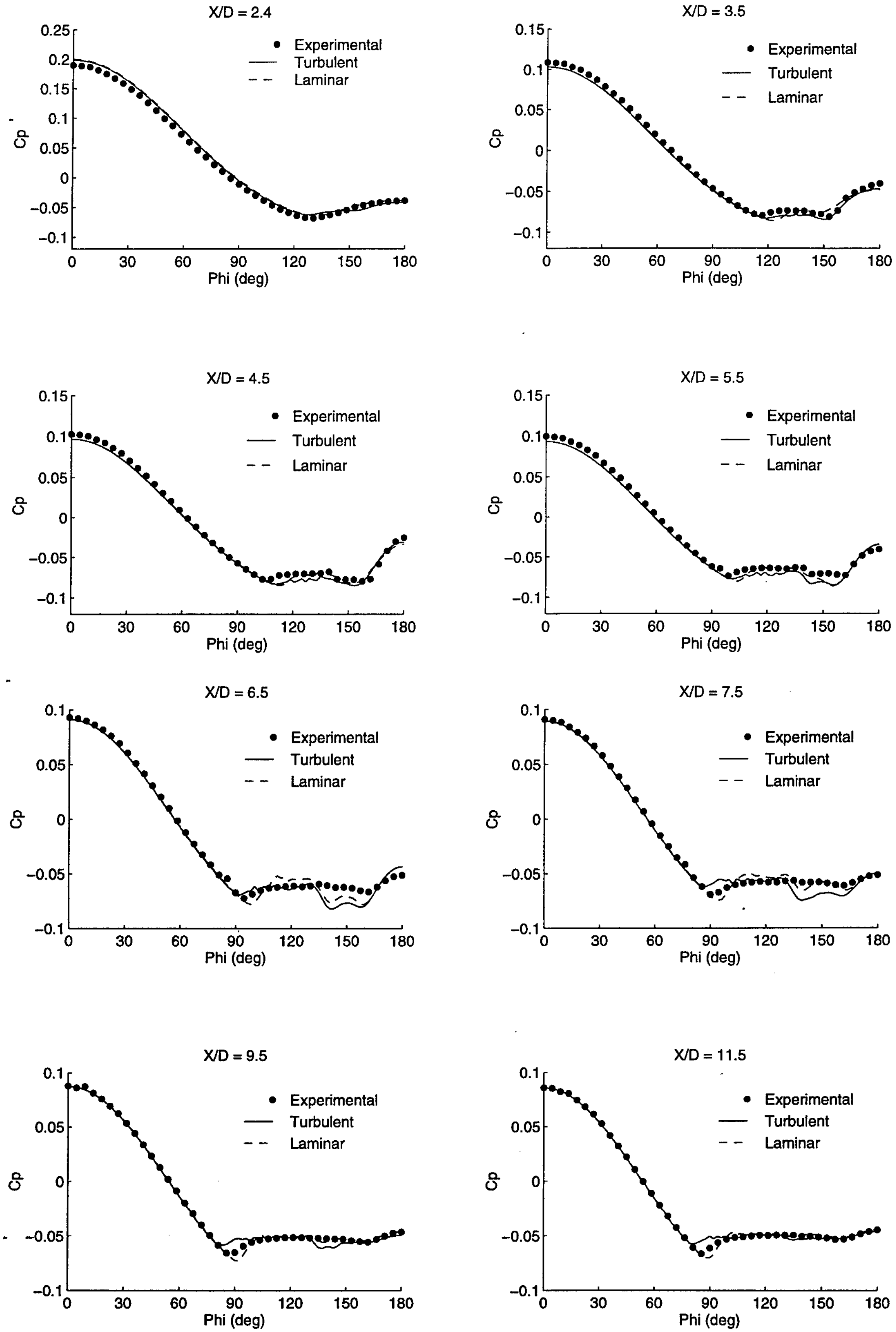

Figure 6. Test Case Overview, Case 5, Mach = 3.5, α = 14°, Re/D = 1.123×10^{6}

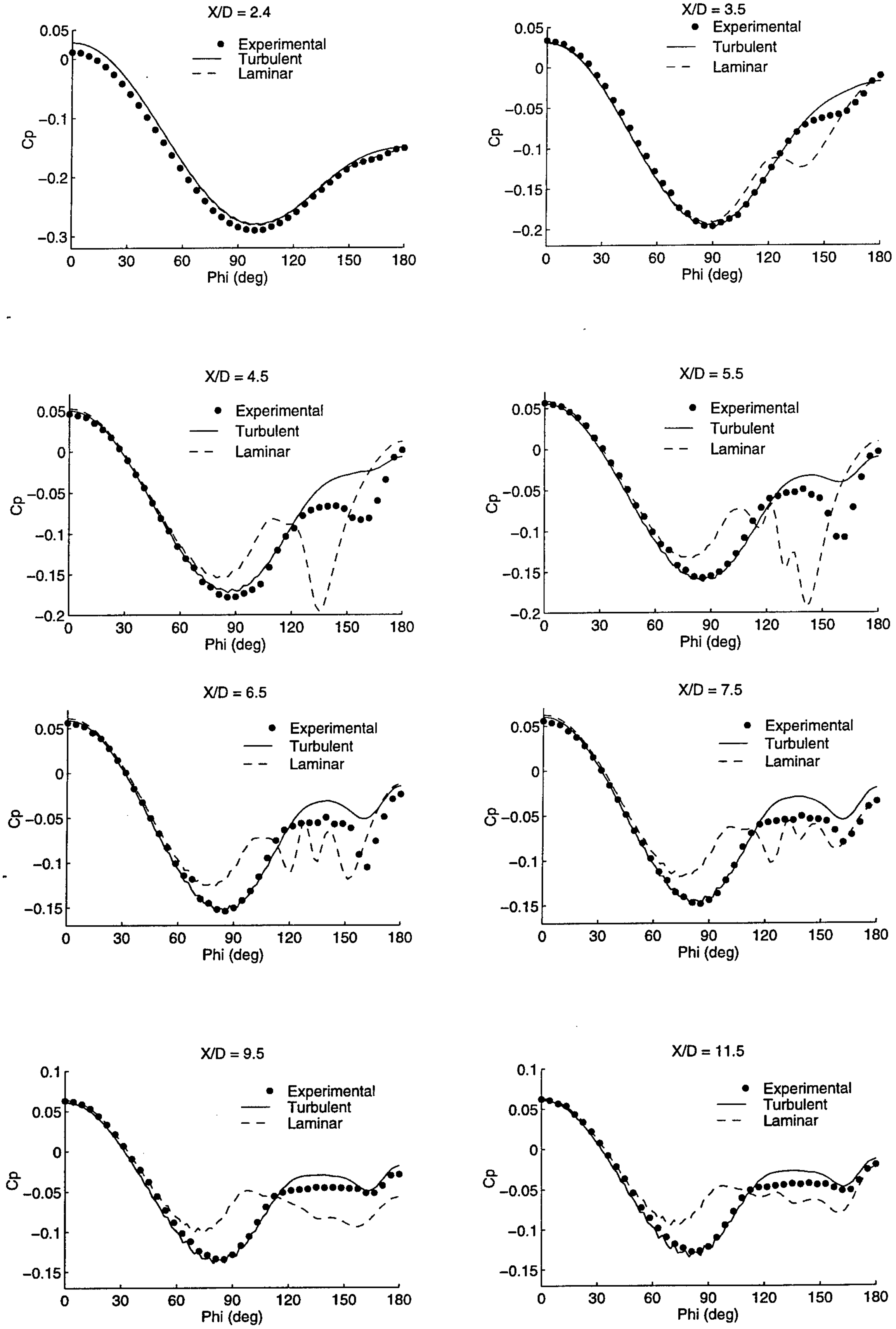

Figure 7. Test Case Overview, Case 6, Mach = 0.7, $\alpha = 14°$, Re/D = 0.667×10^6

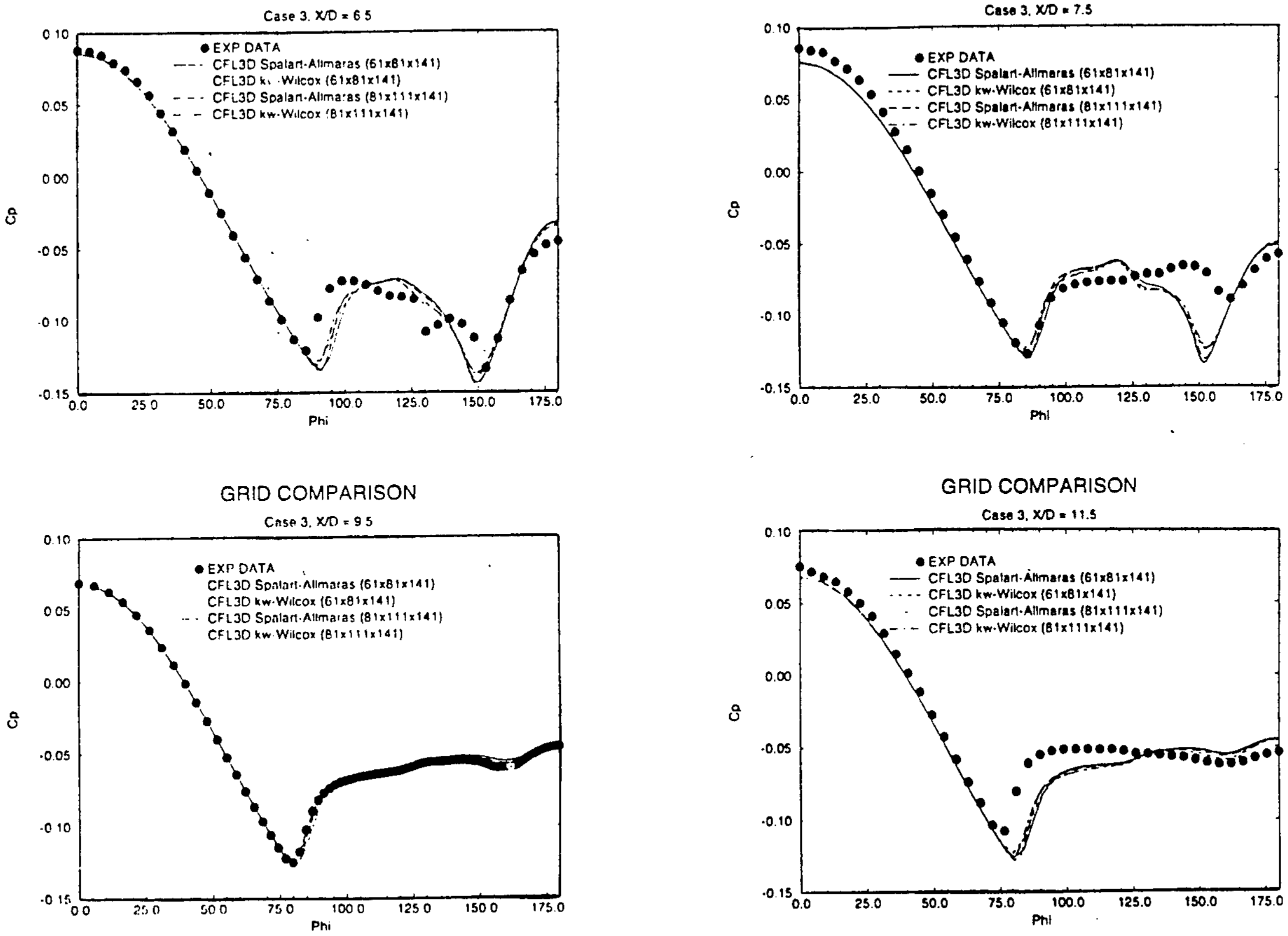

Figure 8. Grid resolution, CFL3D results

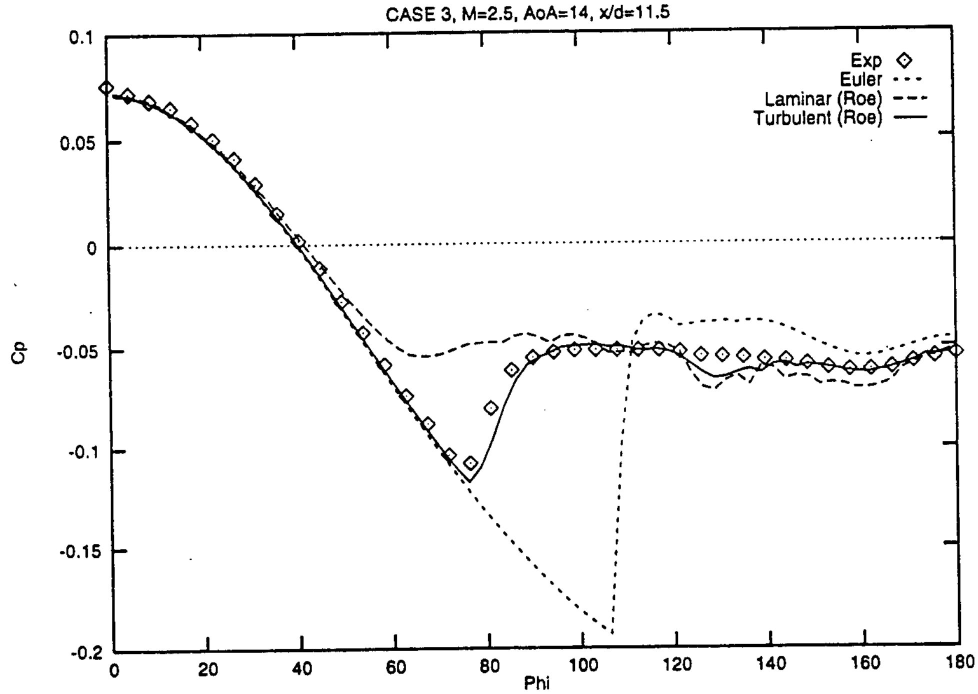

Figure 9. Grid resolution, iterative PNS, Case 3, Mach = 2.5, α = 14°, X/D = 11.5

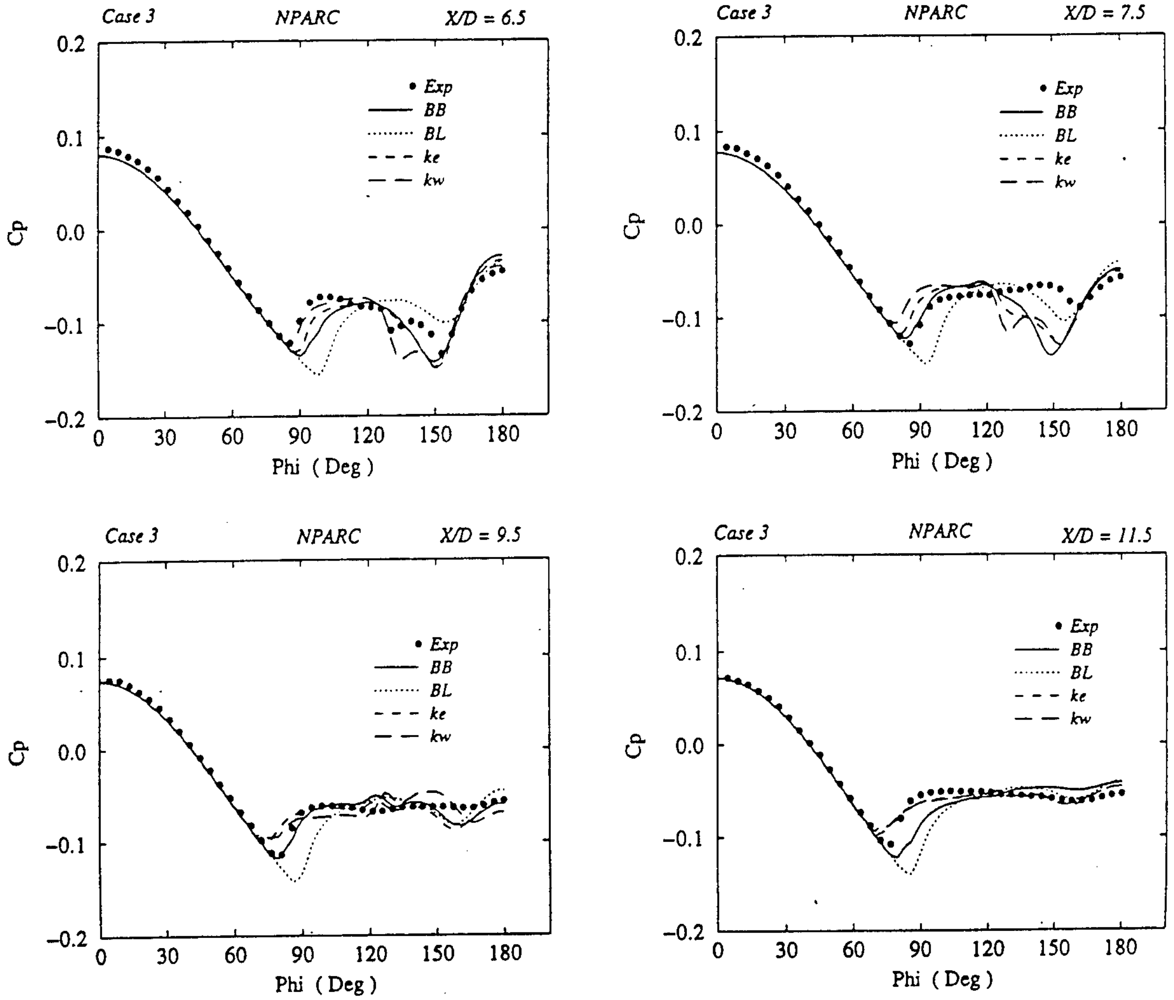

Figure 10. Turbulence Model Comparison, Case 3, M=2.5, α=14°

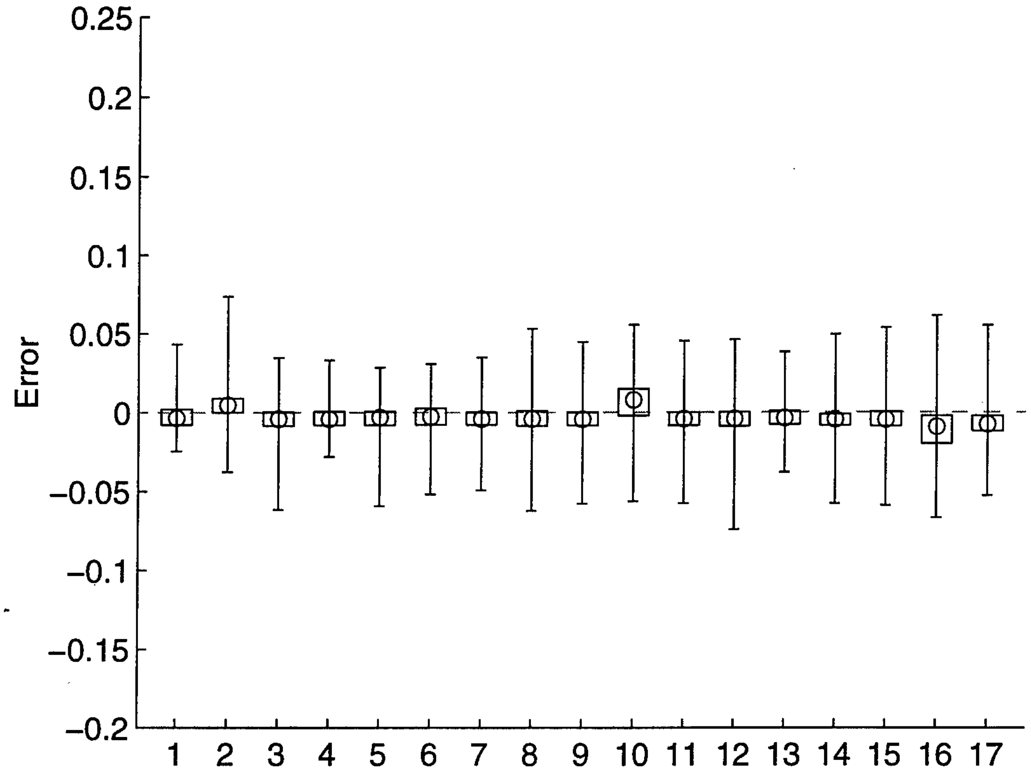

Figure 11. Statistical analysis box & whisker plot for Case 3, M=2.5, α=14° , all results (see Table 4 for code identification.

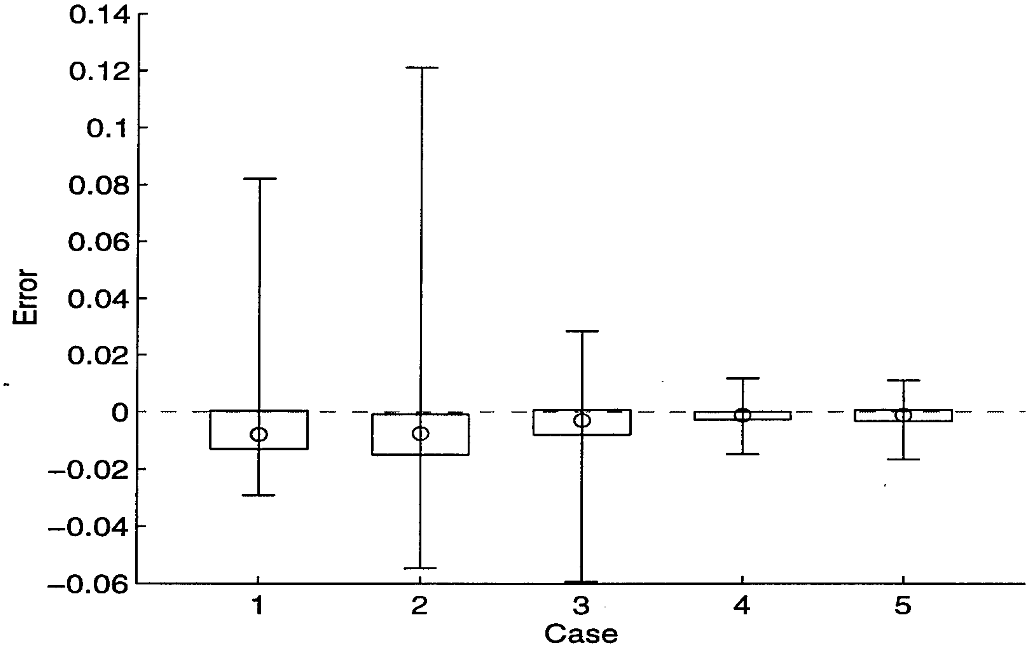

Figure 12. Statistical analysis box & whisker plot for test case numbers 1, 2, 3, 4, 5. Code ID 5.

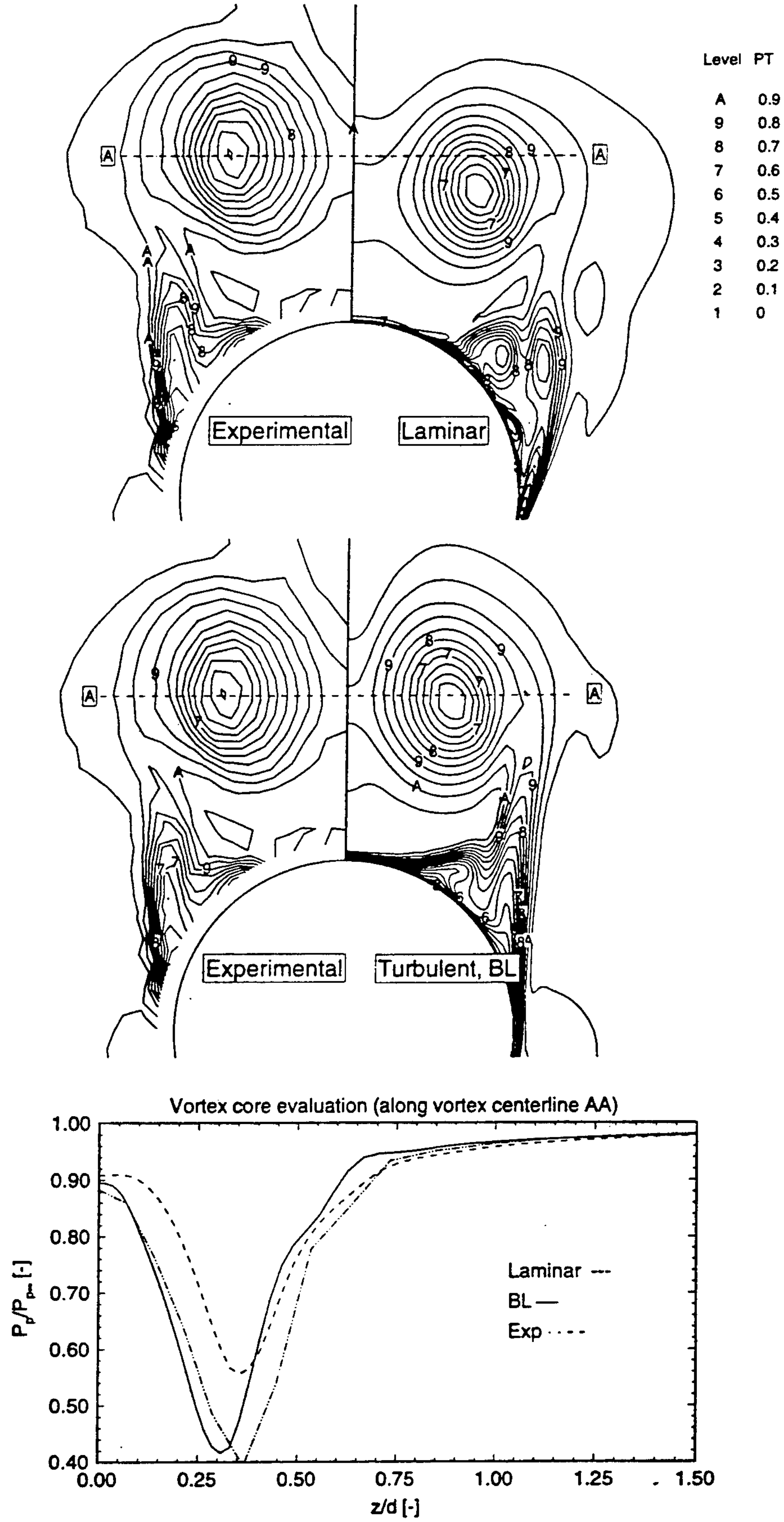

Figure 13. Pitot pressure contours for experiment compared to laminar and turbulent viscous computations. Vortex core pitot pressure along Z/D line to flow field centerline. Case 2, M=1.8, α=14°, X/D=11.5.

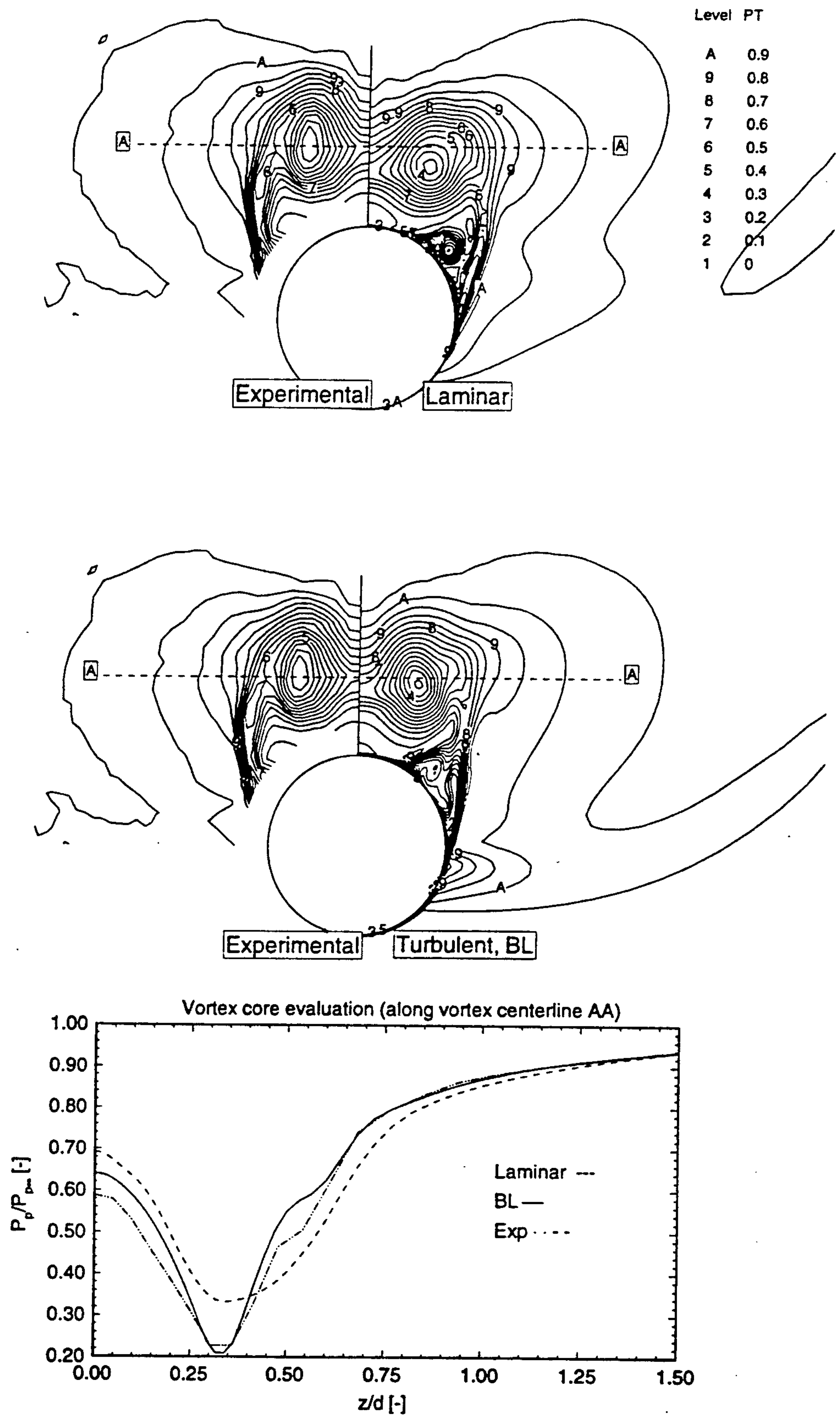

Figure 14. Pitot pressure contours for experiment compared to laminar and turbulent viscous computations. Vortex core pitot pressure along Z/D line to flow field centerline.
Case 3, M=2.5, α=14°, X/D =11.5.

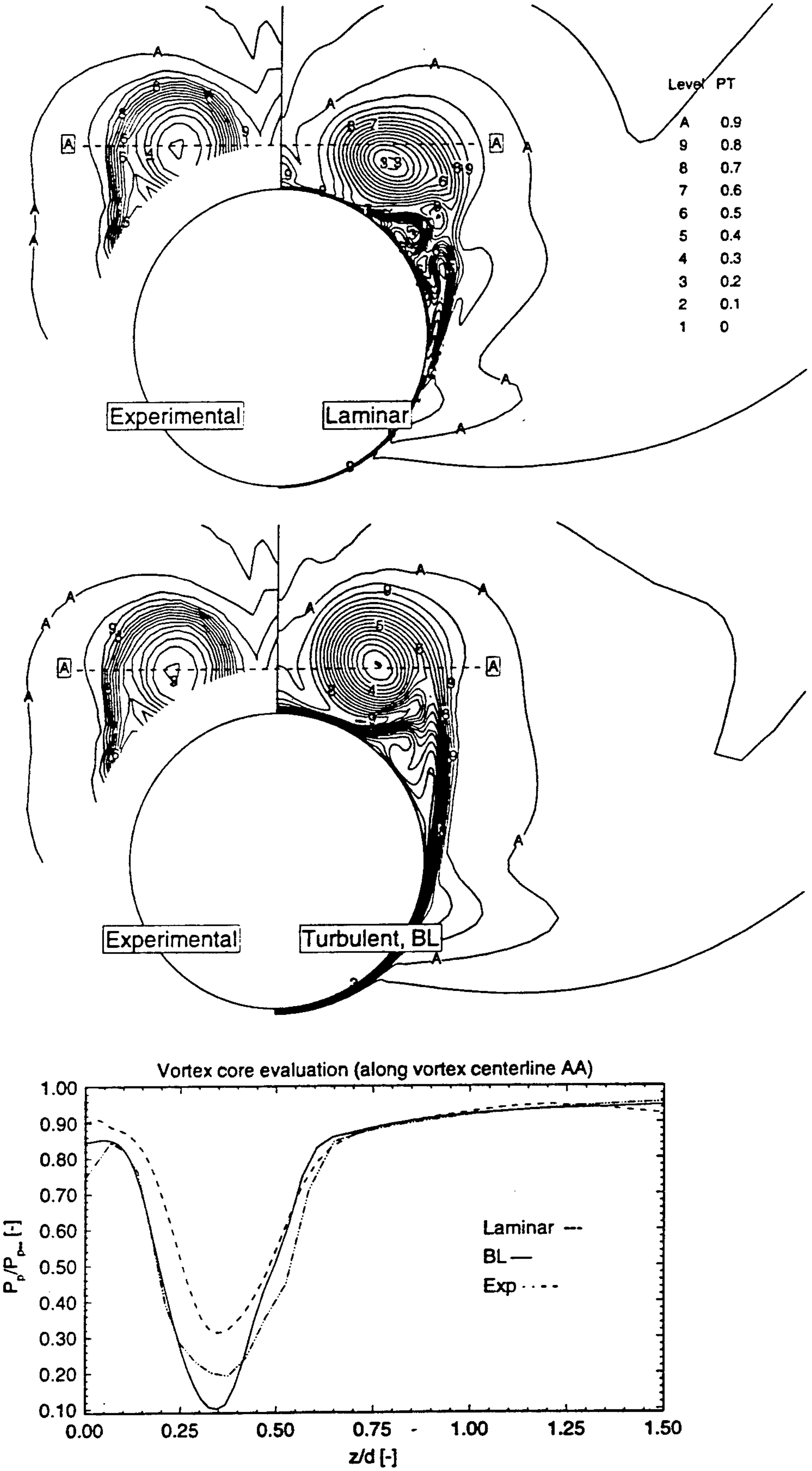

Figure 15. Pitot pressure contours for experiment compared to laminar and turbulent viscous computations. Vortex core pitot pressure along Z/D line to flow field centerline.
Case 4, M=3.5, α=8°, X/D =11.5.

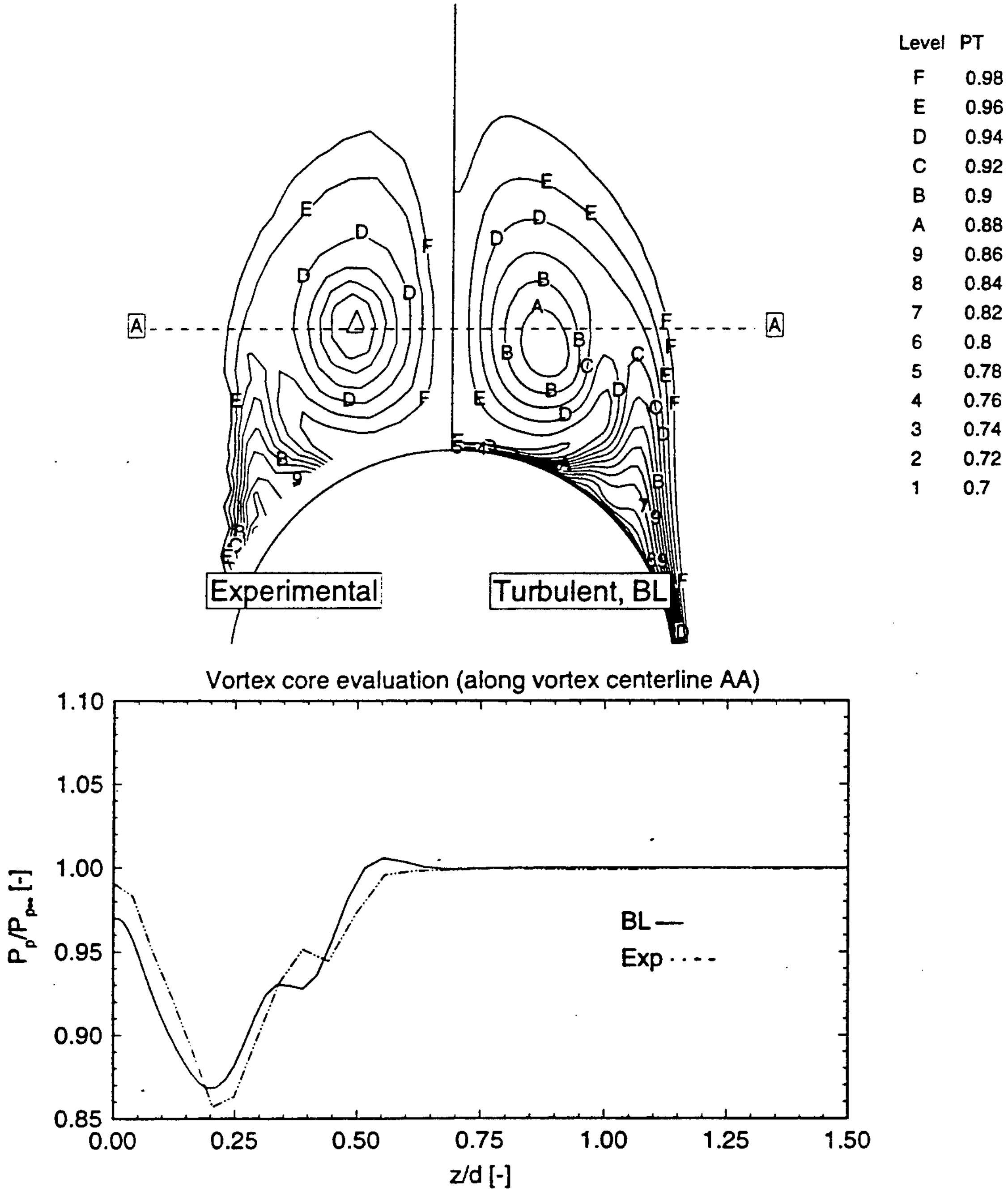

Level	PT
F	0.98
E	0.96
D	0.94
C	0.92
B	0.9
A	0.88
9	0.86
8	0.84
7	0.82
6	0.8
5	0.78
4	0.76
3	0.74
2	0.72
1	0.7

Figure 16. Pitot pressure contours for experiment compared to laminar and turbulent viscous computations. Vortex core pitot pressure along Z/D line to flow field centerline.
Case 6, M=0.7, α=14°, X/D =11.5.

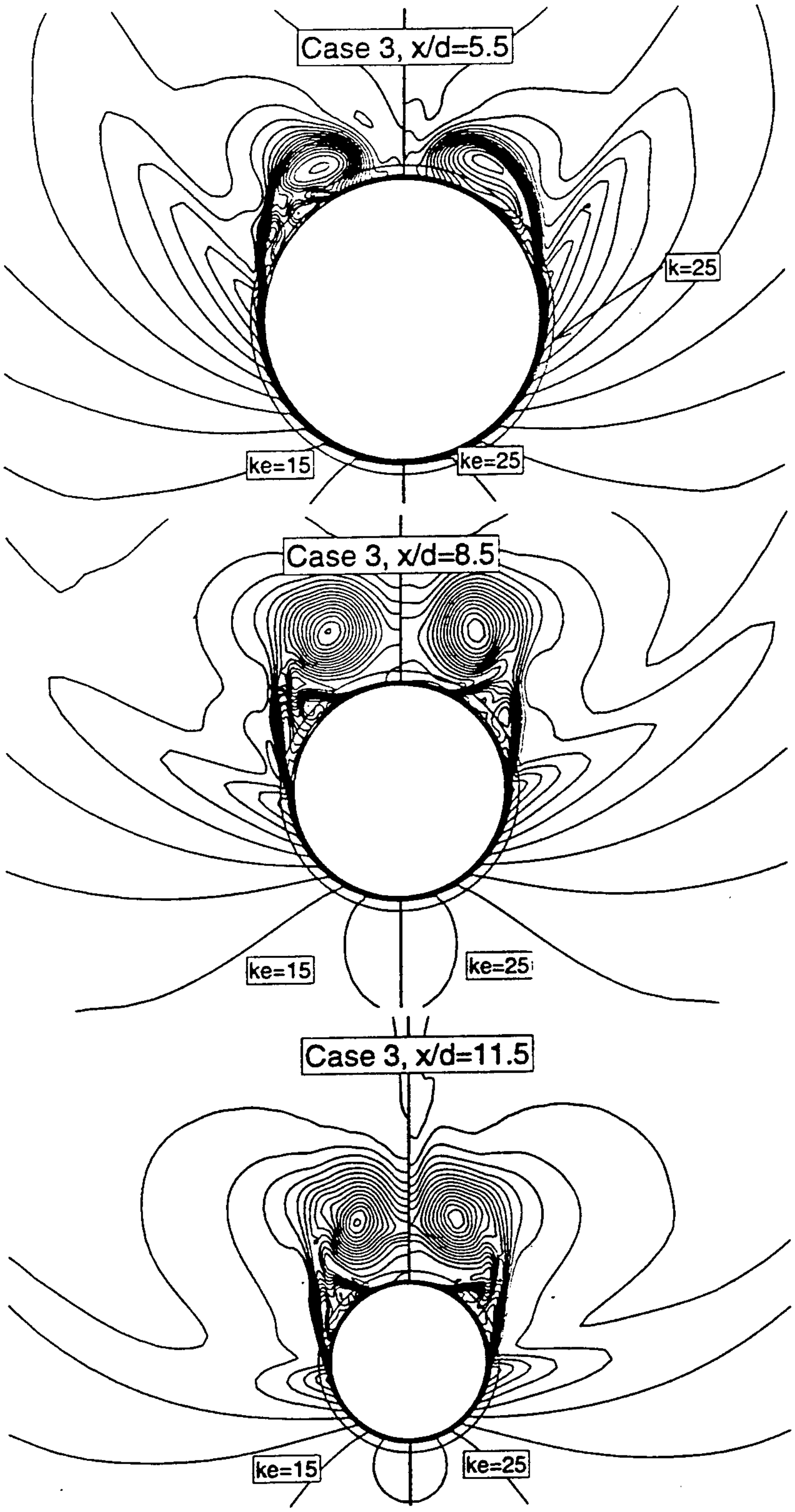

Figure 17. Pitot pressure contours comparing results for BL turbulence model using cutoff values of 15 and 25 for the extent of the length scale search, Case 3, M=2.5, α=14°, X/D =5.5, 8.5, 11.5.

APPENDIX A.2

Technical Paper, “Structured Grid Based Solution–Adaptive Technique for Complex Separated Flows”, to appear, *Journal of Applied Mathematics and Computation*

(T) 96 S A

A Structured Grid Based Solution–Adaptive Technique for Complex Separated Flows

by

Hugh Thornburg, Bharat K. Soni and Boyalakuntla Kishore
NSF Engineering Research Center for
Computational Field Simulation
Mississippi State University
Mississippi State, MS 39762

ABSTRACT

A structured grid based technique is presented to enhance the predictive capability of widely used CFD codes through the use of solution adaptive gridding. The procedure redistributes mesh points based upon an existing flowfield. A newly developed weight function employing Boolean sums is utilized to represent the local truncation error. This weight function is then used to construct forcing functions associated with an elliptic system. A NURBS representation is employed to define block surfaces for boundary point redistribution. The technique has been applied to a flowfield about a configuration of practical interest. This flowfield involves supersonic freestream conditions at angle of attack, and exhibits large scale separated vortical flow, vortex–vortex and vortex–surface interactions, separated shear layers and multiple shocks of different intensity. The results demonstrate the capability of the developed weight function to detect shocks of differing strengths, primary and secondary vortices, and shear layers adequately.

INTRODUCTION

Rapid access to highly accurate data about complex configurations is needed for multi–disciplinary optimization and design. In order to efficiently meet these requirements a closer coupling between the analysis algorithms and the discretization process is needed. In some cases, such as free surface, temporally varying geometries, and fluid structure interaction, the need is unavoidable. In other cases the need is to rapidly generate and modify high quality grids. Techniques such as unstructured and/or solution–adaptive methods can be used to speed the grid generation process and to automatically cluster mesh points in regions of interest. Global features of the flow can be significantly affected by isolated regions of inadequately resolved flow. These regions may not exhibit high gradients and can be difficult to detect. Thus excessive resolution in certain regions does not necessarily increase the accuracy of the overall solution.

Several approaches have been employed for both structured and unstructured grid adaption. The most widely used involve grid point redistribution, local grid point enrichment/derefinement or local modification of the actual flow solver. However, the success of any one of these methods ultimately depends on the feature detection algorithm used to determine solution domain regions which require a fine mesh for their accurate representation. Typically, weight functions are constructed to mimic the local truncation error and may require substantial user input. Most problems of engineering interest involve multi–block grids and widely disparate length scales. Hence, it is desirable that the adaptive grid feature detection algorithm be developed to recognize flow structures of different type as well as differing intensity, and adequately address scaling and normalization across blocks.

These weight functions can then be used to construct blending functions for algebraic redistribution, interpolation functions for unstructured grid generation, forcing functions to attract/repel points in an elliptic system, or to trigger local refinement, based upon application of an equidistribution principle. The popularity of solution–adaptive techniques is growing in tandem with unstructured methods. The difficultly of precisely controlling mesh densities and orientations with current unstructured grid generation systems has driven the use of solution–adaptive meshing Use of derivatives of density or pressure are widely used for construction of such weight functions, and have been proven very successful for inviscid flows with shocks[2,7,11]. However, less success has been realized for flowfields with viscous layers, vortices or shocks of disparate strength. It is difficult to maintain the appropriate mesh point spacing in the various regions which require a fine spacing for adequate resolution. Mesh points often migrate from important regions due to refinement of dominant features. An example of this is the well know tendency of adaptive methods to increase the resolution of shocks in the flowfield around airfoils, but in the incorrect location due to inadequate resolution of the stagnation region. This problem has been the motivation for this research.

The weight functions developed utilize scaled derivatives and normalizing procedures to minimize or eliminate the need for user input. The most attractive feature of this work is the ability to detect flow features of varying intensity and the lack of user defined inputs for the selection of the weight function.

In this research a NURBS representation is employed to define block surfaces for boundary point redistribution. The features described have been implemented into Adapt2D/3D. An adaptive grid system capable of automatically resolving complex flows with shock waves, expansion waves, shear layers and complex vortex–vortex and vortex–surface interactions. An adaptive grid approach seems well suited for such problems in which the spatial distribution of length scales is not known a priori.

APPROACH TO ADAPTION

The elliptic generation system:

$$\sum_{i=1}^{3}\sum_{j=1}^{3} g^{ij}\hat{r}_{\xi^i\xi^j} + \sum_{k=1}^{3} g^{kk}P_k\hat{r}_{\xi^k} = 0 \qquad (1)$$

where
r : Position vector,
g^{ij} : Contravariant metric tensor
ξ^i : Curvilinear coordinate, and
P_k : Control function.

is widely used for grid generation [1]. Control of the distribution and characteristics of a grid system can be achieved by varying the values of the control functions P_k in Equation 1 [1]. The application of the one dimensional form of Equation 1 combined with equidistribution of the weight function results in the definition of a set of control functions for three dimensions.

$$P_i = \frac{(W_i)_{\xi^i}}{W_i} \quad (i = 1,2,3) \qquad (2)$$

These control functions were generalized by Eiseman [2] as:

$$P_i = \sum_{j=1}^{3}\frac{g^{ij}}{g^{ii}}\frac{(W_i)_{\xi^i}}{W_i} \quad (i = 1,2,3) \qquad (3)$$

In order to conserve some of the geometrical characteristics of the original grid the definition of the control functions is extended as:

$$P_i = \left(P_{initialgeometry}\right) + c_i(P_{wt}) \quad (i = 1,2,3) \tag{4}$$

where $P_{\text{initial geometry}}$: Control function based on initial geometry
P_{wt} : Control function based on current solution
c_i : Constant weight factor.

These control functions are evaluated based on the current grid at the adaption step. This can be formulated as:

$$P_i^{(n)} = P_i^{(n-1)} + c_i(P_{wt})^{(n-1)} \quad (i = 1,2,3) \tag{5}$$

where

$$P_i^{(1)} = P_i^{(0)} + c_i(P_{wt})^{(0)} \quad (i = 1,2,3) \tag{6}$$

A flow solution is first obtained with an initial grid. Then the control functions P_i are evaluated in accordance with Equations 2 and 5, which is based on a combination of the geometry of the current grid and the weight functions associated with the current flow solution[11].

Evaluation of the forcing functions corresponding to the grid input into the adaptation program has proven to be troublesome. Direct solution of Equation 1 for the forcing functions using the input grid coordinates via Cramer's rule or IMSL libraries was not successful. For some grids with very high aspect ratio cells and/or very rapid changes in cell size, the forcing functions became very large. The use of any differencing scheme other than the one used to evaluate the metrics, such as the hybrid upwind scheme[8], would result in very large mesh point movements. An alternative technique for evaluating the forcing functions based on derivatives of the metrics was implemented[3].

$$P_i = \frac{1}{2}\frac{(g_{11})_{\xi^i\xi^i}}{g_{11}} + \frac{1}{2}\frac{(g_{22})_{\xi^i\xi^i}}{g_{22}} + \frac{1}{2}\frac{(g_{33})_{\xi^i\xi^i}}{g_{33}} \quad (i = 1,2,3) \tag{7}$$

This technique has proven to be somewhat more robust, but research efforts are continuing in this area.

SOLUTION PROCEDURE

The software developed inputs two PLOT3D format files [4], one for the grid and one for the flow solution. These files contain the number of blocks, the grid size, the grid coordinates and the solution vector. Output consists of an NPARC[5] restart file, as well as two PLOT3D files of the adapted grid and the flow solution interpolated onto the new grid. A multi–block treatment capability is included. The adaptive grid is constructed in three steps. The first step is to generate the weight functions, which due to their critical importance will be discussed in detail in a separate section. The second step is to generate the actual adapted grid by equidistribution of the aforementioned weight function. In the current work this is accomplished by the numerical solution of Equation 1. A coupled three–dimensional strongly implicit procedure (CSIP) as described by Ghia et al. [6] has been implemented for the solution of the discretized equations. Upwind differencing, with biasing based on the sign of the forcing functions, as well as central differencing has been implemented and studied for the first derivative terms. The first order upwind differencing increases the stability of the procedure, but at the expense of smearing the grid clustering. Hence, a hybrid upwind/central differencing scheme has been implemented to lessen this smearing while maintaining the smoothness and stability of the upwind procedure. Central differencing has been employed for all second and mixed derivative terms. All non-linear terms were treated by quasi-linearization. Since Equation 1 is solved iteratively, the forcing functions must be evaluated for each new successive grid point location. The forcing functions are obtained by interpolation from the original grid. The interpolation procedure employed was that used for the non-matching block to block interface capability of the NAPRC [5] code. This scheme is based on trilinear interpolation. Upon convergence of this process the flow solution is interpolated onto the adapted grid using the same interpolation subroutine. Calculations can then be continued from the new restart file. This procedure can then be repeated until an acceptable solution is obtained. Experience indicates that coupling this procedure with a code capable of treating time accurate grid movement would ease this process and lessen the CPU requirements.

Currently, grid adaptation is performed in an uncoupled manner. For simple problems this is adequate as only marginal changes are observed after two to three cycles of adaptation. However, for complex flow fields it appears necessary to closely couple the flow solver and the adaptation technique as significant changes in both grid and flow solution are visible after even six cycles of uncoupled adaption. Also, the more complex flows require the use of a hybrid differencing scheme for the solution of the grid equations. For flows containing strong shocks and shear layers along with weaker structures, central differencing was unstable and first order upwind differencing of the grid equations smeared the weaker structures. Therefore to obtain full benefit of the adaptive grid blended central/upwind has been implemented for the grid equations.

WEIGHT FUNCTIONS

Application of the equidistribution law results in grid spacing inversely proportional to the weight function, and hence, the weight function determines the grid point distribution. Ideally, the weight would be the local truncation error ensuring a uniform distribution of error. However, evaluation of the higher-order derivatives contained in the truncation error from the available discrete data is progressively less accurate as the order increases and is subject to noise. Determination of this function is one of the most challenging areas of adaptive grid generation. Lower-order derivatives must be non-zero in regions of wide variation of higher-order derivatives, and are proportional to the rate of variation. Therefore, lower-order derivatives are often used to construct a weight function as a proxy for the truncation error. Construction of these weight functions often requires the user to specify which derivatives and in what proportion they are to be used. This can be a time consuming process. Also, due to the disparate strength of flow features, important features can be lost in the noise of dominant features. The weight functions developed by Soni and Yang [7] and Thornburg and Soni [8] are examples of such efforts. The weight function of Thornburg and Soni [8] has the attractive feature of requiring no user specified inputs. Relative derivatives are used to detect features of varying intensity, so that weaker, but important structures such as vortices are accurately reflected in the weight function. In addition, each conservative flow variable is scaled independently. One-sided differences are used at boundaries, and no-slip boundaries require special treatment since the velocity is zero. This case is handled in the same manner as zero velocity regions in the field. A small value, epsilon in equation 8, is added to all normalizing quantities. In the present work this weight function has been modified using the Boolean sum construction method of Soni [7]. Also, several enhancements of an implementation nature have been employed. For example epsilon has been placed outside the absolute value operator. This eliminated the possibility of spurious gradients in the weight function in regions where epsilon was nearly equal and opposite in sign to the local normalizing flow variable. Also, the normalizing derivatives have been set to an initial or minimum value of ten percent of the freestream quantities. This alleviates problems encountered in flows without significant features to trigger adaption in one or more coordinate directions. Otherwise a few percent variation would be normalized to the same level as a shock or other strong feature. The current weight function is as follows:

$$W = \frac{W^1}{max(W^1, W^2, W^3)} \oplus \frac{W^2}{max(W^1, W^2, W^3)} \oplus \frac{W^3}{max(W^1, W^2, W^3)}$$

Where, $k=1,2,3,$ and

$$W^k = 1 + \frac{\dfrac{|\varrho_{\xi^k}|}{|\varrho|+\varepsilon}}{\left(\dfrac{|\varrho_{\xi^k}|}{|\varrho|+\varepsilon}\right)_{\max}} \oplus \frac{\dfrac{|(\varrho u)_{\xi^k}|}{|(\varrho u)|+\varepsilon}}{\left(\dfrac{|(\varrho u)_{\xi^k}|}{|(\varrho u)|+\varepsilon}\right)_{\max}} \oplus \frac{\dfrac{|(\varrho v)_{\xi^k}|}{|(\varrho v)|+\varepsilon}}{\left(\dfrac{|(\varrho v)_{\xi^k}|}{|(\varrho v)|+\varepsilon}\right)_{\max}} \oplus \frac{\dfrac{|(\varrho w)_{\xi^k}|}{|(\varrho w)|+\varepsilon}}{\left(\dfrac{|(\varrho w)_{\xi^k}|}{|(\varrho w)|+\varepsilon}\right)_{\max}}$$

$$\oplus \frac{\dfrac{|\varrho_{\xi^k\xi^k}|}{|\varrho|+\varepsilon}}{\left(\dfrac{|\varrho_{\xi^k\xi^k}|}{|\varrho|+\varepsilon}\right)_{\max}} \oplus \frac{\dfrac{|(\varrho u)_{\xi^k\xi^k}|}{|(\varrho u)|+\varepsilon}}{\left(\dfrac{|(\varrho u)_{\xi^k\xi^k}|}{|(\varrho u)|+\varepsilon}\right)_{\max}} \oplus \frac{\dfrac{|(\varrho v)_{\xi^k\xi^k}|}{|(\varrho v)|+\varepsilon}}{\left(\dfrac{|(\varrho v)_{\xi^k\xi^k}|}{|(\varrho v)|+\varepsilon}\right)_{\max}} \oplus \frac{\dfrac{|(\varrho w)_{\xi^k\xi^k}|}{|(\varrho w)|+\varepsilon}}{\left(\dfrac{|(\varrho w)_{\xi^k\xi^k}|}{|(\varrho w)|+\varepsilon}\right)_{\max}} \qquad (8)$$

The symbol ⊕ represents the Boolean sum. Note that the directional weight functions are scaled using a common maximum in order to maintain the relative strength. For the results shown, the weight function used is the sum of the weight function defined by Eq. 8 and the one defined in [8]. The weight function defined in [8] is Eq. 8 evaluated without using the Boolean sum.

Flow past a wedge at Mach = 2.0 is used to illustrate the enhanced detection capabilities of this newly developed weight function. Figure 1 presents weight functions evaluated using the previous procedure, lower half plane, as well as the current procedure, upper half plane.

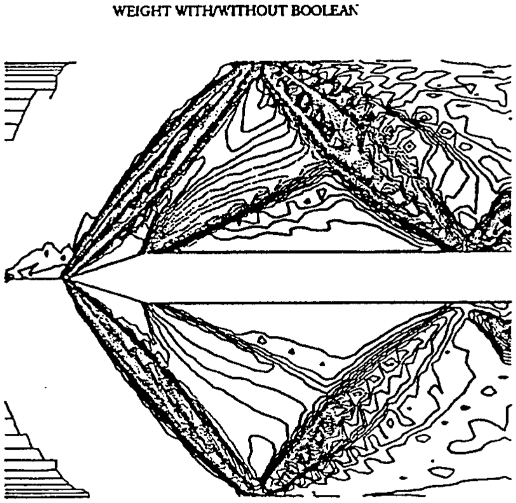

Figure 1. Comparison of Weight Functions.

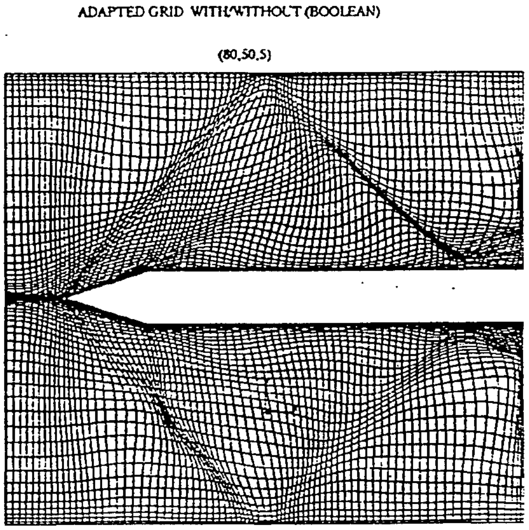

Figure 2. Comparison of Adapted Grids.

It can be observed that both weight functions clearly detected the primary shock. It can also be seen that the expansion fan, boundary layer, and the reflected shocks are much more clearly represented in the current weight function. Adapted grids using both weight function formulations are presented in Fig. 2. The high gradient regions of the expansion region are only reflected in the adapted grid using the new weight function. The reflected shock is also much sharper. Figure 3 compares the solution obtained using the current adaption procedure with that obtained using the original grid. The enhanced resolution is clearly evident.

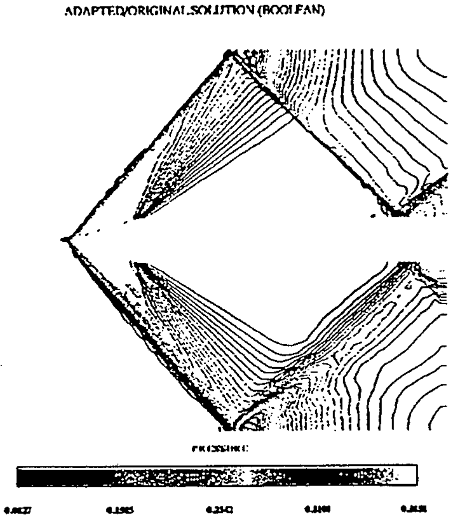

Figure 3. Comparison of Solutions Using Adapted Grid.

BOUNDARY POINT REDISTRIBUTION

Accurate representation of the flowfield in the vicinity of boundaries is critical for an acceptable overall solution. Physics occurring near boundaries often drive the flow physics occurring in other regions of the flowfield. This is especially true for noslip surfaces. Hence, the quality and distribution of the grid in this region is of critical importance. For the implementation of many turbulence models orthogonality is also required. When using an adaptive procedure based on a redistribution of mesh points, such as in this work, the interior points move as the grid is adapted. This leads to distorted cells if the boundary points are not redistributed as the grid is adapted. Both grid quality and geometric fidelity must be maintained during redistribution. In the current work all surfaces of individual blocks are treated in the same manner, whether block interfaces or flow boundary conditions. Two steps must be performed. First the geometry is defined, and secondly the surface mesh is regenerated using a given distribution mesh. The geometry is defined as a NURB surface from the current surface mesh to be redistributed. This procedure is based on the algorithms developed by Yu and Soni for Genie++[9]. This definition is then used to generate the surface using a user specified distribution mesh. The entire surface or a subregion can be redistributed. Subregions can be used to fix points, such as sharp corners or a transition point between boundary condition type. For example block boundary to noslip surface. The distribution mesh is a [0,1] square evaluated from a specified surface based upon arc length. For solid surfaces the distribution mesh is based on the nearest interior coordinate surfaces. The spacing between surfaces is small and the surfaces are of a similar geometric shape. Therefore the normal coordinate is nearly orthogonal to the surface. Block interfaces are treated by redistributing the current block surface based on its corresponding surface in the neighboring block.

FLOW AROUND GENERIC MISSILE CONFIGURATION

Supersonic flow at Mach=1.45 and 14 degree angle of attack has been simulated around a tangent-ogive cylinder. The grid constructed after two adaption cycles using hybrid differencing of the grid equations and the current weight functions is presented is presented in Figure 4.

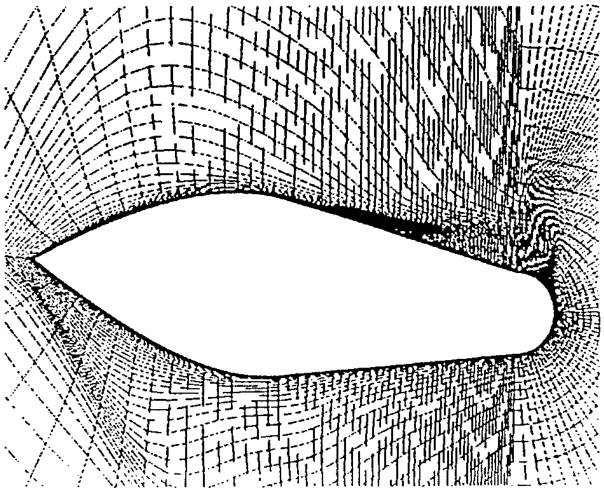

Figure 4. Adapted grid after two cycles.

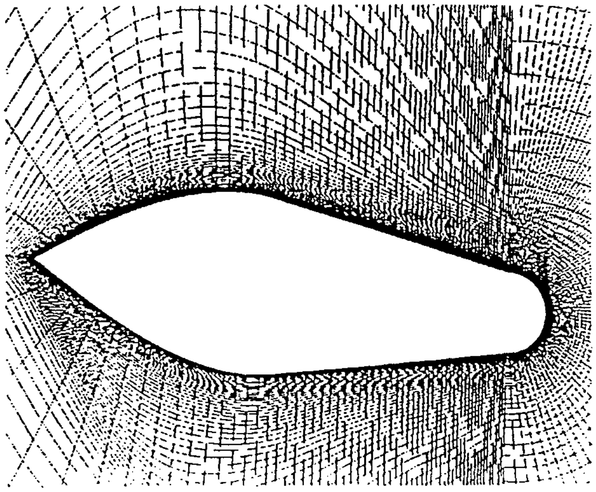

Figure 5. Adapted grid after two cycles.

Figure 5 presents the grid constructed using the previous weight function and the same flow conditions and number of adaptation cycles. Figures 5 and 6 present streamwise cuts of the two grids shown in Figs 4 and 5 at X/D = 5.5 and 7.5 respectively. The left had side of Figures 6 and 7 correspond to Figure 5 and the right hand side corresponds to Figure 5.

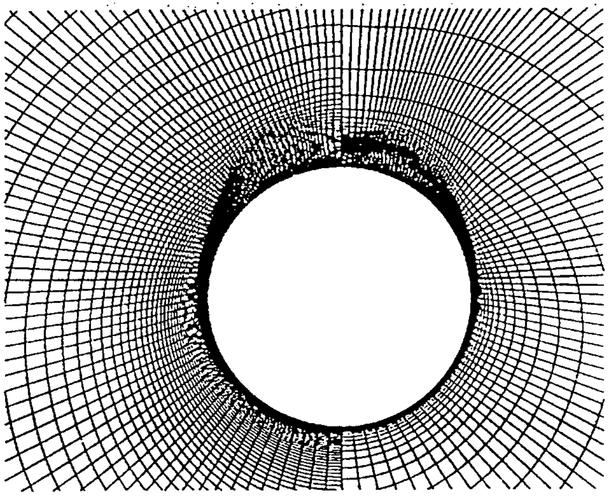

Figure 6. X/D = 5.5

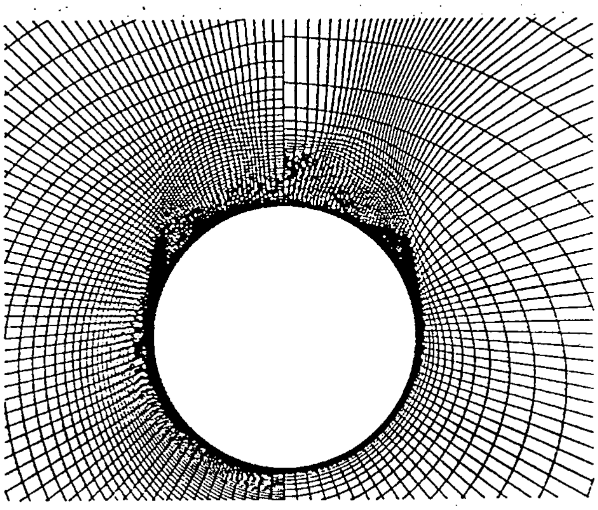

Figure 7. X/D = 8.5.

As can be seen from Figures 4–7 the feeding sheet, and both primary and secondary vortices, as well as the strong shock at the nose are clearly visible. Comparison of Figures 4 and 5 show the sharper resolution provided by the new formulation of the weight function. The shock itself is more sharply represented, but the greatest improvement is in representing the vortex and the shear layer. The previous formulation simply clustered mesh points in the vicinity of the vortex. This does improve resolution. However, the new formulation clearly shows the circular shape of the vortex, as well as the high gradient regions on the edges of the structure. Hence, the new method of grid adaptation more closely reproduces the flow physics. Also, stronger and sharper concentration of mesh points is observed with the new formulation. This is most apparent in the far field region and the greater detail of the flowfield visible in the grid. Both the primary and secondary separation points are well represented. On the windward side of the missile it can be seen that the boundary layer clustering is greatly increased by the adaptation procedure. This is desirable in this area as the boundary layer is the only feature of interest. Examination of Fig 4 reveals that toward the aft end of the missile, the off surface structure is not well defined. This is because after two cycles of adaptation the structure is not well enough defined by the flow solver and associated grid for the adaptation procedure to sharply define the structure. Only structures that have been at least partially resolved by the flow solver can be detected by the weight function. Hence the quality of the weight function is dependent upon the quality of the solution. It should be noted that resolution of the flowfield improves with each cycle of adaptation. The adaption procedure and the flow solver should be coupled so that the adapted grid can reflect all the features that are detected as the solution progresses and improves due to adaption.

Figure 8 presents the flow solution obtained using the NPARC [5] flow solver, and the KE turbulence model option. Figure 9 presents the associated weight function.

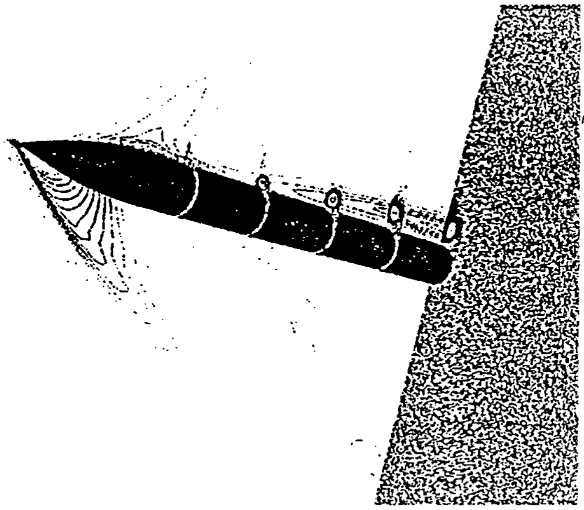

Figure 8. Normalized Stagnation Pressure.

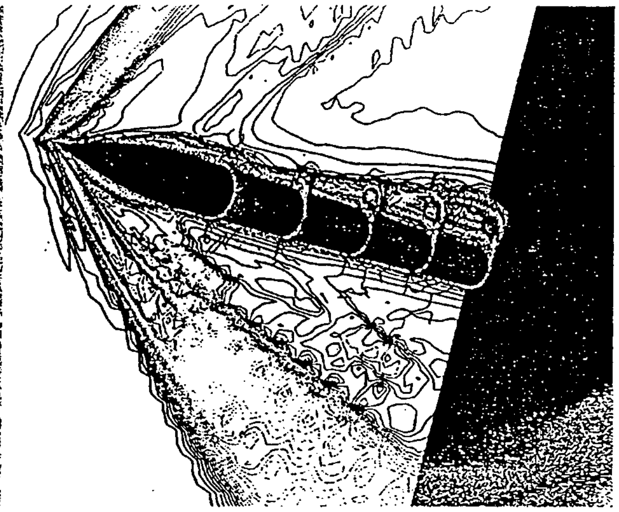

Figure 9. Weight Function.

CONCLUSIONS

The results shown demonstrate the capability of the developed weight function to detect shocks of differing strengths, primary and secondary vortices, and shear layers adequately. For the test case presented the increased resolution of the shock and the expansion region resulted in the structure increasing in size so that interaction with the farfield occurred. Thus, the farfield boundaries should be placed at a larger distance from the body. No user input is required. It is imperative that the adaptation process be coupled with the flow solver as experience indicates that the complex flowfields may require many adaptive cycles. This is particularly critical for flow fields that are not well represented by the initial solution. The adapted grids allow the use of larger time steps to increase the convergence rate. However, the single greatest benefit resulting from the adapted grid is the lowering of the artificial viscosity required for stability. The adapted grid aligns and clusters near shocks and shear layers. For the test problem a dramatic decrease in the artificial viscosity coefficients is possible when running on the adapted grid. This results in off surface structures which are much sharper and more closely resemble the flow visualization. The boundary layer on the windward side also became thinner and the normal grid spacing was decreased by the adaptive procedure.

Currently multi–block problems are being simulated to evaluate this capability. Attention is being placed upon across block scaling for the weight functions. A global maximum across all blocks seems to work well for the normalization of weight function components. However, this issue is being monitored as more complex problems are attempted. A further problem arises due to equidistribution via forcing functions. This does not appear to be a problem where a block face is connected to one and only one face of another block. Problems have been encountered for a multi–block launch vehicle computation where a block face consisted of a block to block connection and a solid surface for the base region. A smooth, continuous set of forcing functions across this block boundary does not yield a smooth grid. It is believed that this is due to the elliptic character of the grid equations. The simple fix is to introduce artificial block boundaries to force one to one correspondence. Work is continuing on these issues as well as coupling with a flow solver, unsteady flows, and more complex multi–block problems. These results will be published at a later date.

References

1. Thompson, J.F., Warsi, Z.U.A. and Mastin, C.W., Numerical Grid Generation: Foundations and Applications, North–Holland, Amsterdam. 1985.
2. Eiseman, P.R., "Alternating Direction Adaptive Grid Generation," AIAA Paper 83–1937, 1983.
3. Soni, B.K., "Structured Grid Generation in Computational Fluid Dynamics," Vichnevetsky, R., Knight, D., and Richter, G. (eds.), Advances in Computer Methods for Partial Differential Equations VII, Rutgers University, pp 689–695, June 1992.
4. Buning, P.G. and Steger, J.L., "Graphics and Flow Visualization in Computational Fluid Dynamics," AIAA Paper 85–1507–CP, Proceedings of the AIAA 7th Computational Fluid Dynamics Conference, 1985.
5. NASA LeRC and USAF AEDC, "NPARC 1.0 User Notes," June 1993.
6. Ghia, K.N., Ghia, U., Shin, C.T. and Reddy, D.R., "Multigrid Simulation of Asymptotic Curved–Duct Flows Using a Semi–Implicit Numerical Technique," Computers in Flow Prediction and Fluid Dynamics Experiments, ASME Publication, New York 1981.
7. Soni, B.K. and Yang, J.C., "General Purpose Adaptive Grid Generation System," AIAA–92–0664, 30th Aerospace Sciences Meeting, Reno, NV, Jan. 6–9, 1992.
8. Thornburg, H.J. and Soni, B.K., "Weight Functions inGrid Adaption," Proceedings of the 4th International Conference in Numerical Grid Generation in Computational Fluid Dynamics and Related Fields held at Swansea, Wales 6–8th April 1994.
9. Soni, B.K., Thompson, J.F., Stokes, M.L. and Shih, M.H., "GENIE++, EAGLEView and TIGER: General and Special Purpose Interactive Grid Systems," AIAA–92–0071, 30th Aerospace Sciences Meeting, Reno, NV, Jan. 6–9, 1992.
10. NASA LaRC, "User Document for CFL3D/CFL3DE (Version 1.0)", 1993.
11. Thompson, J.F., "A Survey of Dynamically–Adaptive Grids in Numerical Solution of Partial Differential Equations," Applied Numerical Mathematics, vol. 1, pp 3–27, 1985.